
Unterschrift (Betreuer)



DIPLOMARBEIT

Depth-Resolved Measurement of Ocular Fundus Pulsations in Rats using Low-Coherence Tissue Interferometry

Ausgeführt am

Institut für Angewandte Physik
der Technischen Universität Wien

unter der Anleitung von

Ao.Univ.-Prof. DI Dr. Martin Gröschl

Institut für Angewandte Physik
Technische Universität Wien

in Zusammenarbeit mit

Ass.-Prof. DI(FH) René Werkmeister, PhD

Ao.Univ.-Prof. DI Dr. Leopold Schmetterer

Zentrum für med. Physik und biomed. Technik
Medizinische Universität Wien

durch

József Teodor Klaizer

Matr. Nr.: e1129879

Udvarnoki utca 8
H-9400 Sopron

Wien, 18. Februar 2017

Unterschrift (Student)

Szüleimnek.

This document was set with the help of $\text{\LaTeX} 2_{\epsilon}$, KOMA-Script and \BibLaTeX . Diagrams and graphs were created with the \LaTeX packages TikZ and pgfplots as well as with the Python library Matplotlib. Mathematical calculations were performed with Sagemath. Git was used for version controlling.

Abstract

Low-coherence tissue interferometry (LCTI) is an optical technique that uses light of low temporal coherence for the observation of the pulsatile, heart rate related movement of various structures of the eye at pre-selected axial positions (i.e., in various depths, corresponding to different reflective structures in the eye). By means of LCTI, Dragostinoff et al. [1] were able to measure relative changes in the positions of various layers of the human eye (e.g., inner limiting membrane, retinal pigment epithelium) with to the cornea serves as reference.

However, pulsation measurements of the outer most layer of the human eye ball, i.e. the sclera are currently not possible, which is due to the large blood volume within the choroid and the associated scattering and absorption of the probing beam.

In this master thesis, an LCTI system for pulsation measurements in humans was adapted to allow for observation of ocular pulsations in all layers (including sclera) of the rat's eye. Due to the smaller thickness of retinal and choroidal structures and the related lower absorption, these measurements seem feasible.

Within this master thesis following work packages were performed: (1) re-design and adaptation of the optical system; (2) in vitro measurements using phantom structures; (3) in vivo measurements on rats involving the determination of the absolute position of the ocular layers with respect to the cornea front surface and measurement of heart beat related changes in the position of these layers.

This master thesis is the first step for establishment of an LCTI system for studying both dynamic and long-term variations in axial position of ocular structures in rodent's eyes. The system allows for both estimation of pulsatile ocular blood flow and measurement of real-time growth of axial eye length in myopia models.

The work was performed in a large interdisciplinary group of scientists from different sub-specialities, including physics, electrical engineering and medicine, under the guidance of Prof. Dr. Martin Gröschl, TU Wien and Prof. René Werkmeister, PhD, as well as Prof. Dr. Leopold Schmetterer, Medical University of Vienna.

Kurzfassung

Niederkohärenz-Gewebeinterferometrie (Low-Coherence Tissue Interferometry, LCTI) ist eine optische Technik, die Licht niedriger zeitlicher Kohärenz verwendet, um die pulsatilen, Herzfrequenz-bezogenen Bewegungen verschiedener Augenstrukturen an vorbestimmten axialen Positionen (d.h. in unterschiedlichen Tiefen, entsprechend den verschiedenen reflektierenden Strukturen im Auge) zu untersuchen. Mit Hilfe von LCTI konnten Dragostinoff et al. [1] relative Veränderungen in den Positionen verschiedener Schichten des menschlichen Auges (z. B. innere Grenzmembran, retinales Pigmentepithel) in Bezug zur Hornhaut als Referenz messen.

Jedoch sind Pulsationsmessungen der äußersten Schicht des menschlichen Auges, d.h. der Sclera, derzeit nicht möglich, was auf das große Blutvolumen innerhalb der Aderhaut und die damit verbundene Streuung und Absorption des Probenstrahls zurückzuführen ist.

In dieser Masterarbeit wurde ein für menschliche Pulsationsmessungen benutztes LCTI-System adaptiert, um die Beobachtung von Augenpulsationen in allen Schichten (einschließlich Sclera) von Rattenaugen zu ermöglichen. Wegen der geringeren Dicke der Netzhaut- und Aderhautstrukturen und der damit verbundenen geringeren Absorption erscheinen derartige Messungen durchführbar.

Im Rahmen dieser Masterarbeit wurden folgende Arbeiten durchgeführt: (1) Neukonstruktion und Anpassung des optischen Systems; (2) *in vitro* Messungen an Phantomstrukturen; (3) *in vivo* Messungen an Ratten, die die Bestimmung der absoluten Position der Augenschichten in Bezug auf die Hornhautvorderfläche bzw. die Messung von Herzschlag-bezogenen Veränderungen in der Position dieser Schichten einschließen.

Diese Masterarbeit ist der erste Schritt zur Etablierung eines Systems zur Untersuchung sowohl der dynamischen als auch der langfristigen Variationen der axialen Lage der Schichtstrukturen in den Augen von Nagetieren. Das System ermöglicht sowohl eine Abschätzung des pulsierenden, okulären Blutflusses als auch die Messung des Echtzeitwachstums der axialen Augenlänge bei Myopiemodellen.

Die Arbeit wurde in einer großen interdisziplinären Gruppe von Wissenschaftlern aus verschiedenen Disziplinen durchgeführt, im Speziellen Physik, Elektrotechnik und Medizin, unter der Leitung von Prof. Martin Gröschl, TU Wien, sowie Prof. René Werkmeister und Prof. Leopold Schmetterer, Medizinische Universität Wien.

Acknowledgements

First and foremost I would like to express my sincere gratitude to my supervisor Martin Gröschl of the Institute of Applied Physics at the Vienna University of Technology for his continuous support and advices.

My honest thanks also goes to Leopold Schmetterer of the Center of Medical Physics and Biomedical Engineering at the Medical University of Vienna for introducing me to the topic. He provided me an opportunity to join his research team and gave access to the research facility.

I owe my deepest gratitude to René Werkmeister, who was a constant source of expert knowledge; I could always count on him. Furthermore, I am very grateful to him for proofreading my whole master thesis.

I would like to offer my special thanks to Corinna Knopf for helping me conducting all my experiments and her contribution in the animal testing.

At the Center of Medical Physics and Biomedical Engineering I had the honor of working together with many great people and I want to thank them all; especially Iris Schmidt, Thomas Blaschke, Martin Pfister, Valentin Aranha dos Santos, Gerold Aschinger, Alina Messner, Martin Vietauer, Nikolaus Dragostinoff and Andreas Hodul.

Furthermore, I am grateful to Lilly Merz Raff and Diethelm Raff for their selfless and generous support and for helping me get through the difficult times.

This master thesis would not have been possible without the support of my family. I would like to thank especially to my parents Erika and József Klaizer, as well as to my wife Fanni, my sister Kriszti and my cousin Barbi. They have been encouraging, supportive and shown belife in me and my work. Thank you!

Contents

Abstract	iii
Kurzfassung	iv
Acknowledgements	v
Contents	viii
1 Introduction	1
1.1 Motivation	1
2 Medical Aspects	4
2.1 Human Eye	4
2.1.1 Fibrous Tunic (<i>tunica fibrosa bulbi</i>)	4
2.1.2 Vascular Tunic (<i>tunica vasculosa bulbi</i>)	7
2.1.3 Retina	9
2.1.4 The Interior of the Eye, the Ocular Media	12
2.2 Eye Diseases	13
2.2.1 Glaucoma	13
2.2.2 Age-related Macular Degeneration	15
2.2.3 Diabetic Retinopathy (Diabetic Eye Disease)	16
2.3 The Rat Eye (Differences to the Human Eye)	16
2.3.1 Pigmented Rats	19
2.3.2 Albino Rats	19
3 Theory and Principles of LCTI	20
3.1 The Wave Equation	20
3.1.1 Intensity	21
3.1.2 Power	21
3.1.3 Energy	21
3.2 Monochromatic Waves	21
3.2.1 Complex Amplitude	21
3.2.2 Optical Intensity	22
3.2.3 Interference	22
3.3 Non-monochromatic Light	23
3.3.1 Optical Intensity	24
3.3.2 Interference	25

Contents

3.3.3	Visibility	25
3.4	Coherence	26
3.4.1	Temporal Coherence	26
3.4.2	Coherence Time and Coherence Length	26
3.5	Optical Path Difference and Optical Path Length	27
3.6	Dynamic Interferometric Length Measurement Technique	28
3.7	Partial Coherence Interferometry	28
3.8	Dual Beam PCI	29
3.9	Spectral Interferometry	30
3.10	Optical Coherence Tomography (OCT)	30
3.10.1	Low-coherence Interferometry	30
3.10.2	OCT	31
3.11	Measurement of OBF and OFP	32
3.11.1	Laser Doppler Velocimetry (LDV)	32
3.11.2	Pulsatile Ocular Blood Flow by Laser Interferometry	32
3.12	Low-Coherence Tissue Interferometry (LCTI)	33
3.12.1	Description of the System	34
3.12.2	Measurement Process	44
4	Optical Setup	46
4.1	Optical Setup of the Old System	46
4.2	Adaptations to the Rat Eye	48
4.2.1	Equation System	48
4.2.2	Fringe Contrast	48
4.2.3	Solutions of the Equation System 4.1	52
4.3	Optical Setup of the New System	54
5	Hardware and Software	57
5.1	Incompatibility Issues	57
5.2	Hardware	58
5.2.1	PC	58
5.2.2	Data Acquisition and Stepping Motor Controller	59
5.3	Software	60
5.3.1	Operating System and Development Environment	60
5.3.2	NI-DAQ Driver	60
5.3.3	Strasing PCI Driver	62
5.4	Data Aquisition and Signal Processing	62
5.4.1	Filtering and Image Enhancement	62
5.4.2	Data Acquisition Software Developed in LabVIEW Environment	62
5.4.3	Changes in the LabVIEW Code	63
6	Measurements and Results	65
6.1	In Vitro Measurements	65
6.1.1	Results	65

Contents

6.2	In Vivo Measurements	70
6.2.1	Laboratory Rats Used in the Study	70
6.2.2	Remarks	71
6.2.3	Representative Results	73
7	Conclusion and Future Work	85
	References	87
	List of Figures	93
	List of Tables	94
	Acronyms and Abbreviations	97
	Appendices	98
A	Technical Specifications	99
A.1	Datasheet NI-DAQ	100
A.2	Manual for Stresing LCCD Camera System	101
A.3	Fiber Collimator: HPUCO-23-850-S-6.2AS, OZ Optics	102
A.4	Optical Fiber: SM800-5.6-125, Thorlabs	103
A.5	Optical Isolator: IO-F-850-APC, Thorlabs	104
A.6	Polarisation Controller: FPC030, Thorlabs	105
A.7	Beam Splitter Cube: , Thorlabs	106
B	LabVIEW	107
B.1	Axial Eye Length Measurement	111
B.2	Ocular Fundus Pulsation Measurement	114
B.3	Data Evaluation	118
C	Curriculum Vitæ	119

Chapter 1

Introduction

LCTI is an optical technique that uses light of low temporal coherence for the observation of the pulsatile, heart rate related movement of various structures of the eye at pre-selected axial positions (i.e., in various depths, corresponding to different reflective structures in the eye). By means of LCTI, Dragostinoff et al. [1] were able to measure relative changes in the position of various layers of the human eye (e.g. inner limiting membrane (ILM), retinal pigment epithelium (RPE)) with respect to the cornea that serves as reference. However, pulsation measurements of the outer most layer of the eye ball, i.e. the sclera, using this technique in humans is currently not possible, which is due to the large blood volume within the choroid and the associated scattering and absorption of the probing beam.

The aim of this master thesis is the adaptation of an LCTI system to allow for observation of ocular fundus pulsations (OFPs) in all layers (including sclera) of the rat's eyeball. Due to the smaller thickness of retinal and choroidal structures and the related lower absorption, these measurements seem feasible.

First, the system was re-designed and the optical system has been adapted to the characteristics of the rat's eyeball. Secondly, in vitro measurements were performed using phantom structures. This was followed by in vivo rat measurements, in which (1) the absolute position of the ocular layers with respect to the cornea front surface was determined, (2) heart beat related changes in the position of these layers were measured.

1.1 Motivation

285 million people are estimated to be visually impaired worldwide: 39 million are blind and 246 have low vision (see Figure 1.1). 80.00 % of all visual impairment (VI) can be prevented or cured [2].

If one look at the global causes of VI, one can see, that cataract and uncorrected refracted errors are the leading causes.

Visual impairments and blindness in the world

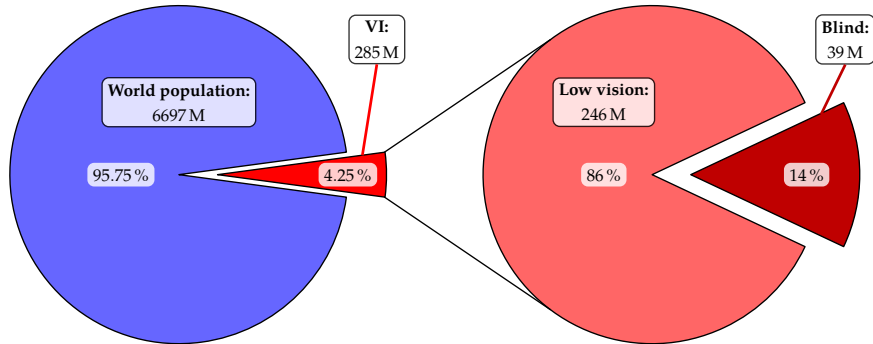


Figure 1.1: The ratio of VI and blindness to the world population. Figure is based on data from [3].

According to WHO, other main causes of VI in 2002 are glaucoma (12.30%), age-related macular degeneration (AMD) (8.70%), corneal opacities (5.10%), diabetic retinopathy (DR) (4.80%), childhood blindness (3.90%), trachoma (3.60%), and onchocerciasis (0.80%). All of the above causes, except AMD, belong to the avoidable VI [4] (see Figure 1.2 and Figure 1.3).

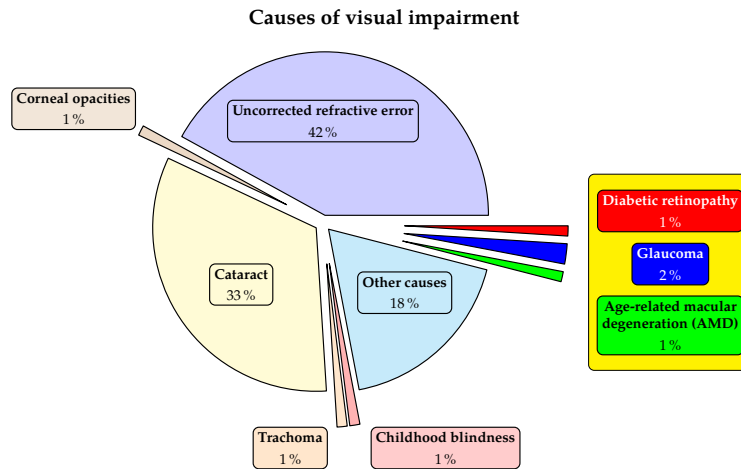


Figure 1.2: The most common global causes of VI. Three of these “main causes”, namely glaucoma, AMD and DR, can be associated with an altered ocular blood flow. Figure is based on data from [3].

Three of these “main causes”, namely glaucoma, AMD and DR, can be associated with an altered ocular blood flow [5–7].

Completion of this master thesis is the first step for establishment of an LCTI system

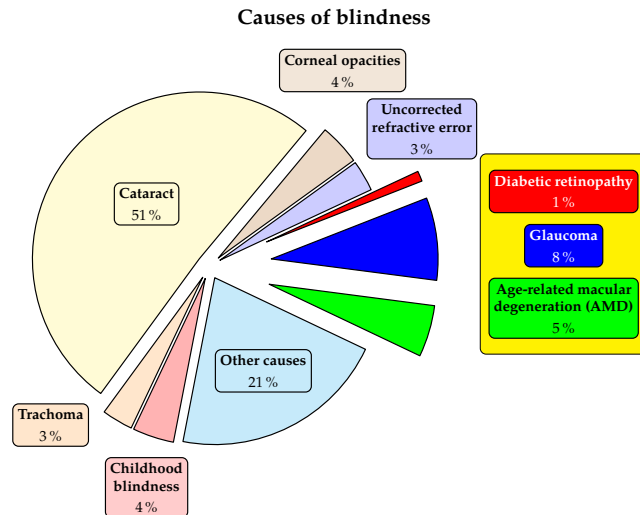


Figure 1.3: The most common global causes of blindness. Three of these “main causes”, namely glaucoma, AMD and DR, can be associated with an altered ocular blood flow. Figure is based on data from [3].

for studying both dynamic and long-term variations in axial position of ocular structures in rodent’s eyes. Such a system would allow for both estimation of pulsatile ocular blood flow (POBF) and measurement of real-time growth of axial eye length (AEL) in myopia models.

Chapter 2

Medical Aspects

In this chapter, the anatomy of the human eye is described followed by the most important eye diseases caused by deficiencies in the ocular blood flow (OBF). The main differences between the human and rat eye are discussed at the end of the chapter.

2.1 Human Eye

Figure 2.1 on page 5 shows the superior view of transverse section of right eyeball.

The bulb of the eye (*bulbus oculi*) is nearly a spheroid that is situated in a skeletal cavity, the orbit. The sagittal diameter of the eyeball amounts to about 24 mm and its vertical diameter to about 23.5 mm [10].

Anatomically, the wall of the eyeball consists of three layers: (1) fibrous tunic, (2) vascular tunic and (3) retina [8].

The outermost layer is the fibrous tunic (*tunica fibrosa bulbi*) consisting of the *sclera* behind and the *cornea* in front; the middle layer is a vascular pigmented tunic (*tunica vasculosa bulbi*) comprising, from behind forward, the *choroid*, ciliary body (*corpus ciliare*), and *iris*; the innermost is a nervous tunic, the *retina*. Within these coats are the chambers (*camerae bulbi*) containing the aqueous humor (*humor aquosus*), the vitreous body (*corpus vitreum*) and the flexible lens.

2.1.1 Fibrous Tunic (*tunica fibrosa bulbi*)

Parts of two spheres with different radii build up the outer surface of the eye: the *cornea* anteriorly (accounts for $\approx 7\%$ of the ocular surface) and the *sclera* posteriorly (accounts for $\approx 93\%$). They form the semi-elastic protective capsule enclosing the eye.

Chapter 2 Medical Aspects

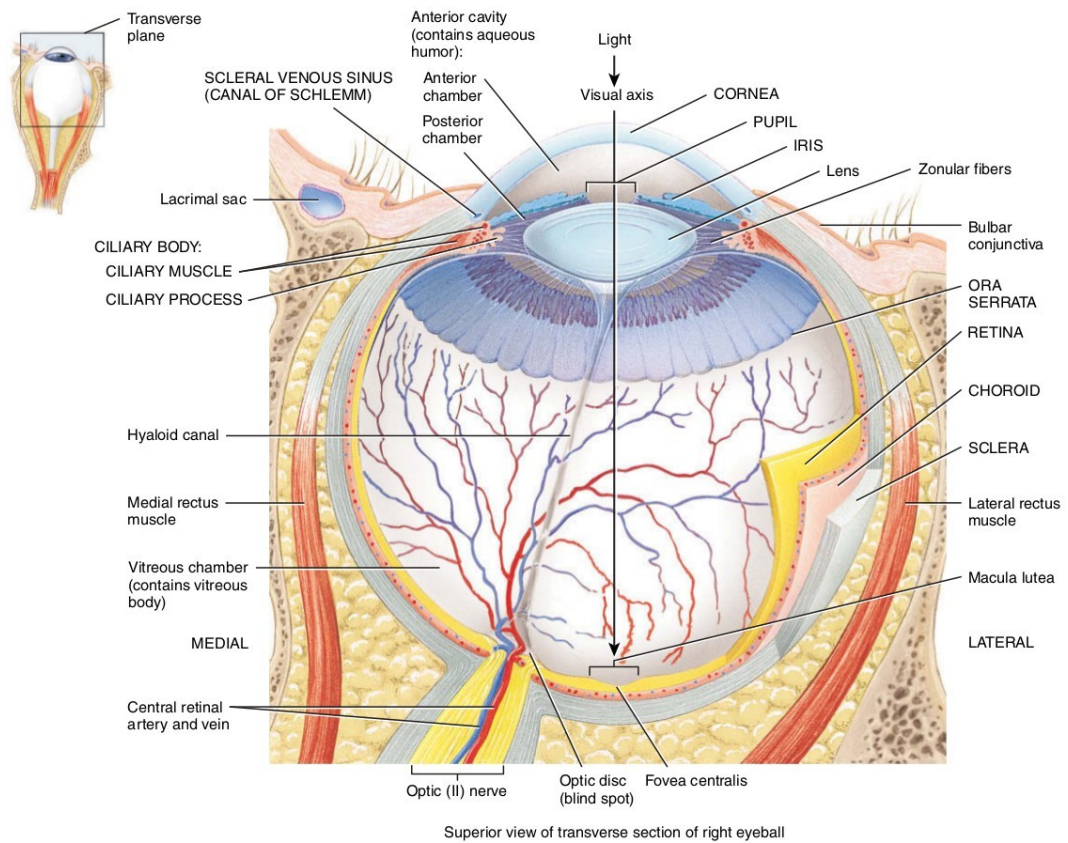


Figure 2.1: Superior view of transverse section of right eyeball [8].

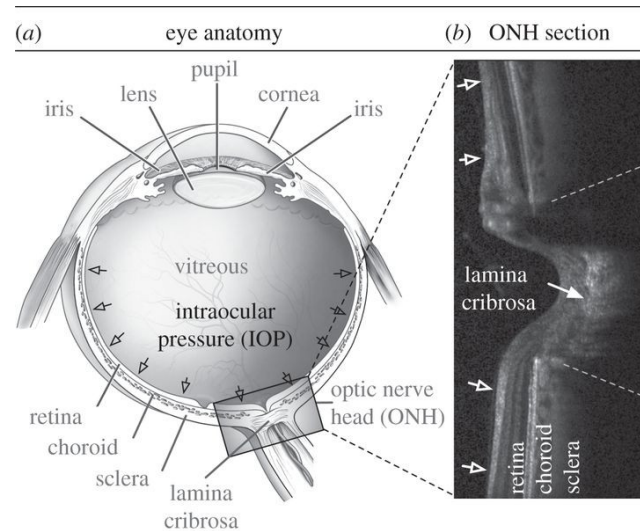


Figure 2.2: (a) Schematic of a human eye. (b) Cross section of a human ONH captured with optical coherence tomography. (Figure taken from [9].)

Cornea

The avascular cornea is the anterior transparent part of the outer coat. It is more curved than the sclera, therefore a slight *sulcus scleræ* marks the corneoscleral junction (*limbus*) [10]. It is thinner at its center than close to the *limbus*. For numerical values see Table 2.1.

The cornea not only admits light, but its covering tear film is also the major refractive surface of the eye. It helps focus light onto the retina. The cornea contributes between 65–75 percent of the eye's total focusing power.

Microscopically, the corneal tissue is arranged in five layers: (1) corneal epithelium (*epithelium anterius corneæ*); (2) anterior limiting lamina (*lamina limitans anterior*) (Bowman's layer); (3) *substantia propria* (stroma); (4) posterior limiting lamina (*lamina limitans posterior*) (Descemet's membrane) and (5) endothelium (*endothelium cameræ anterioris*) [11].

Table 2.1: Curvature and thickness of the cornea and sclera [12].

	Cornea	Sclera
Curvature r (mm)	6.8–8.5	11.5
Average curvature (mm)	7.8	
Thickness (µm)	520–670	300–1350

Sclera

The sclera is the posterior opaque part of the outer coat (it accounts for approximately 93 % of the ocular surface); it is a layer of dense connective tissue made up mostly of collagen fibers and fibroblasts. Together with the cornea, they determine the geometry of the eye and ensures its shape is not distorted when it moves [12]. The sclera serves as a site of attachment for the extrinsic eye muscles. At the junction of the sclera and cornea is an opening known as the scleral venous sinus (canal of Schlemm) which is filled with *aqueous humor* [8].

The sclera is thickest posteriorly (1–1.4 mm), decreasing gradually towards the equator to reach a minimum of 300 µm under the tendons of the recti. Going forwards from the insertions of the recti, it gradually increases in thickness once more to 800 µm at the *limbus* [12].

2.1.2 Vascular Tunic (*tunica vasculosa bulbi*)

The middle layer of the eyeball is the vascular tunic (also called the uvea, uveal layer, uveal tract). The three parts the uvea is composed of (posteroanterior): (1) choroid (*choroidea*); (2) ciliary body (*corpus ciliare*) and (3) *iris*.

Choroid

The choroid is highly vascularized and lines most of the internal surface of the sclera. Numerous blood vessels provide nutrients to the posterior surface of the retina. The choroid also contains melanocytes that produce the pigment melanin, which cause this layer to appear dark brown in color. Melanin in the choroid absorbs stray light rays, which prevents reflection and scattering of light within the eyeball. As a result, the image cast on the retina by the cornea and lens remains sharp and clear [8].

Layers of the choroid (see Figure 2.3): (1) suprachoroid (*lamina suprachoroidea*); (2) vessel layer, vascular stroma (*lamina vasculosa*); (3) choriocapillaris (*lamina choriocapillaris*) and (4) lamina vitrea *lamina basalis* or Bruch's membrane [11, 12].

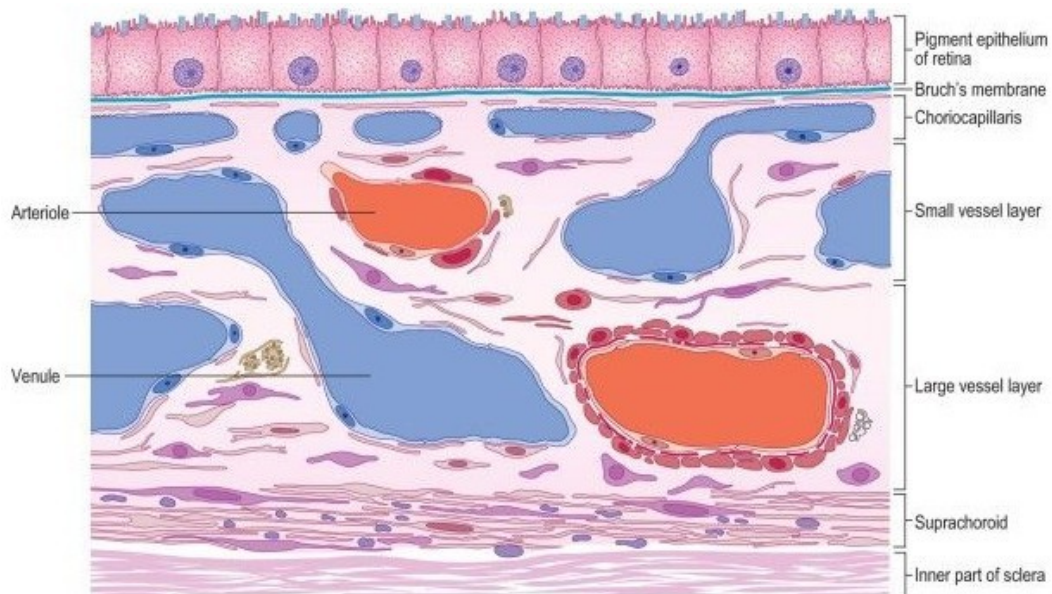


Figure 2.3: Drawing of a histological section through the choroid close to the posterior pole [12].

The external surface of the choroid is covered approximately 30 μm thick by the suprachoroid. It is composed of delicate non-vascular lamellæ, each one a network of fine collagen and elastic fibres, fibroblasts and melanocytes. In this layer long posterior ciliary arteries and ciliary nerves pass forward to the anterior uvea [12].

To the suprachoroid internal lies the vascular stroma, composed mainly of arteries and veins, but also some loose connective tissue containing melanocytes. The choroidal stroma can be divided into further layers based on the change in the calibre of the vessels (Haller's layer and Sattler's layer) [12].

The choriocapillaris is composed of large (up to 20 μm thick) densely packed capillaries. It provides nutrients to the outer five layers of the retina [12].

The Bruch's membrane is derived from the choriocapillaris and the retinal pigment epithelium between both it lies. Its function is thought to be related to the passage of fluid and solutes from the choroidal capillaries to the retina. This glassy, homogeneous layer values about 2–4 μm in diameter [12].

The vessels of the choroid have a rich autonomic vasomotor supply. The blood flow through the choroid is high, a feature probably associated with an intraocular pressure of 15–20 mmHg, which means that a venous pressure above 20 mmHg is required to maintain circulation. The choroidal perfusion rate exceeds that required to supply nutrients and may serve to cool the retina during exposure to bright light [12].

Ciliary Body

In the anterior portion of the vascular tunic, the choroid becomes the ciliary body. It extends from the *ora serrata*, the anterior margin of the retina, to a point just posterior to the junction of the sclera and cornea. The ciliary body contains melanocytes too, it appears dark brown in color. The ciliary body consists of ciliary processes and ciliary muscles [8].

The ciliary processes contain blood capillaries that secrete aqueous humor [8].

The ciliary muscle is a circular band of smooth muscle. Contraction or relaxation of the ciliary muscle changes the tightness of zonular fibers, which alters the shape of the lens, changing the refractive power of the lens (accommodation) [8, 12].

Iris

The iris is an adjustable diaphragm, between the cornea and the lens, around the pupil. It consists of melanocytes and circular and radial smooth muscle fibers. The iris is the colored portion of the eye. The iris is immersed in aqueous fluid. Due to the densely pigmented posterior double epithelium, it acts as a light stop. The size of the pupillary aperture is adjusted by two muscles, *dilator* and *sphincter pupillae* [8, 12].

On the one hand, the pupil have an important (but not sole) role in dark/light adaptation: the pupillary diameter varies from around 2 mm (bright light) to at least

8 mm (darkness), and has an even wider range under the influence of drugs. On the other hand, enhancing visual acuity by restricting light to the centre of the lens, and thereby decreasing the amount of spherical aberration, is at least as important function as of pupillary constriction [12].

2.1.3 Retina

The inner layer of the eyeball, the retina covers the posterior three-quarters of the eye. The surface of the retina serves as the only place in the body, where blood vessels can be viewed directly (with an *ophthalmoscope*) and examined for pathological changes [8].

The thickness of the retina varies from 100 μm at its edge to $\approx 300 \mu\text{m}$ at the foveal rim [12].

The place where the optic nerve (ON) exits the eyeball is called the optic disc/optic nerve head (ONH). Together with the ON the central retinal artery (CRA) and central retinal vein (CRV) are bundled. The branches of the CRA nourish the anterior surface of the retina; the CRV drains the blood through the optic disc.

Centred temporal and inferior to the disc lies the *macula* or *macula lutea* (approximate diameter 5–6 mm), the middle of which is composed of the *fovea* and *foveola*. The peripheral retina lies outside of the *macula* [12].

The retina can be divided into ten layers: this convention is based on the distribution of the diverse retinal cell types: epithelial, neural and glial cells. The ten layers of the retina are: (1) RPE (*stratum pigmenti retinæ*), (2) Rod and cone layer, (3) external limiting membrane (ELM) (*membrana limitans externa*), (4) outer nuclear layer (ONL) (*stratum granulosum externum*), (5) outer plexiform layer (OPL¹) (*stratum plexiforme externum*), (6) inner nuclear layer (INL) (*stratum granulosum internum*), (7) inner plexiform layer (IPL) (*stratum plexiforme internum*), (8) ganglion cell layer (GCL) (*stratum ganglionare*), (9) nerve fibre layer (NFL) and (10) ILM (*membrana limitans interna*).

Retinal pigment epithelium The RPE forms the outermost layer of the retina and therefore forms the boundary with the choroid, from which it is separated by the thick composite *basal lamina* (*Bruch's membrane*). It contains cuboidal pigment cells which absorb light reaching the retina but missing the photoreceptors: preventing stray light. The RPE has also the function of supplying the visual cells with nutrients.

Photoreceptor Layer The photoreceptor layer contains the photoreceptive outer segments and the outer part of the inner segments of rod and cone cells. Rods and cones are the two types of photoreceptor cells. Rods and cones are the first step in the process converting light into nerve impulses.

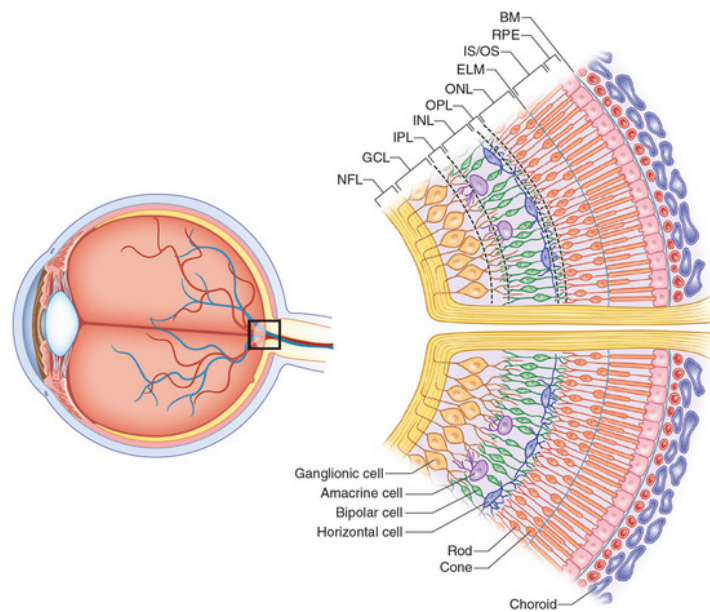


Figure 2.4: Cell layers of the retina. Figure taken from [13].

NFL: nerve fibre layer; GCL: ganglion cell layer; IPL: inner plexiform layer; INL: inner nuclear layer; OPL¹: outer plexiform layer; ONL: outer nuclear layer; ELM: external limiting membrane; IS: photoreceptor inner segment; OS: photoreceptor outer segment; RPE: retinal pigment epithelium; BM: Bruch's membrane.

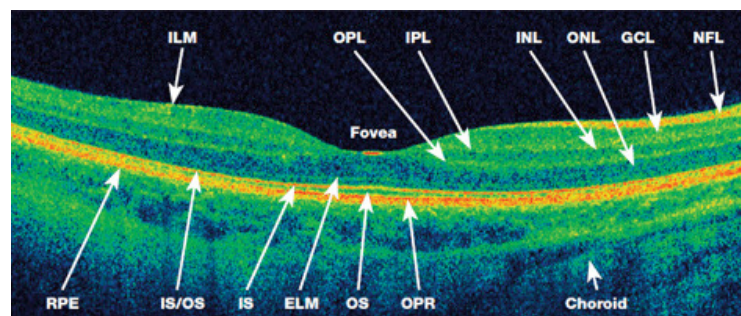


Figure 2.5: An HD-OCT scan of a healthy retina. Figure taken from [14].

ILM: inner limiting membrane; OPL¹: outer plexiform layer; IPL: inner plexiform layer; INL: inner nuclear layer; ONL: outer nuclear layer; GCL: ganglion cell layer; NFL: nerve fibre layer; RPE: retinal pigment epithelium; IS/OS: interface between IS and OS; IS: photoreceptor inner segment; ELM: external limiting membrane; OS: photoreceptor outer segment; OPR: outer photoreceptor/RPE complex.

Light is absorbed by rhodopsins, visual pigments consisting of a protein, opsin, that spans the membrane of the outer segment discs, bound to a light absorbing chromophore, retinal, which is an aldehyde of vitamin A₁. Such rhodopsins have gaussian-shaped absorption spectra with a point of maximum absorbance (λ_{\max}), indicating the wavelength at which they are most sensitive. Humans possess four different opsins resulting in four spectrally distinct visual pigments, one located within the rods ($\lambda_{\max} = 498 \text{ nm}$) and three within different populations of cones absorbing maximally at the short ($\lambda_{\max} = 420 \text{ nm}$), middle ($\lambda_{\max} = 534 \text{ nm}$) and longer wave ($\lambda_{\max} = 563 \text{ nm}$) end of the visible spectrum. The three cone classes are sometimes referred to as blue, green and red cones, but are better classed as S, M and L cones. Although cones populate the whole retina, their density is highest in the foveola: this area is entirely rod free. Going outwards from the foveola, rod numbers rise, reaching a peak density in a horizontal elliptic ring at the eccentricity of the optic disc, before declining once more toward the periphery.

Rods are responsible for vision in low light: they do not provide color vision, only black and white and all shades of gray in between.

Cones are responsible for color vision. There are three types of cones: cones sensitive to blue, green and red light. From the combination of cones of these three types, color vision results.

External limiting membrane The ELM separates the cell bodies of the photoreceptor cells from the photoreceptor layer.

Outer nuclear layer In the ONL are the rod and cone cell bodies and their nuclei located.

Outer plexiform layer The OPL¹ contains the synaptic processes of rod and cone cells, bipolar cells and horizontal cells.

Inner nuclear layer The INL gives place for the nuclei of bipolar, amacrin and horizontal cells. Bipolar cells transmit information from the photoreceptors to the ganglion cells. There are several classes of amacrin cells which serve a number of important functions in vision: they are, e. g. essential element in the rod pathway; furthermore they function as important modulators of photoreceptor signals. The horizontal cells play a role in sharpening contrast and maximising spatial resolution.

Inner plexiform layer The IPL synapse the bipolar, amacrin and ganglion cells. This plays an important role in the compression of image information before being transmitted to the visual cortex.

Ganglion cell layer In the GCL are the cell bodies, nuclei and initial segments of the ganglion cells located.

Nerve fibre layer The NFL contains the axons of retinal ganglion cells which run towards the ONH, the spot where they leave the eye and form the optic nerve. The axons in the NFL are unmyelinated, they get a myelin sheath only in the ONH.

Inner nuclear layer The INL is the boundary between vitreous body and the retina. It is formed by the end feet of Müller cells and astrocytes.

2.1.4 The Interior of the Eye, the Ocular Media

The lens divides the interior of the eye into two cavities: the anterior cavity (anteriorly to the lens) and the vitreous chamber (posteriorly, between the lens and the retina). The anterior cavity is divided into two chambers: the anterior chamber (between cornea and iris) and posterior chamber (between the iris and the lens). Both are filled with aqueous humor.

Within the vitreous chamber is the vitreous body, it occupies about four-fifths of the eyeball.

The pressure in the eye, called intraocular pressure (IOP), is produced mainly by the aqueous humor and partly by the vitreous body; normally it is about 16 mmHg. The IOP maintains the shape of the eyeball and prevents it from collapsing. Puncture wounds to the eyeball may cause the loss of aqueous humor and the vitreous body. This in turn causes a decrease in IOP, a detached retina, and in some cases blindness [8].

The ocular media, i. e. the cornea, aqueous humor, lens and vitreous body, serve to form an image on the retina by transmitting and refracting light.

Aqueous Humor

Aqueous humor is a transparent watery fluid that nourishes the lens and cornea. Aqueous humor continually filters out of blood capillaries in the ciliary processes of the ciliary body and enters the posterior chamber. It then flows forward between the iris and the lens, through the pupil, and into the anterior chamber. From the anterior chamber, aqueous humor drains into the scleral venous sinus (canal of Schlemm) and then into the blood. Normally, aqueous humor is completely replaced about every 90 minutes [8].

Lens

Behind the pupil and iris, within the cavity of the eyeball, is the lens. The lens is a transparent, encapsulated (enclosed by a clear connective tissue capsule), biconvex body bathed in aqueous humour [12]. Within the cells of the lens, proteins called crystallins, arranged like the layers of an onion, make up the refractive media of the lens, which normally is perfectly transparent and lacks blood vessels. It is held in position by encircling zonular fibers, which attach to the ciliary processes. The lens helps focus images on the retina to facilitate clear vision [8].

Vitreous Body

The vitreous body is a transparent jellylike substance that holds the retina flush against the choroid, giving the retina an even surface for the reception of clear images. It is colourless, consisting of approximately 99 % water, but is not entirely structureless. At its perimeter it has a gel-like consistency (100–300 µm thick); nearer the centre it contains a more liquid zone [12].

It occupies about four-fifths of the eyeball. Unlike the aqueous humor, the vitreous body does not undergo constant replacement. It is formed during embryonic life and consists of mostly water plus collagen fibers and hyaluronic acid. The vitreous body also contains phagocytic cells that remove debris, keeping this part of the eye clear for unobstructed vision. Occasionally, collections of debris may cast a shadow on the retina and create the appearance of specks that dart in and out of the field of vision. These vitreal floaters, which are more common in older individuals, are usually harmless and do not require treatment. The hyaloid canal is a narrow channel that is inconspicuous in adults and runs through the vitreous body from the optic disc to the posterior aspect of the lens. In the fetus, it is occupied by the hyaloid artery [8].

2.2 Eye Diseases

2.2.1 Glaucoma

After Cataract (74.9 %), glaucoma is the second leading cause of vision impairment in the world (in 2002: 12.3 % [15]). In 2010 60.5 Mio people suffered under open-angle glaucoma (OAG) or angle-closure glaucoma (ACG), the number could be increase to 79.6 Mio until 2020. In 2010 8.4 Mio people lived with bilateral blindness caused by OAG or ACG, 2020 this value is predicted to 11.2 Mio [5, 16].

It is a group of diseases where the optic nerve is damaged resulting in vision loss and blindness. In healthy eye, *aqueous humor* is circulating inside the front portion of the eye. To maintain a constant healthy eye pressure, a small amount of *aqueous*

humor is continually produced while an equal amount of this fluid flows out of the eye through *Schlemm's canal*. In glaucoma, the *aqueous humor* does not flow out of the eye properly therefore increasing the IOP. This increase in the IOP causes the damage to the optic nerve fibers.

We distinguish between primary and secondary glaucoma. Primary glaucoma is developed due to an unknown cause, while secondary glaucoma develops from a known cause, usually due to a serious eye injury, cataract, tumor, or diabetes. There exists also developmental (congenital, pediatric, infantile, childhood) glaucoma which occurs in babies and young children, caused by incorrect development of the eye's drainage system before birth [17].

There are several types of glaucoma ((1) primary open-angle glaucoma (POAG), (2) primary angle-closure glaucoma (PACG), (3) secondary glaucoma (SG) (both open-angle and angle-closure), (4) developmental glaucoma (DG) and (5) normal-tension glaucoma (NTG)), however the two most common are POAG, having a slow and insidious onset, and PACG, which is less common and tends to be more acute.

Open-angle glaucoma The angle where the iris meets the cornea is as wide and open as it should be (see Figure 2.6a). OAG is caused by the slow clogging of the drainage canals, resulting in increased eye pressure. It develops slowly and has symptoms and damage that are not noticed. It is a lifelong condition (also called *chronic glaucoma*) [18].

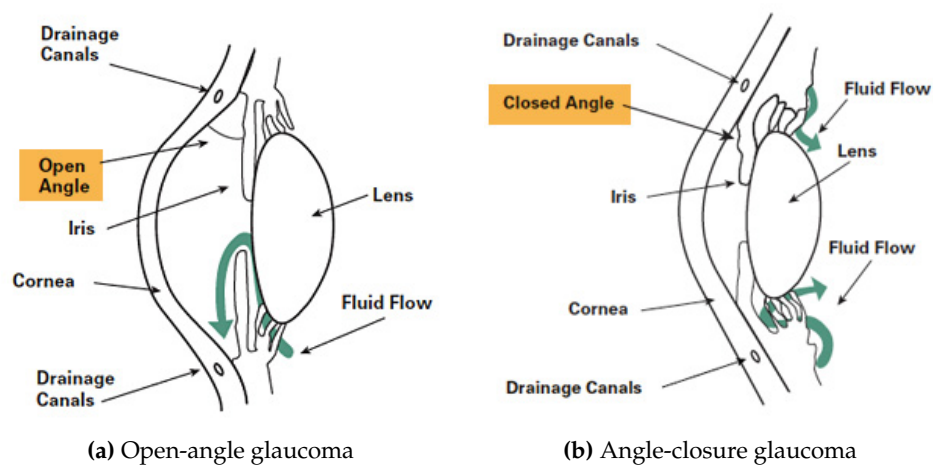


Figure 2.6: The two most common types of glaucoma are primary open-angle glaucoma and primary angle-closure glaucoma. In both cases the intraocular pressure increases, resulting in the damage of the optic nerve fibers. Picture taken from [18].

Angle-closure glaucoma The angle between the iris and cornea are closed or narrowed down, thus blocking the drainage canals (see Figure 2.6b). It develops very quickly and occurs a sudden rise in the IOP. It is also called *acute glaucoma* and demands immediate medical attention [18].

In normal-tension glaucoma (NTG) the IOP is not very high, but optic nerve damage and loss of vision still occur [18].

2.2.2 Age-related Macular Degeneration

AMD is a condition affecting older people, and involves the loss of the person's central field of vision (see Figure 2.7).

AMD ranks globally as third, as a cause of blindness in the world, and it is the primary cause in industrialized countries [19].

The severity is divided into early, intermediate and late types. The late type is additionally divided into "dry" (atrophic, non-exudative, non-neovascular) and "wet" (exudative or neovascular) forms, with the dry form making up 80–90% of the cases.

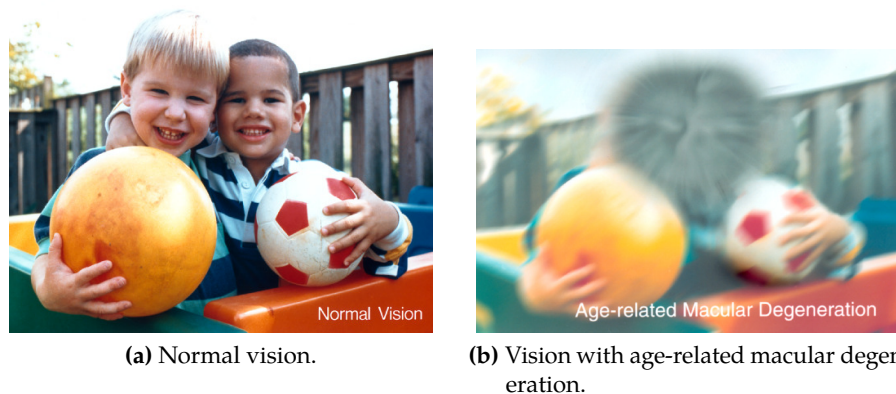


Figure 2.7: Comparing normal vision and vision affected by age-related macular degeneration. Figure taken from [20].

In "dry" AMD, central vision gradually diminishes because the pigmented layer atrophies and degenerates. There is no effective treatment. In about 10% of cases, dry AMD progresses to "wet" AMD, in which new blood vessels form in the choroid and leak plasma or blood under the retina. Vision loss can be slowed by using laser surgery to destroy the leaking blood vessels [8].

Drusen with associated visual acuity loss due to overlying RPE atrophy constitutes nonexudative AMD. There is absence of subretinal hemorrhage, subretinal fluid

and hard exudates. Choroidal neovascularization heralds the onset of exudative macular degeneration. Clinically this is associated with subretinal fluid, subretinal hemorrhage, hard exudates, pigment epithelium irregularity, pigment epithelium detachment, or subretinal greenish-gray lesion [21, p. 67].

Drusen are deposits of membranous debris, extracellular material between the RPE and its basement membrane (basilar laminar drusen) or between the RPE basement layer and the inner collagenous layer of Bruch's membrane (basilar linear drusen). Drusen lead to secondary Bruch's membrane thickening and RPE degeneration. Visual loss due to macular degeneration is the result of degeneration of photoreceptor cells and the choriocapillaris, which ensues soon after RPE [21, p. 70].

2.2.3 Diabetic Retinopathy (Diabetic Eye Disease)

DR is the most common cause of vision loss among people with diabetes, and the leading cause of vision impairment and blindness among working-age adults. In early stages there are usually no symptoms, the disease often progress unnoticed until it affects vision (see Figure 2.8).

Chronically high blood sugar from diabetes is associated with damage to the tiny blood vessels in the retina, leading to DR. DR can cause blood vessels in the retina to leak fluid or hemorrhage, distorting vision. One can differentiate between non-proliferative diabetic retinopathy (NDR), proliferative diabetic retinopathy (PDR) and diabetic macular edema (DME). In PDR, new abnormal blood vessels proliferate (increase in number) on the surface of the retina, which can lead to scarring and cell loss in the retina. DME is a consequence of DR: due to the leakage from the vessels, the macula swells. Although it is more likely to occur as DR worsens, DME can happen at any stage of the disease [22].

2.3 The Rat Eye (Differences to the Human Eye)

The rat's eye has the same basic structure and function as the human eye (see Figure 2.9) [23]. It is much smaller than the human eye, but the former's lens is much bigger related to the whole eye ball: Table 2.2 gives a quantitative comparison between human and rat eye dimensions; Figure 2.10 shows schematic ZEMAX illustrations comparing both.

Since the rat's eye has the same basic structure as the human eye, using the LCTI system it is possible to observe in vivo OFPs at pre-selected axial positions in rats.

Both, human and rat cornea allow visible and ultraviolet light to pass through. Both, human and rat pupil is highly variable in size. The rat pupil's diameter can vary from about 0.2 mm (under bright light) up to 1.2 mm (under dim light). This change



Figure 2.8: Comparing normal vision and vision affected by diabetic retinopathy and diabetic macular edema, respectively. Figure taken from [22].

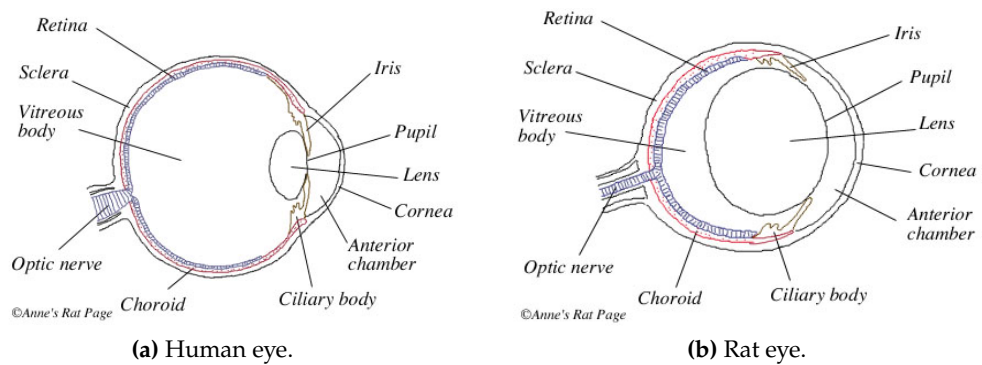


Figure 2.9: Schematical cross sections of the human and rat eye. Picture taken from [23].

in diameter takes only half a second [23]. In contrast to the human lens, which only let visible light to pass through, rat lenses allow all visible light plus almost 50 % of ultraviolet A light to pass through [24]. Unlike humans, rats seem to be unable to change their lenses' shape and so to change the focus of their lenses. On the one hand, rats are unable to see red, but on the other hand, their blue cones are sensitive to shorter wavelengths: rats can discriminate between greens, blues and ultraviolet. Rats have less cones as humans: only 1 % of the rat's retina (compared to 5 %) [23]. Rats do not have a fovea nor possess a macula [25, 26]. Rats have a poor visual acuity: a normally pigmented rat has about 20/600 and an albino has about 20/1200 [23].

In humans, the depth of focus (DOF) ¹ of the unaccommodated eye is from 2.3 meters to infinity. As a result of the rat's small eyes and poor visual acuity, rats have an enormous depth of focus: from 7 centimeters to infinity. One consequence of this difference is that humans perceive blurriness after a change of about 1/3 diopter, but rats require a 14 diopter change to perceive any blurriness [23].

Table 2.2: Dimensions of the rat and human eyes [12, 23, 27, 28]

	Human	Rat
Axial Eylength (mm)	24–32	6.3
Horizontal Diameter (mm)	23.5	6.4
Vertical Diameter (mm)	24	6.4
Corneal Radius (mm)	7.9	2.9
Refractive Power (Diopters), \approx	58	300
Depth of Focus (m)	2.3	0.1

Table 2.3: Parameters for Gullstrand's schematic eye and for the reduced schematic rat eye (rSRE) [29, 30].

Surface	Gullstrand's eye		rSRE	
	r (mm)	n	r (mm)	n
Anterior cornea	7.8		3	
Posterior cornea	6.5	1.4	2.7	1.4
Anterior lens	10.2	1.4	2.3	1.5
Posterior lens	-6	1.4	-2.3	1.7
Retina	-13.4	1.3	-3	1.3

¹Depth of focus is a property of a visual system that determines the range over which all objects are effectively at the same focal distance. It is determined by the size and acuity of the eye.

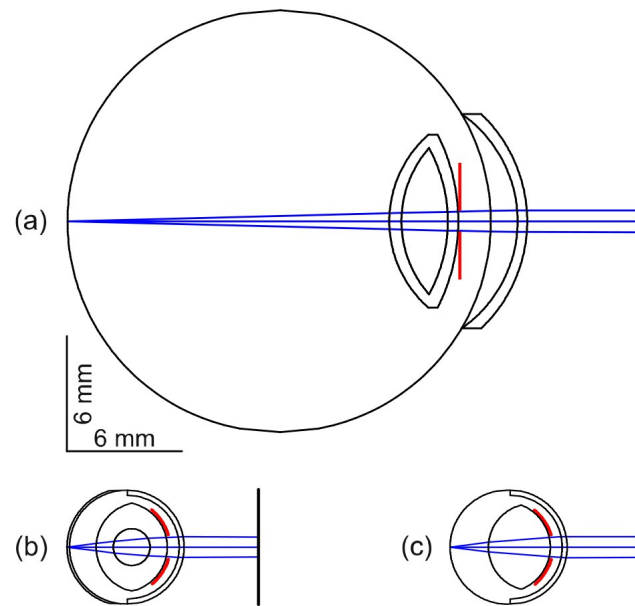


Figure 2.10: Schematic ZEMAX illustrations of the dimensions of the rat eye (b, c) in relation to the human eye (a). (a) Gullstrand's human schematic eye. (b) Hughes' schematic rat eye (c) Reduced schematic rat eye (rSRE). All eyes show a pupil diameter of 1 mm (red lines) [29].

2.3.1 Pigmented Rats

Normally pigmented rats have panoramic, blurry vision with faint greens, blues and ultraviolets. These colors may or may not be meaningful to the rats [31].

2.3.2 Albino Rats

Albinos have no pigment (no melanin) in their eyes: no pigments in the iris, but they also lack pigment deeper in the eye: without it, light inside the eye scatters. The albino's eye is flooded with light. Albino rats have very poor vision [31].

Chapter 3

Theory and Principles of LCTI

In this chapter, the theory, principles and main properties of light waves and of their interference are introduced and described. In the second part of the chapter, several techniques and methods are introduced which finally have been lead to the LCTI system, which is described in detail at the end of the chapter.

In the first part of the chapter, Bahaa E. A. Saleh and Malvin Carl Teich. *Fundamentals of Photonics*. 2nd ed. 2007, was used as a reference.

3.1 The Wave Equation

Mathematically, an optical wave can be described by a complex function of position $\mathbf{r} = (x, y, z)$ and time t , denoted $U(\mathbf{r}, t)$ and known as the *complex wavefunction*.

The *real wavefunction* $u(\mathbf{r}, t)$ is the real part of the complex wavefunction:

$$u(\mathbf{r}, t) = \text{Re}\{U(\mathbf{r}, t)\} = \frac{1}{2}[U(\mathbf{r}, t) + U^*(\mathbf{r}, t)], \quad (3.1)$$

where the symbol * signifies complex conjugation.

Like the real, the complex wavefunction must satisfy the *wave equation*

$$\nabla^2 U - \frac{1}{c^2} \frac{\partial^2 U}{\partial t^2} = 0, \quad (3.2)$$

where ∇^2 is the Laplacian operator, which is $\nabla^2 = \partial^2/\partial x^2 + \partial^2/\partial y^2 + \partial^2/\partial z^2$ in Cartesian coordinates. Any function that satisfies Eq. 3.2 represents a possible optical wave.

Because the wave equation is linear, the *principle of superposition* applies: if $U_1(\mathbf{r}, t)$ and $U_2(\mathbf{r}, t)$ represent possible optical waves, then $U(\mathbf{r}, t) = U_1(\mathbf{r}, t) + U_2(\mathbf{r}, t)$ also represents a possible optical wave.

3.1.1 Intensity

The optical intensity $I = I(\mathbf{r}, t)$, defined as the optical power per unit area (units of W/cm^2), is proportional to the average of the squared wavefunction:

$$I(\mathbf{r}, t) = 2\langle u^2(\mathbf{r}, t) \rangle. \quad (3-3)$$

The operation $\langle \cdot \rangle$ denotes averaging over a time interval much longer than the time of an optical cycle, but much shorter than any other time of interest.

3.1.2 Power

The optical power $P(t)$ (units of W) flowing into an area A normal to the direction of propagation of light is the integrated intensity

$$P(t) = \int_A I(\mathbf{r}, t) dA. \quad (3-4)$$

3.1.3 Energy

The optical energy (units of J) collected in a given time interval is the integral of the optical power over the time interval.

3.2 Monochromatic Waves

A monochromatic wave is represented by a wavefunction with harmonic time dependence. Both the amplitude and phase are generally position dependent, but the wavefunction is a harmonic function of time with frequency ν at all positions.

$$U(\mathbf{r}, t) = A(\mathbf{r})e^{[i\varphi(\mathbf{r})]}e^{(i2\pi\nu t)} = U(\mathbf{r})e^{i2\pi\nu t}. \quad (3-5)$$

3.2.1 Complex Amplitude

In Eq. 3.5 the time-independent factor $U(\mathbf{r}) = A(\mathbf{r})e^{[i\varphi(\mathbf{r})]}$ is referred to as the *complex amplitude* of the wave. At a given position \mathbf{r} , the complex amplitude $U(\mathbf{r})$ is a complex variable whose magnitude $|U(\mathbf{r})| = A(\mathbf{r})$ is the amplitude of the wave and whose argument $\arg\{U(\mathbf{r})\} = \varphi(\mathbf{r})$ is the phase.

3.2.2 Optical Intensity

The (cycle averaged) optical intensity of a monochromatic wave is proportional to the absolute square of its complex amplitude:

$$I(\mathbf{r}) \propto |U(\mathbf{r})|^2 \quad (3.6)$$

The intensity of a monochromatic wave does not vary with time.

3.2.3 Interference

When considering two monochromatic waves with time delay τ

$$U_1 = \mathbf{A}e^{i\omega t} \quad \text{and} \quad U_2 = \mathbf{B}e^{i\omega(t+\tau)} \quad (3.7)$$

the components of the complex amplitudes of the two waves can be written as

$$A_x = a_1e^{-ig_1}, \quad A_y = a_2e^{-ig_2}, \quad A_z = a_3e^{-ig_3}, \quad (3.8)$$

$$B_x = b_1e^{-ih_1}, \quad B_y = b_2e^{-ih_2}, \quad B_z = b_3e^{-ih_3}, \quad (3.9)$$

where g and h are of the form $(\mathbf{k} \cdot \mathbf{r} - \phi)$. \mathbf{k} is the propagation vector, \mathbf{r} represents the position of the point in space where the wave amplitudes are added, and ϕ is the phase constant.

Thus, the total electric field is:

$$U(\mathbf{r}, t) = U_1(\mathbf{r}, t) + U_2(\mathbf{r}, t + \tau) \quad (3.10)$$

It can be shown that the resultant wave's intensity is given by

$$I = I_1 + I_2 + \underbrace{2\langle \mathbf{E}_1 \cdot \mathbf{E}_2 \rangle}_{J_{12} \equiv \text{interference term}} \quad (3.11)$$

where I_1 and I_2 are the intensities of each wave. If the interference term is zero at all positions, the two waves are called incoherent.

In an experimental setup consider the same *phase difference* δ

$$g_1 - h_1 = g_2 - h_2 = g_3 - h_3 = \delta = \frac{2\pi}{\lambda_0} \Delta S, \quad (3.12)$$

where λ_0 is the wavelength in vacuum, and ΔS is the optical path length (OPL²) difference for the two waves.

The interference term can be expressed [30] as

$$\begin{aligned} J_{12} &= 2\langle \mathbf{E}_1 \cdot \mathbf{E}_2 \rangle = \frac{1}{2}[\mathbf{A} \cdot \mathbf{B}^* + \mathbf{A}^* \cdot \mathbf{B}] \\ &= a_1b_1 \cos(g_1 - h_1) + a_2b_2 \cos(g_2 - h_2) + \\ &\quad + a_3b_3 \cos(g_3 - h_3) \\ &= (a_1b_1 + a_2b_2 + a_3b_3) \cos \delta. \end{aligned} \quad (3.13)$$

Using Maxwell's equations it can be shown that light waves propagating in free space and polarized orthogonally to each other will not interfere. Since only parallel polarized waves interfere with each other, it is supposed that light is linearly polarized in the x -direction and the waves propagating in the z -direction.

$$a_2 = a_3 = b_2 = b_3 = 0, \quad (3.14)$$

thus,

$$I_1 = \frac{1}{2}a_1^2, \quad (3.15)$$

$$I_2 = \frac{1}{2}b_1^2, \quad (3.16)$$

$$2\langle \mathbf{E}_1 \cdot \mathbf{E}_2 \rangle = J_{12} = a_1 b_1 \cos \delta = 2\sqrt{I_1 I_2} \cos \delta, \quad (3.17)$$

and the total intensity

$$I = I_1 + I_2 + 2\sqrt{I_1 I_2} \cos \delta. \quad (3.18)$$

One can see that the value of the total intensity varies between

$$I_{min} = I_1 + I_2 - 2\sqrt{I_1 I_2} \cos \delta \quad (\text{if } |\delta| = \pi, 3\pi, 5\pi, \dots)$$

and

$$I_{max} = I_1 + I_2 + 2\sqrt{I_1 I_2} \cos \delta \quad (\text{if } |\delta| = 0, 2\pi, 4\pi, \dots)$$

If both waves have the same amplitude, the total intensity can be rewritten as [33]

$$I = 4I_1 \cos^2 \frac{\delta}{2}. \quad (3.19)$$

3.3 Non-monochromatic Light

Section 3.2.3 covered the interference of monochromatic light produced by a point source. Any real light wave is finite, and hence, non-monochromatic. In general, a light beam contains many finite waves or "wavelets".

Although a polychromatic wave is described by a wavefunction $u(\mathbf{r}, t)$ with non-harmonic time dependence, it may be expanded as a superposition of harmonic functions, each of which represents a monochromatic wave.

Fourier methods permit the expansion of an arbitrary function of time $u(t)$, representing the wavefunction $u(\mathbf{r}, t)$ at a fixed position \mathbf{r} , as a superposition integral of harmonic functions of different frequencies, amplitudes, and phases:

$$u(t) = \int_{-\infty}^{\infty} v(\nu) e^{i2\pi\nu t} d\nu, \quad (3.20)$$

where $v(\nu)$ is determined by carrying out the Fourier transform:

$$v(\nu) = \int_{-\infty}^{\infty} u(t)e^{-i2\pi\nu t} dt. \quad (3.21)$$

It is convenient to represent the real function $u(t)$ by a complex function:

$$U(t) = 2 \int_0^{\infty} v(\nu)e^{i2\pi\nu t} d\nu \quad (3.22)$$

that includes only the positive-frequency components (multiplied by a factor of 2), and suppresses all the negative frequencies. The real function $u(t)$ can be determined from its complex representation $U(t)$ by simply taking the real part,

$$u(t) = \text{Re}\{U(t)\} = \frac{1}{2}[U(t) + U^*(t)]. \quad (3.23)$$

The complex function $U(t)$ is known as the *complex analytic signal*.

In fact, the complex representation of a polychromatic wave is simply a superposition of the complex representations of each of its monochromatic Fourier components.

The complex analytical signal corresponding to the wavefunction $u(\mathbf{r}, t)$ is called the complex wavefunction $U(\mathbf{r}, t)$. Since each of its Fourier components satisfies the wave equation, so too does the complex wavefunction $U(\mathbf{r}, t)$:

$$\nabla^2 U - \frac{1}{c^2} \frac{\partial^2 U}{\partial t^2} = 0. \quad (3.24)$$

An arbitrary optical wave is described by a wavefunction $u(\mathbf{r}, t) = \text{Re}\{U(\mathbf{r}, t)\}$, where $U(\mathbf{r}, t)$ is the complex wavefunction.

3.3.1 Optical Intensity

For random light, $U(\mathbf{r}, t)$ is a random function of time and position. The intensity $|U(\mathbf{r}, t)|^2$ is therefore also random. The *average intensity* is then defined as

$$I(\mathbf{r}, t) = \langle |U(\mathbf{r}, t)|^2 \rangle, \quad (3.25)$$

where the symbol $\langle \cdot \rangle$ denotes an ensemble average over many realizations of the random function.

3.3.2 Interference

U_1 and U_2 are two partially coherent waves. At a given position \mathbf{r} and time t , the intensities of the two waves are $I_1 = \langle |U_1|^2 \rangle$ and $I_2 = \langle |U_2|^2 \rangle$, whereas their cross-correlation is described by the statistical average $G_{12} = \langle U_1^* U_2 \rangle$, along with its normalized version

$$g_{12} = \frac{\langle U_1^* U_2 \rangle}{\sqrt{I_1 I_2}}. \quad (3.26)$$

When the two waves are superposed, the average intensity of their sum is

$$\begin{aligned} I &= \langle |U_1 + U_2|^2 \rangle = \langle |U_1|^2 \rangle + \langle |U_2|^2 \rangle + \langle U_1^* U_2 \rangle + \langle U_1 U_2^* \rangle \\ &= I_1 + I_2 + G_{12} + G_{12}^* = I_1 + I_2 + 2\text{Re}\{G_{12}\} \\ &= I_1 + I_2 + 2\sqrt{I_1 I_2} \text{Re}\{g_{12}\}. \end{aligned} \quad (3.27)$$

We thus obtain the interference equation

$$I = I_1 + I_2 + \underbrace{2\sqrt{I_1 I_2} |g_{12}| \cos \varphi}_{J_{12} \equiv \text{interference term}}, \quad (3.28)$$

where $\varphi = \arg\{g_{12}\}$ is the phase of g_{12} .

3.3.3 Visibility

The strength of the interference is measured by the *visibility* V (also called the modulation depth or the contrast of the interference pattern) [32, p. 420]:

$$V = \frac{I_{max} - I_{min}}{I_{max} + I_{min}}, \quad (3.29)$$

where I_{max} and I_{min} are, respectively, the maximum and minimum values that I takes as the phase φ is varied. Since $\cos \varphi$ stretches between 1 and -1 , inserting the interference equation into Eq. 3.29 yields

$$V = \frac{2\sqrt{I_1 I_2}}{I_1 + I_2} |g_{12}|. \quad (3.30)$$

The visibility is therefore proportional to the absolute value of the normalized cross-correlation $|g_{12}|$. In the special case when the intensities of the two waves are the same, i.e. $I_1 = I_2$, this simplifies to

$$V = |g_{12}| \quad (3.31)$$

3.4 Coherence

3.4.1 Temporal Coherence

Consider the fluctuations of *stationary* light at a fixed position \mathbf{r} , as a function of time. The stationary random function $U(t)$ has a constant intensity $I = \langle |U(t)|^2 \rangle$.

For two non-monochromatic waves with time delay τ the so called *temporal coherence function* is introduced:

$$G(\tau) = \langle U^*(t)U(t + \tau) \rangle \quad (3.32)$$

$G(\tau)$ is a function with Hermitian symmetry, $G(-\tau) = G^*(\tau)$; the intensity (see Eq. 3.25) is equal to $G(\tau)$ when $\tau = 0$:

$$I = G(0). \quad (3.33)$$

For two non-monochromatic waves with time delay τ the so called *complex degree of temporal coherence* is introduced:

$$g(\tau) = \frac{G(\tau)}{G(0)} = \frac{\langle U^*(t)U(t + \tau) \rangle}{\langle U^*(t)U(t) \rangle}. \quad (3.34)$$

$|g(\tau)|$ is called the *degree of coherence*, it is a measure of the degree of correlation between $U(t)$ and $U(t + \tau)$, and its absolute value cannot exceed unity:

$$\text{For } |g(\tau)| = \begin{cases} 1 \\ 0 \\ > 0 \text{ and } < 1 \end{cases} \quad \text{the light is } = \begin{cases} \text{first-order coherent} \\ \text{incoherent} \\ \text{partially coherent} \end{cases} .$$

3.4.2 Coherence Time and Coherence Length

In a Michelson interferometer (see Figure 3.1a) the beam from the light source (LS) is split into two parts by a semi-transparent mirror (beam-splitter). The two beams are reflected from the two mirrors (M1 and M2), are reunited back at the beam-splitter and are measured. Since the beams travel different (optical) distances, alternating interference fringes can be observed. Because the interfering light waves differ in their time origin, the coherence measured by the Michelson interferometer is called *temporal coherence*. To characterize the temporal coherence, the *coherence time* τ_c is introduced: within the time τ_c , the light maintains its phase.

In general, τ_c is the width of the function $|g(\tau)|$. For $\tau < \tau_c$ the fluctuations are “strongly” correlated whereas for $\tau > \tau_c$ they are “weakly” correlated. Although

the definition of the width of a function is rather arbitrary (e.g., 1/e-width, half-maximum width), the power-equivalent width is commonly used as the definition of coherence time:

$$\tau_c = \int_{-\infty}^{\infty} |g(\tau)|^2 d\tau \quad (3.35)$$

Coherence time is fundamentally related to spectral width. The precise relation depends on the shape of the spectral line, but from the Fourier uncertainty relation a first approximation of the coherence time can be calculated [32, 34]:

$$\Delta\nu\tau_c \approx 1, \quad (3.36)$$

where $\Delta\nu$ is the full width at half maximum (FWHM) *linewidth* (*spectral width*).

The corresponding *coherence length* (l_c) is defined [30, 34, 35] by

$$l_c = c\tau_c \approx \frac{c}{\Delta\nu} = \frac{\lambda_0^2}{\Delta\lambda_0} \quad (3.37)$$

where c is the speed of light, λ_0 is the mean wavelength and $\Delta\lambda_0$ is the FWHM bandwidth of the light source.

For a Gaussian-shaped spectrum the coherence time τ_c^G

$$\tau_c^G = \frac{4 \ln 2}{\pi} \frac{1}{\Delta\nu} \quad (3.38)$$

and the corresponding *round-trip coherence length* (l_c^G) (because of the backscattering configuration)

$$l_c^G = \frac{c\tau_c^G}{2} = \frac{c2 \ln 2}{\pi} \frac{1}{\Delta\nu} = \frac{2 \ln 2}{\pi} \frac{\lambda_0^2}{\Delta\lambda_0}. \quad (3.39)$$

For the observation of interference fringes, the path difference between two beams (e.g. in a Michelson interferometer) must be smaller than the coherence length of the light. When the difference of optical path is greater than the coherence length, interference can not be observed.

3.5 Optical Path Difference and Optical Path Length

Optical path difference (OPD) corresponds to the phase shift that is induced between two previously coherent sources when passed through different optical media.

The OPD can be calculated from the following equation:

$$\text{OPD} = d_1n_1 - d_2n_2, \quad (3.40)$$

where d_1 and d_2 are the distances of the ray passing through medium 1 or 2, n_1 is the greater refractive index and n_2 is the smaller refractive index.

OPL² is the product of the geometric length d of the path light follows through a system, and the index of refraction of the medium through which it propagates:

$$\text{OPL} = nd. \quad (3.41)$$

If a wave is traveling through several different media, then the optical path length of each medium can be added to find the total optical path length (TOPL).

3.6 Dynamic Interferometric Length Measurement Technique

In the *dynamic interferometric length measurement technique* (see Figure 3.1), that uses light of high temporal coherence, one of the interferometer mirrors is moved over the distance d to be measured. The distance d can be obtained from the number of fringes N which pass the photodetector[35] (see Figure 3.1b):

$$N = 2 \cdot \frac{d}{\lambda} \quad \Rightarrow \quad d = \frac{N \cdot \lambda}{2} \quad (3.42)$$

This technique is widely used in industrial metrology. In medicine and biology this technique cannot be used because an interferometer mirror cannot be moved across the eye or other tissues. This and the inherent instability of these living structures raise a need for other techniques.

3.7 Partial Coherence Interferometry

To overcome the problem described above, a technique called partial coherence interferometry (PCI) (see Figure 3.2) has been introduced. The measurement of the eye length as well as the determination of intraocular distances are based on PCI. In this technique, light of high spatial coherence (i.e. collimated), but low temporal coherence is used [1, 36].

In PCI there is only one measurement mirror, mounted on a stepping motor. The light beam emitted by the light source (LS) is split into two components by a beam splitter cube (BSC). The one component is guided to the mirror, the other one illuminates the object. This beam is reflected at light remitting sites of the object. After backscattering from the measurement mirror and from the object, the two beams are reunited. The signal exits the interferometer and comes to the photodetector (PD). An interference can be observed if the OPD of the two beams lies within the coherence length.

The weakness of these technique is the high sensitivity to movements of the object during the time needed for moving the reference mirror. To conquer this problem the reference mirror has to be moved at very high speed, or the self-compensating dual-beam technique has to be used [30, 37].

3.8 Dual Beam PCI

In *dual beam PCI* (see Fig. 3.3) the light beam (emitted by a superluminescent diode (SLD)) is split up by a Michelson interferometer into two components. The one part (*reference arm*) is guided to a fixed mirror (reference mirror, M_R). The other component is guided to the measurement mirror M , which is mounted to a stepping motor (*measurement arm*), hence the arm length difference d between measurement and reference arm is variable. After the components exit the interferometer, they have a path difference, which equals twice the arm length difference d .

This dual beam is guided onto the eye and reflected at various sites (which are boundaries between regions with different refractive indices of the eye). Each component is further split into subcomponents reflected — among others — at the anterior side of the cornea, at the inner limiting membrane, the retinal pigment epithelium and the Bruch's membrane [30]. These reflected components are then superimposed at the photodetector.

Intraocular distances can be measured by moving the measurement mirror at a constant speed. Every time when the OPD between the two arms matches an optical distance in the eye, the respective subcomponents of the beam will interfere, leading to an interference signal at the photodetector (PD). The real envelope of the photodetector (PD) signal is recorded on a computer. These recorded curves are called *optical A-scans* and contain information about the intraocular distances: every peak corresponds to a reflecting layer in the eye, and the respective optical distances can be determined directly. The resolution is in the order of l_c' .

The gross longitudinal eyemovements have no impact on the match between the arm length difference of the interferometer and the intraocular distances; so it can be used for *in vivo* measurements, as it has been reported [30]: for measurements of optical distances in the anterior eye, in the posterior eye, and for the measurement of the axial eye length.

There is a commercially available product, the IOL Master (from Zeiss, see Figure 3.4), which is based on this technique.

One of the main noise sources in interferometry is mechanical $1/f$ noise. To achieve a shot-noise limited detection, the most straightforward way in optics is to use the

Doppler effect [30, 35, 37]. The reference mirror is moved at constant speed v , which produces a Doppler shift Δf of the light frequency of the beam:

$$\Delta f = 2f_0 \frac{v}{c} = 2 \frac{v}{\lambda_0} \quad . \quad (3.43)$$

The corresponding photodetector signal is modulated with this Doppler shift [1]. It is band-pass filtered with $2f_0 v/c$ as central frequency, then rectified and low-pass filtered, hence the output signal of the filter is the envelope of the oscillating part of the photodetector signal [30, 35, 37].

3.9 Spectral Interferometry

This technique is based on the Fourier-transform relation between the intensity spectrum of a light wave and its path-difference dependent degree of coherence. A spatially coherent broadband light source together with a spectrometer has to be used, however no mechanical scanning (like in PCI) is required.

3.10 Optical Coherence Tomography (OCT)

Tomography is based on the reconstruction of cross-sectional images of an object from its projections. The word is derived from the Greek word *tomos* which stays for “cut” or “section”. The term *tomography* is also used whenever two-dimensional data are derived from a three-dimensional object to obtain a slice image of the internal structure.

3.10.1 Low-coherence Interferometry

Optical coherence tomography (OCT) uses interferometry to perform high-resolution measurements of light echoes. If a coherent (narrow linewidth) light source is used, interference will be observed over a wide range of path length differences [38]. To detect optical echoes, a low-coherence (broad bandwidth) light source is required. When low-coherence light is used, interference is only observed when the path lengths of the reference and measurement arms are matched to within the coherence length of the light.

Low coherence interferometry (LCI) has the advantage that it can be performed with continuous wave light sources, without the need for short pulses. In LCI, the axial resolution is inversely proportional to the bandwidth of the light source, therefore broad-bandwidth light sources are required to achieve high axial resolution.

The axial measurements of backscatter vs. depth using LCI provided the foundation for OCT.

3.10.2 OCT

Optical coherence tomography (OCT) (see Fig. 3.5) generates cross-sectional or three-dimensional images by measuring the echo time delay and magnitude of backscattered or backreflected light [39]. The reflectivity profile, called an A-scan, contains information about the spatial dimensions and location of structures within the item of interest. A cross-sectional tomograph (B-scan) may be achieved by laterally combining a series of these axial depth scans (A-scans).

There are three different types of interferometric detection techniques, which can be used to measure echo time delays. Early OCT instruments used a low-coherence light source and an interferometer with a scanning reference delay arm. This method of LCI can be viewed as time domain detection [38].

Time domain optical coherence tomography (TD-OCT) is based on PCI. This method generates 2D images (*B-scans*). A scanning mirror is used to shift the probe beam to different transversal positions of the object under study. There are two kinds of scanning schemes: the longitudinal (conventional) and the transversal. In the former, the position of the lateral scanning mirror is held constant during a single A-scan. Cross-sectional images are generated by performing a series of axial scans (A-scans) at different transverse positions to generate a two-dimensional data set (B-scan). In the latter, the probe beam is moved by the scanning mirror over the lateral scanning range while holding the measurement mirror of the interferometer at the same longitudinal position [38].

However, it is also possible to perform detection in the Fourier domain by measuring the interference spectrum. There are two types of Fourier domain detection. One approach, known as spectral/Fourier domain OCT, uses an interferometer with a low-coherence light source and measures the interference spectrum using a spectrometer and a high-speed, line scan camera. The second approach, known as swept source/Fourier domain OCT, or optical frequency domain imaging (OFDI), uses an interferometer with a narrow-bandwidth, frequency-swept light source and detectors, which measure the interference output as a function of time [38].

In Fourier domain optical coherence tomography (FD-OCT) no mechanical depth scan is performed. The light exiting the interferometer is dispersed by a spectrometer and its spectral distribution is recorded via a CCD line camera. The oscillating part of the intensity which exits the interferometer is the convolution of the illuminating beam with the light remitting structure of the sample. The depth structure can be obtained by a Fourier transform of the measured spectrum [38].

3.11 Measurement of Ocular Blood Flow and Ocular Fundus Pulsations

OBF is a global measure that includes retinal and choroidal flow. Many diseases of the ocular fundus originate from pathologic changes in the blood supply. For this reason it is important to study OBF. Until the early 1970s OBF could only be estimated by means of *fundus fluorescence cinematography*. Other techniques are the *blue field entoptic technique*, the *laser speckle technique* and techniques which can only be applied in animals, like the injection of radioactively labelled and colored microspheres. All these techniques have specific limitations and their choice must depend on the aim underlying the study to be performed [35].

3.11.1 Laser Doppler Velocimetry (LDV)

Laser dopler velocimetry (LDV) is a technique in which the velocity of a fluid is calculated from the measured doppler frequency shift of a laser beam scattered from tracer particles in the fluid [41]. Since 1972 this technique has been used for measuring the *retinal blood flow*.

The technique can only be used for the quantification of retinal macrocirculation, i.e. to measure blood flow velocity in large retinal vessels (with a diameter in range of $\approx 80\text{--}200\ \mu\text{m}$). In addition the velocity measured is the velocity of the erythrocytes, which is substantially larger than the plasma velocity. For quantification of retinal microcirculation only the blue field entoptic technique and the digital scanning laser fluorescein angiography are available[35].

3.11.2 Pulsatile Ocular Blood Flow by Laser Interferometry

Whereas LDV can readily be used on retinal blood vessels, choroidal blood vessels are very difficult to access, since they are located behind the outer retina. Several techniques are used to get information about choroidal blood flow (based on angiography, color Doppler imaging, pneumotometry). The first method based on laser interferometry was described by Fercher [42] and Schmetterer [43]. This technique allows for measuring pulsations of the fundus surface. This ocular fundus pulsation (OFP), which is the distance variation between cornea and retina during the cardiac cycle, is caused by the arterial blood pressure amplitude [1, 42]. Because of the pulsatile inflow into the arteries and the continuous outflow via the venes, the volume change of the bulbus is[35]:

$$\Delta V = A_{arteries} \cdot \int_0^T v_{arteries}(t) \cdot dt - A_{veins} \cdot v_{veins} \cdot T \quad (3.44)$$

where A is the vessel's cross-section, v the velocity, and T is the duration of the cardiac cycle.

The eye is illuminated by a collimated laser beam, that is of long coherence length. There are four reflections corresponding to the four Purkinje reflexes (also called Purkinje-Sanson images). The first and the second Purkinje images are the reflections from the outer and from the inner surface of the cornea. The third and fourth ones are the reflections from the outer (anterior) and from the inner (posterior) surface of the lens. The reflection from the front surface of the cornea is the most prominent, another dominant light beam is remitted from the retinal pigment epithelium (RPE) or Bruch's membrane. The former one is close to spherical while the latter is a plane wave. These two beams generate non-localized concentric circular interference fringes similar to Newton's fringes. The optimal contrast is 30–40 mm in front of the subject's eye [1, 30, 35].

The fundus pulsations lead to a corresponding shift of these fringes and can be determined by counting the fringes moving through a fixed point. The change in optical distance $\Delta L(t)$ can be calculated by [1, 30]

$$\Delta L(t) = \Delta N(t) \frac{\lambda}{2}, \quad (3.45)$$

where $\Delta N(t)$ is the change in interference order and λ is the wavelength of the light source. The maximum distance change during the cardiac cycle is called *fundus pulsation amplitude (FPA)*.

A linear CCD array (LCCD) acquires a full temporal record of the pulsation. The spatio-temporal display of the interference fringes is the so called *synthetic interferogram*, which is the result of plotting each LCCD's readout over time (see Figure 3.6).

This technique allows only the observation of the strongest reflecting layer [1].

3.12 Low-Coherence Tissue Interferometry (LCTI)

It is often required (in study of macular edema or observation of eye elongation during myopia development) to measure other intraocular layers than the strongest reflecting one (like with the fundus pulsation interferometer presented in the previous section). Due to this reason the technique of low-coherence tissue interferometry (LCTI) has been employed, combining a dual beam PCI (measurement of intraocular (IO) distances) with a fundus pulsation interferometer (measuring and recording fundus pulsation). LCTI (see Fig. 3.7) allows for the measurement of distance changes between the cornea and a pre-selected reflecting layer at the posterior pole of the eye in human subjects [1].

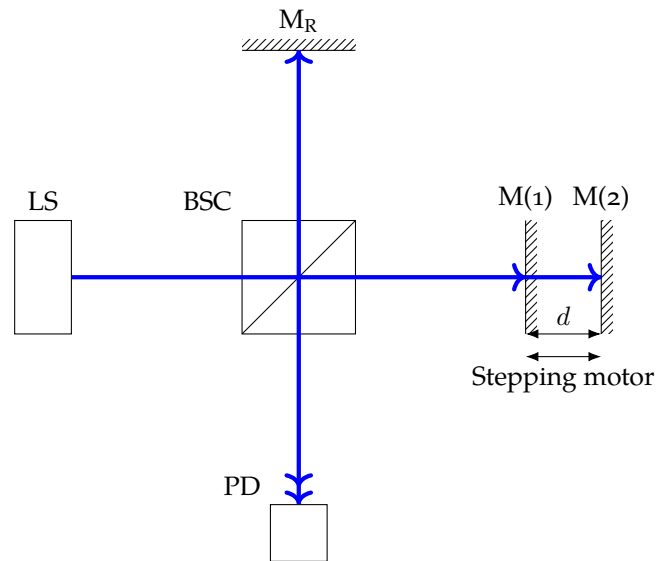
3.12.1 Description of the System

A light source of low temporal coherence (a *SLD*) is used for illumination. The beam is split by a Michelson interferometer into two components. The interferometer has an arm length difference d which is variable: one of the mirrors (the measurement mirror) is mounted on a stepping motor. After the components exit the interferometer, they have a path difference, which equals twice the arm length difference d .

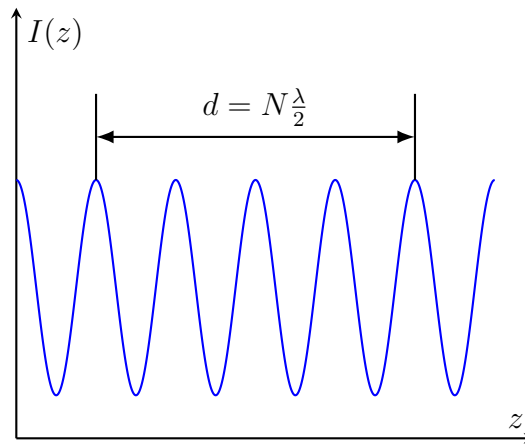
An additional (polarizing) beam splitter with a quarter wave plate (QWP) is built in the detection arm, directly before the subject's eye. The polarizing beam splitter cube (PBSC) splits randomly polarized beams into two orthogonal, linearly polarized components. S-polarized light is reflected at a 90 degree angle, while P-polarized light is transmitted. In this way, the S-polarized part of the beam (which is due the polarization controller only a very small part) is lost, the other part illuminates the eye and is reflected from the various sites. Since the beam passes the QWP twice, it reaches the PBSC the second time as S-polarized light after reflection at the eye. Hence, this beam is reflected towards the detection part of the system (see Figure 3.9 and 3.10).

For observation of fundus pulsations, the reflected beam is directed towards a linear CCD array (LCCD) array, whereas for the length measurement it is directed toward the photodetector (PD), an avalanche photodiode (APD) module.

This optical setup allows for real-time assessment of tissue pulsations as long as the optical distances between the two interferometer arms and the optical distance between the two ocular surfaces are within the coherence length of the light source[1].



(a) Michelson interferometer. LS: light source; BSC: beam splitter cube; M_R : reference mirror; $M(1)$ and $M(2)$: measurement mirror at position (1) and (2); PD: photodetector; d : distance to be measured.



(b) Detector signal. d : distance to be measured; N : number of fringes which passed the photodetector; λ : wavelength of the light source.

Figure 3.1: Dynamic length measurement interferometry.

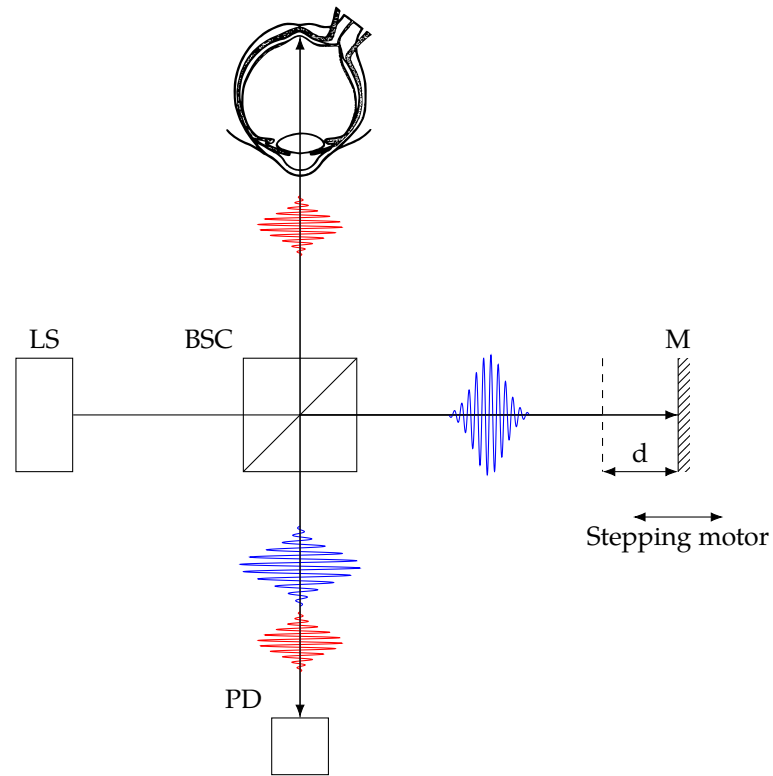


Figure 3.2: Partial Coherence Interferometry (PCI).

LS: light source; BSC: beam splitter cube; M: measurement mirror;
PD: photodetector; d : distance to be measured.

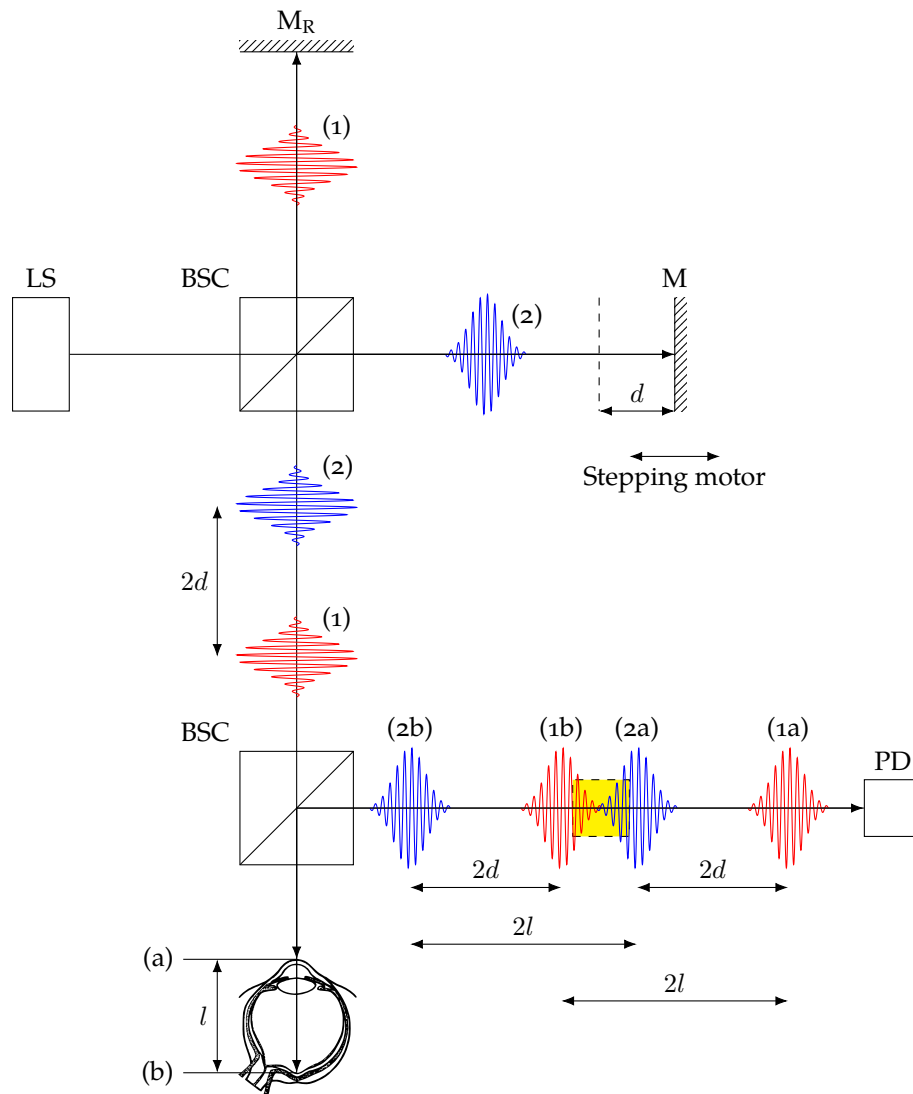


Figure 3.3: Schematic diagram of a dual beam partial coherence interferometer. LS: light source; BSC: beam splitter cube; M_R : reference mirror; M : measurement mirror; PD: photodetector; (a) and (b): various reflecting sites in the eye; l : distance between (a) and (b); (1) and (2) are the two components of the beam, split up by the Michelson interferometer; (1a), (1b), (2a) and (2b) are subcomponents reflected at the various sites of the eye, respectively.



Figure 3.4: The commercially available product, IOL master (Zeiss, Jena, Germany) is based on dual beam PCI technique. Picture is taken from http://www.vision-surgery.com/images/iolmaster_los_angeles.jpg, accessed on 2017-02-09.

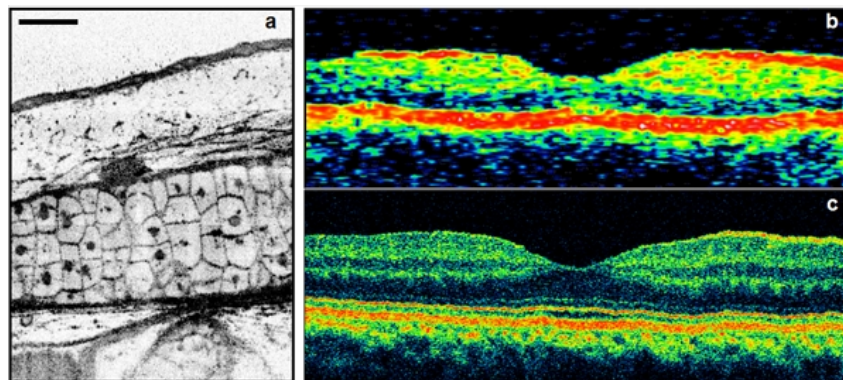


Figure 3.5: In vivo sub-cellular resolution OCT (a) (in a African tadpole). Standard resolution OCT (second generation OCT) (b) versus ultrahigh resolution ophthalmic OCT (c) of the living human retina. (from: [40])

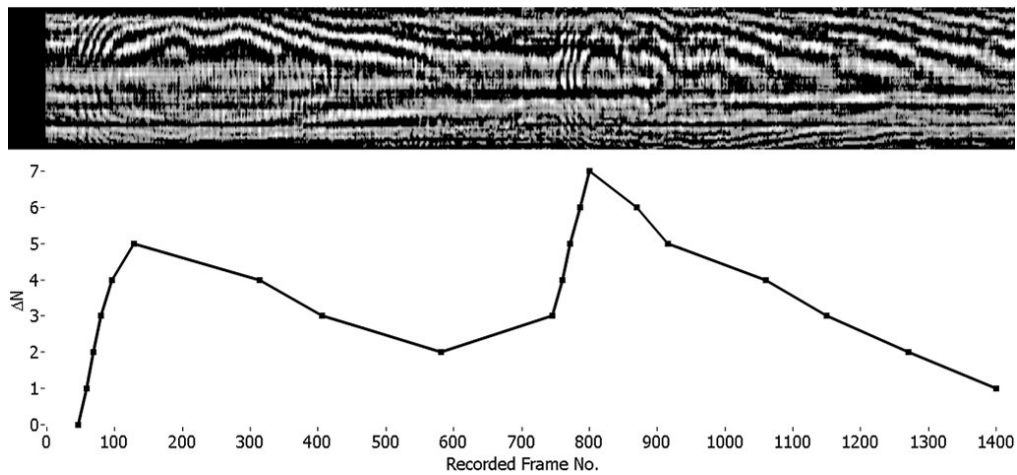


Figure 3.6: Synthetic interferogram recorded *in vivo* over two pulse periods, and the corresponding contraction-dilatation graph, i.e. the change of interference order (calculated by counting the fringes moving inward and outward) as function of time)[30].

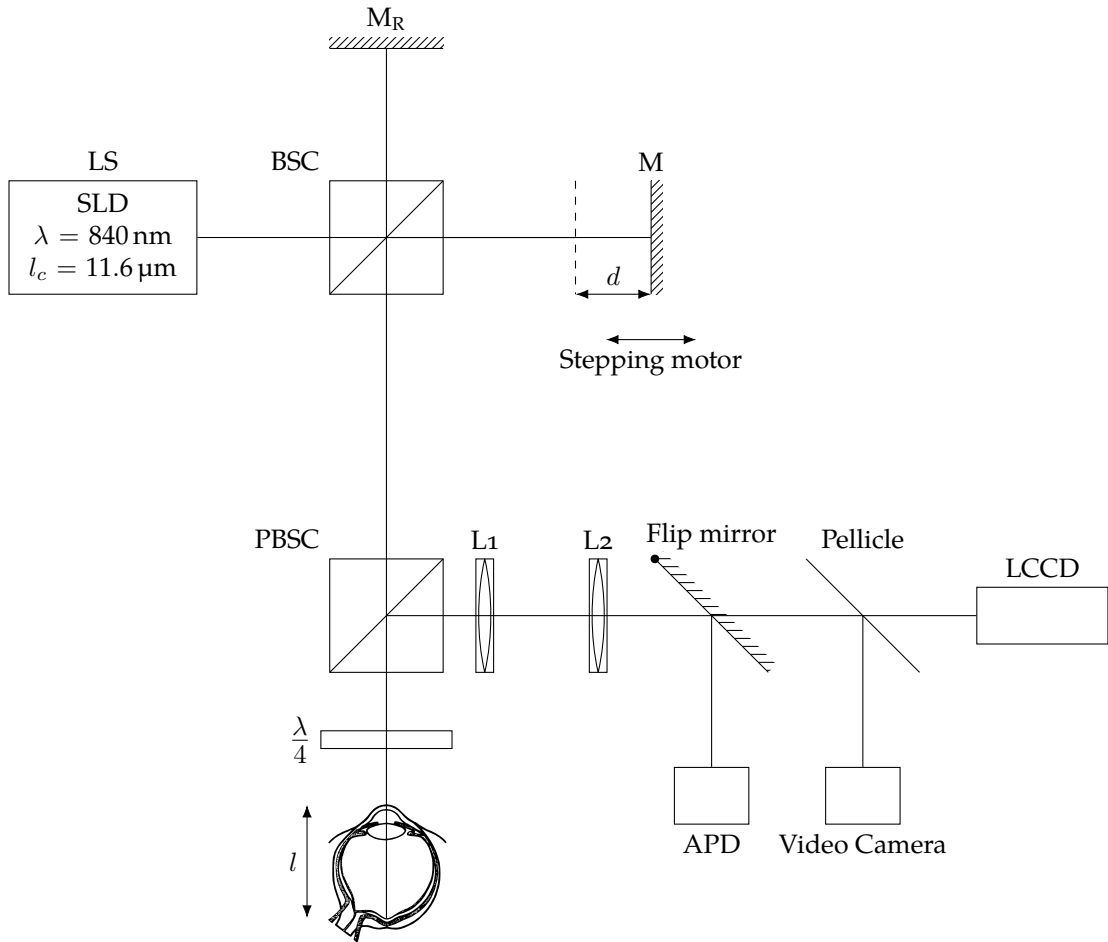


Figure 3.7: Schematic diagram of an LCTI system.

LS: light source; SLD: superluminescent diode; λ : central wavelength of the light source; l_c : coherence length of the light source; BSC: beam splitter cube; M_R : reference mirror; M: measurement mirror; PBSC: polarizing beam splitter cube; QWP: quarter wave plate; L1 and L2: lenses; APD: avalanche photodiode; LCCD: linear CCD array; l : intraocular distance to be measured.

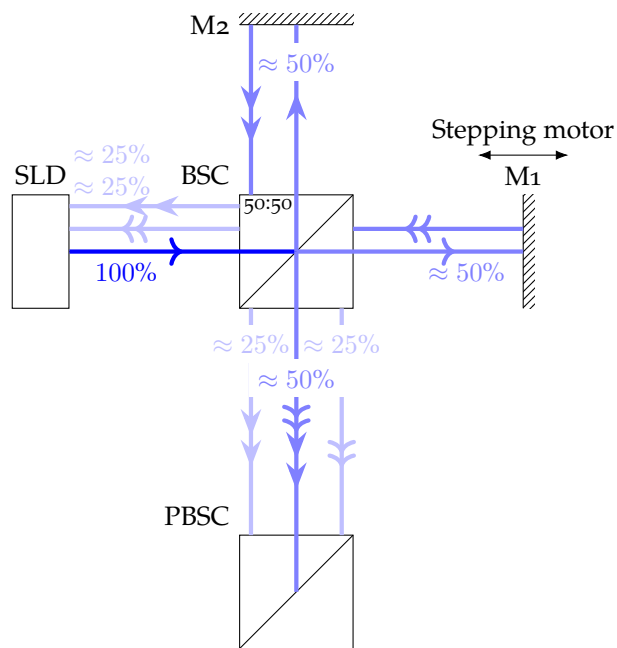


Figure 3.8: Losses on the non-polarizing beam splitter cube of the Michelson interferometer.
 SLD: superluminescent diode; BSC: beam splitter cube; M2: reference mirror; M1: measurement mirror; PBSC: polarizing beam splitter cube.

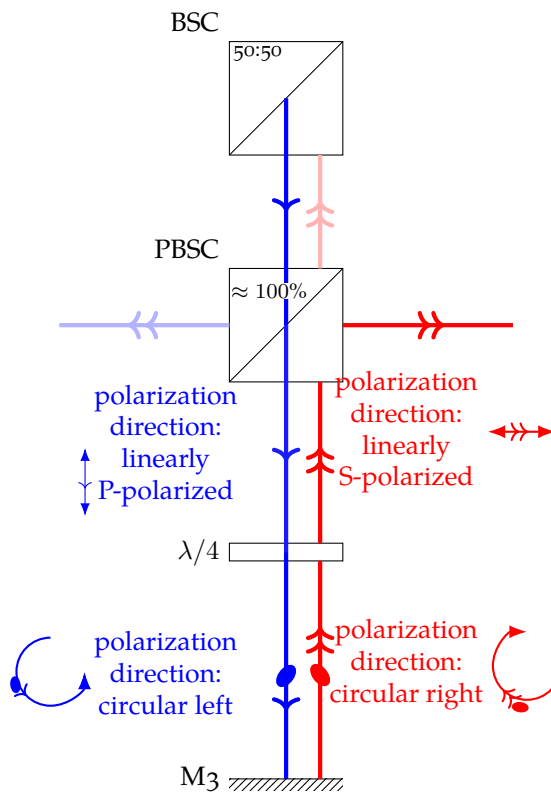
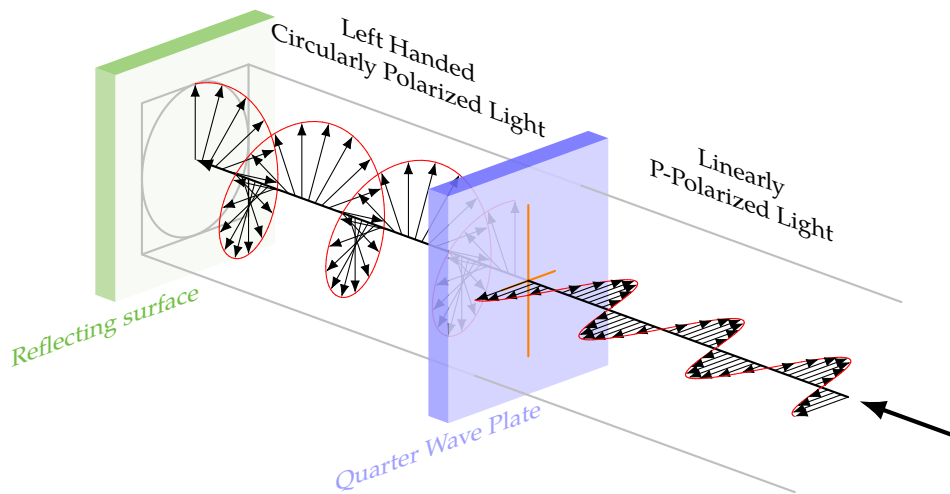
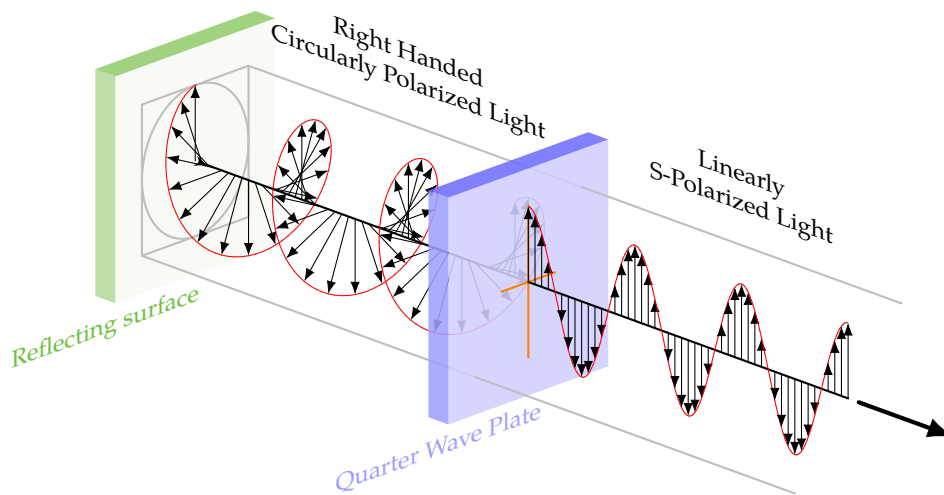


Figure 3.9: Operational principle of the polarizing beam splitter cube (PBSC). BSC: beam splitter cube; PBSC: polarizing beam splitter cube; QWP: quarter wave plate; M₃ represents the reflecting surfaces in the eye. For more explanation read section 3.12.1.



(a) P-polarized light is transmitted through the PBSC, illuminates the eye ...



(b) ...and is reflected from the various sites.

Figure 3.10: Effect of the QWP to the polarization state of the beam. Since the beam passes the quarter wave plate twice, it reaches the polarizing beam splitter the second time as S-polarized light. (Figure is created based on the code from <http://tex.stackexchange.com/questions/113900/draw-polarized-light/114029#114029>, accessed on 2016-01-08.)

3.12.2 Measurement Process

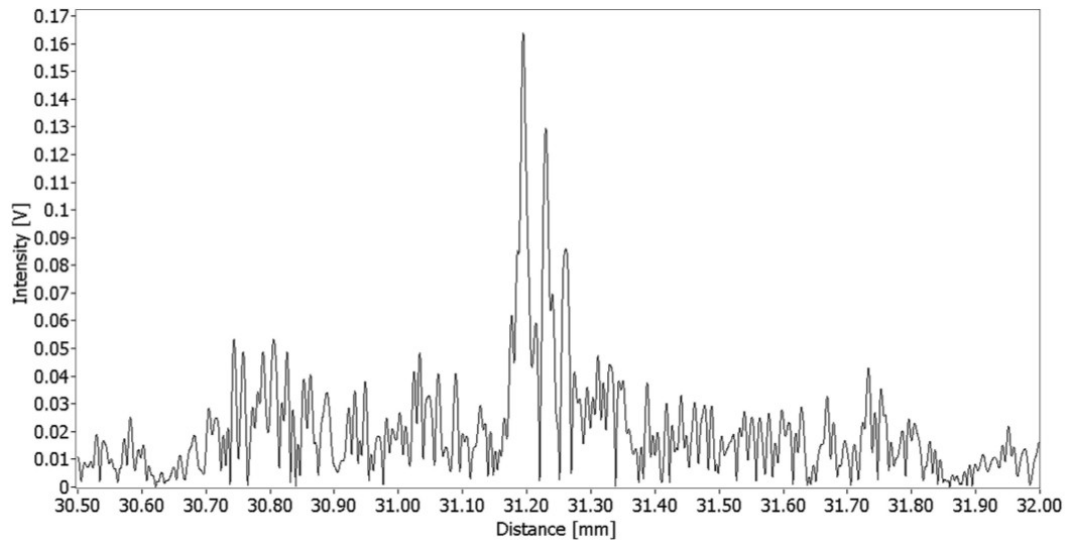


Figure 3.11: A-scan of a human volunteer (from [30]).

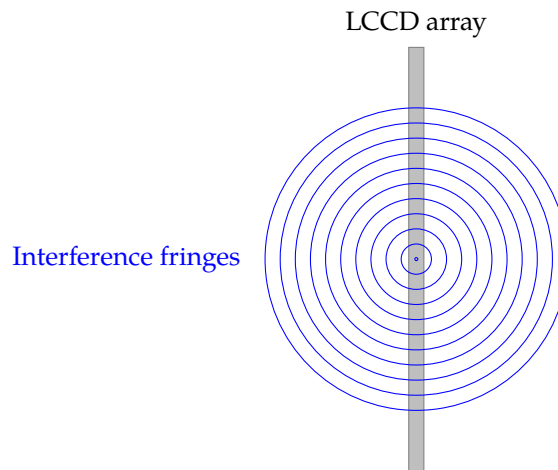
The first step of the measurement process is an axial eye length measurement which is based on dual-beam PCI (see Figure 3.3). In the measurement arm, the measurement mirror mounted on a stepping motor scans through a depth range, resulting in an A-scan (see Figure 3.11).

As long as the optical path length difference d in the interferometer does not differ from the optical path length difference l between the two ocular surfaces in the eye to a larger extent than the coherence length l_c of the light source (i.e., $|d - l| < l_c$), an interference can be observed, resulting in a peak in the A-scan. I.e. each peak on the optical A-scan corresponds to a reflective intraocular layer.

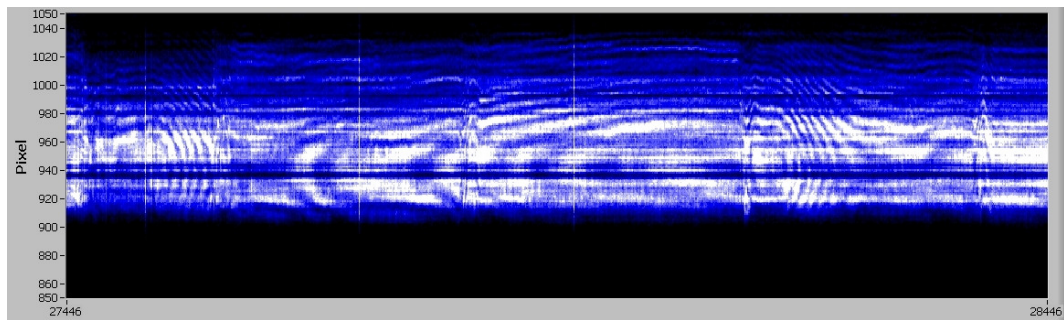
By positioning the stepping motor and hence the measurement mirror, any arbitrary intraocular layer can be selected for the second part of the measurement: the plane $\approx 30\text{--}40$ mm in front of the eye is imaged onto the linear CCD array (LCCD) array (see Figure 3.12a).

Since the relative movement caused by the cardiac cycle between the intraocular layers and the cornea is smaller than the coherence length, an interference pattern can be observed and recorded with the time, resulting in a so called synthetic interferogram (see Figure 3.12b).

LCTI allows measurement of time-resolved distance changes between the anterior surface of the cornea and preselected retinal layers. Figure 3.7 shows the optical setup of the LCTI system.



(a) The interference pattern resulting from the superposition of the reflections from the cornea and the intraocular layers is imaged onto the LCCD camera and recorded with the time ...



(b) ...resulting in a so called synthetic interferogram. The Y-axis shows the various pixels of the LCCD array, while the X-axis represents the time.

Figure 3.12: Interference pattern is recorded with the time.

Chapter 4

Optical Setup

In this chapter the old setup built up by Dragostinoff is presented followed by the necessary calculations for adapting the system to the rat eye.

4.1 Optical Setup of the Old System

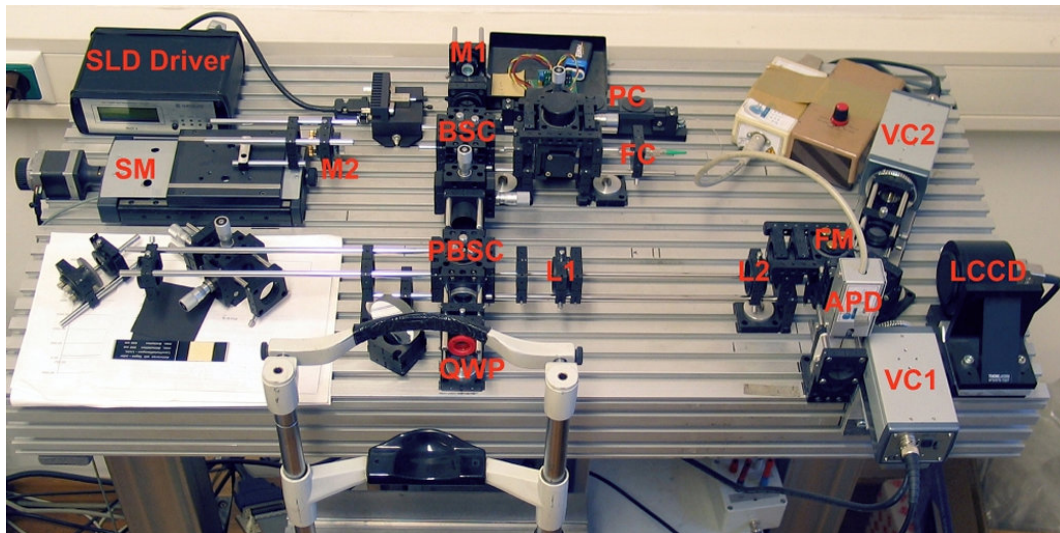


Figure 4.1: LCTI system built by Dragostinoff for human measurements [30].

SM: stepping motor; M1 and M2: mirrors; BSC: beam splitter cube; PC¹: polarization controller; FC: fiber collimator; PBSC: polarizing beam splitter cube; QWP: quarter wave plate; L1 and L2: lenses; FM: flip mirror; APD: avalanche photodiode; VC1 and VC2: video cameras; LCCD: linear CCD array.

The LCTI system built up by Dragostinoff is shown on Figure 4.1 [30].

The light source is a SLD (from Superlum, Russia) with $\lambda_0 = 840$ nm central wavelength, $\Delta\lambda_0 = 26.8$ nm FWHM bandwidth. The corresponding round-trip coherence length (from Equation 3.39) is $l_c = 11.6$ μm .

A fiber collimator with a focal length of 6.2 mm from OZ Optics (HPUCO-23-850-S-6.2AS, see Appendix A.3) was used together with the optical fiber SM800-5.6-125 from Thorlabs (see Appendix A.4). The calculated beam diameter values 0.98 mm [30].

A polarisation independent optical isolator (IO-F-850APC, Thorlabs, see Appendix A.5) was used to prevent light reflected back to the SLD.

The 3-paddle polarisation controller FPC030 from Thorlabs (see Appendix A.6) was used to minimise the losses on the PBSC.

During the scanning process, the stepping motor (SM) is moving the mirror with a constant velocity $v = 2.88$ mm/s, resulting in a Doppler shift of $\Delta f = 6857$ Hz [30]. M1 and M2 are mirrors from Thorlabs¹. The beam splitter cube (BSC) (see Appendix A.7) is a non-polarising beam splitter cube with a 50:50 (R:T) nominal split ratio.

The PBSC from Thorlabs² transmits P-polarised light $T_P > 90\%$ while reflecting S-polarised light $R_S > 99.5\%$.

The QWP converts linearly polarized light into circularly polarized light and vice versa (see Figure 3.10).

L1 and L2 are lenses with $f_1 = 30$ mm and $f_2 = 80$ mm, respectively.

The flip mirror, built in between the avalanche photodiode (APD) module and the LCCD realizes a manual optical router: in one position, the beam is directed toward the APD module, while in the other position it is directed onto the LCCD.

The beam during the axial eye length measurement was guided onto a APD module (with help of VC2). The APD is a semiconductor-based photodetector (photodiode). Carriers (electrons and holes) excited by absorbed photons are strongly accelerated in the strong internal electric field, so that they can generate secondary carriers, as it also occurs in photomultipliers. The avalanche process, which may take place over a distance of only a few micrometers, for example, effectively amplifies the photocurrent by a significant factor.

During the observation of the fundus pulsation, the flip-mirror is switched, and the beam is is guided onto the CCD line-camera (Sony ILX551, 2048 pixels, 14×14 μm pixel size, 8 bit resolution, see Appendix A.2). Due the pellicle (8R/92T), a small portion of the beam is led onto a video camera (VC1). The signal of the linear CCD

¹<https://www.thorlabs.com/thorproduct.cfm?partnumber=BB1-E03>, accessed on 2017-02-02.

²<https://www.thorlabs.com/thorproduct.cfm?partnumber=PB202>, accessed on: 2017-02-06.

array is recorded at a line readout rate of 600 Hz, parallel to that, the interference fringes are observable on the video monitor.

4.2 Adaptations to the Rat Eye

In this section, the mathematical formulas necessary for the adaptation of the system to the rat eye are presented. The distance between the cornea and the plane with the optimal contrast is estimated and the results of the calculations are shown.

4.2.1 Equation System

The following equations are used to determine the position of the lenses in the setup:

$$\begin{aligned}\frac{1}{f_1} &= \frac{1}{i_1} + \frac{1}{o_1} \\ \frac{1}{f_2} &= \frac{1}{i_2} + \frac{1}{o_2} \\ M &= \frac{i_1 i_2}{o_1 o_2} \\ D_{tot} &= i_1 + i_2 + o_1 + o_2\end{aligned}\tag{4.1}$$

Where f_1 and f_2 are the focal lengths, i_1 and i_2 are the image distances, o_1 and o_2 are the object distances respectively; M is the overall magnification and D_{tot} is the total distance.

Solving the equation system one can determine the exact position of the lenses.

4.2.2 Fringe Contrast

In this section the distance of the plane with the optimal contrast from the cornea is estimated. This distance is necessary to solve the equation system 4.1, because this is the plane that has to be imaged onto the LCCD camera.

Distance from the Cornea

For calculation of the fringe contrast, the procedure described in [30, pp. 55] was followed.

The wave reflected at the anterior corneal surface was assumed to be spherical, and the wave reflected at the retina and refracted by the lens and the cornea to be plane. For the following calculation, the distance from the cornea was called d_z (where z is the optical axis) with $d_z = 0$ at the front surface of the cornea, and the distances from the optical axis in x and y directions were called d_x and d_y , respectively. Since both waves can be assumed to be linearly polarized in the same direction, the intensity I is proportional to:

$$I(d_x, d_y, d_z) \propto \left| A e^{ikd_z} + \frac{c_c}{r} B e^{ikr} \right|^2, \quad (4.2)$$

with

$$r(d_x, d_y, d_z) = \sqrt{d_x^2 + d_y^2 + (d_z^2 + c_c)}, \quad \text{and} \quad k(\lambda) = \frac{2\pi}{\lambda}, \quad (4.3)$$

where c_c is the radius of corneal curvature (in m), A and B are reflection coefficients of the retina and the cornea, respectively, and $\lambda = 840 \times 10^{-9}$ m. For computation of contrast at a certain position d_z , the intensity was calculated at positions of d_x starting from -1 – 1 mm in steps of 10^{-3} mm, and the extremes I_{min} and I_{max} were determined. The contrast C was then calculated by:

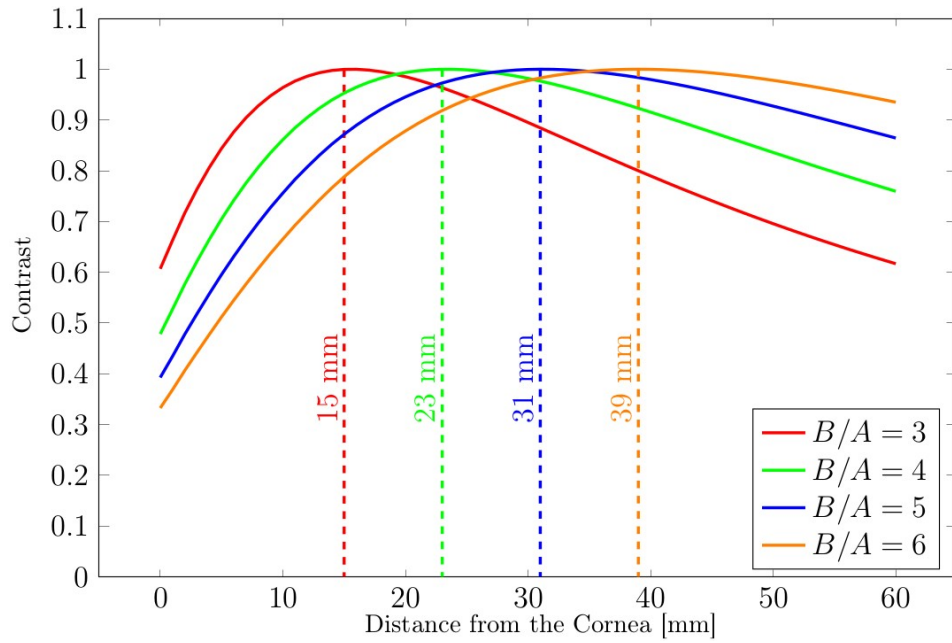
$$C = \frac{I_{max} - I_{min}}{I_{max} + I_{min}} \quad (4.4)$$

In order to make a comparison of the fringe contrasts in case of the rat and human eyes, the reduced schematic rat eye (rSRE) model described in [29] and the Gullstrand's human schematic eye model [44] were used (see Table 2.3 on page 18).

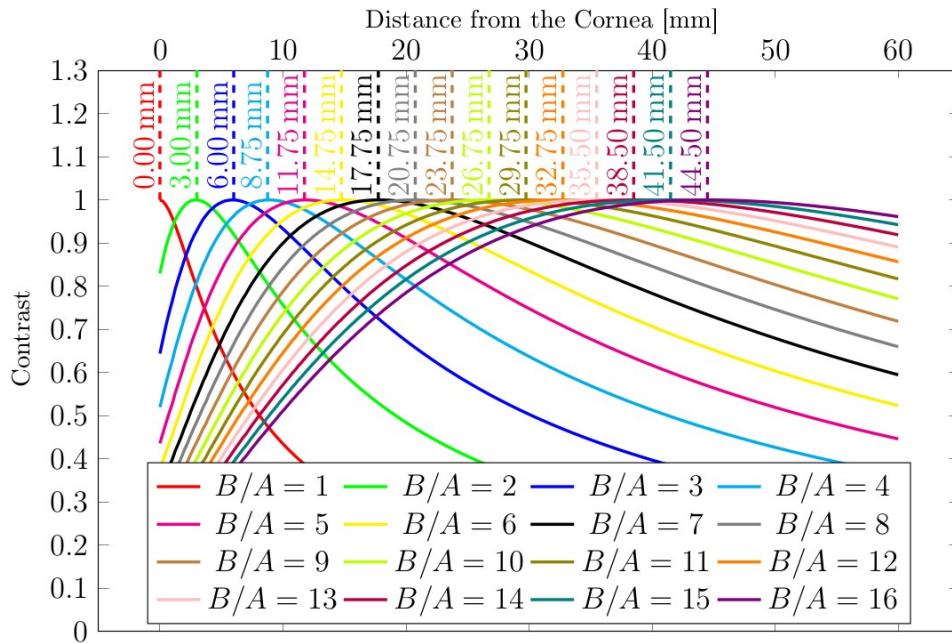
In Figure 4.2, the contrast (Equation 4.4) is plotted against the axial distance from the cornea (d_z values from 0–60 mm). The figure shows different curves for different B/A values.

In case of the human eye (see Figure 4.2a), the contrast maxima occurred at 15 mm ($B/A = 3$), 23 mm ($B/A = 4$), 31 mm ($B/A = 5$) and 39 mm ($B/A = 6$). Experimental results show the maximum contrast between 30 and 40 mm in front of the eye [43].

For the rat eye (see Figure 4.2b), the contrast maxima occurred at 26.8 mm ($B/A = 10$), 29.8 mm ($B/A = 11$), 32.8 mm ($B/A = 12$), 35.5 mm ($B/A = 13$), 38.5 mm ($B/A = 14$), 41.5 mm ($B/A = 15$) and 44.5 mm ($B/A = 16$).



(a) Gullstrand's Human Schematic Eye Model



(b) Reduced Schematic Rat Eye Model (sRE): $c_c = 3$ mm

Figure 4.2: Contrast of the fringe system plotted against the distance from the front surface of the cornea and for values of B/A from 3–6 for the human eye and from 1–16 for the rat eye. A and B , reflection coefficients of the retina and the cornea, respectively.

B/A Calculation

$$r_{reflect} = \frac{n_1 - n_2}{n_1 + n_2}, \quad (4.5)$$

where n_1 and n_2 are the refractive indices of the first and second medium, respectively.

B/A Calculation for the Human Eye

In case of the human eye, the refractive index of the tear film values between 1.336 to 1.357 [30], the refractive index of the vitreous values 1.336 [30], while the refractive index of the retina values 1.400[30].

$$B_1 = \frac{1.000 - 1.336}{1.000 + 1.336} = -0.1437 \quad (\text{from air to tearfilm})$$

$$B_2 = \frac{1.000 - 1.357}{1.000 + 1.357} = -0.1513 \quad (\text{from air to tearfilm})$$

$$A = \frac{1.336 - 1.400}{1.336 + 1.400} = -0.02339 \quad (\text{from vitreous to retina})$$

$$B_1/A = 6.143$$

$$B_2/A = 6.469$$

B/A Calculation for the Rat Eye

In case of the rat eye, the refractive index of the contact lens values 1.450 (the value is specified by the manufacturing company, Cantor & Nissel Ltd), the refractive index of the vitreous values 1.337 [29], while the refractive index of the retina values from 1.369 to 1.385 [45].

$$B = \frac{1.000 - 1.450}{1.000 + 1.450} = -0.1835 \quad (\text{from air to contact lens})$$

$$A_1 = \frac{1.337 - 1.369}{1.337 + 1.369} = -0.01183 \quad (\text{from vitreous to retina})$$

$$A_2 = \frac{1.337 - 1.385}{1.337 + 1.385} = -0.01763 \quad (\text{from vitreous to retina})$$

$$B/A_1 = 15.52$$

$$B/A_2 = 10.41$$

The estimated distance between the cornea and the plane with the optimal contrast values between 26.8 mm and 44.5 mm.

4.2.3 Solutions of the Equation System 4.1

The plane with the optimal contrast (for more explanation see section 4.2.2 on page 48) lies approximately 26.8–44.5 mm in front of the eye; the plane 30 mm in front of the eye is chosen to be imaged onto the LCCD.

The overall magnification is chosen to be 0.5. The total distance (from the plane to be imaged to the LCCD array, i.e. the plane with the optimal contrast) values to 530 mm. Focal length $f_1 = 30$ mm and $f_2 = 50$ mm were chosen to solve the Equation system 4.1.

The solutions of the equation system with the given parameters can be seen in Table 4.1 and a graphical representation can be seen in Figure 4.3. The solution 2 can not be realized, because the two lenses should be placed between the PBSC and the flip mirror (FM).

Table 4.1: Solutions for: eye to plane: 3 cm; plane to pbsc: 13 cm (for a graphical representation see Figure 4.3)

$f_1 = 3$ cm $f_2 = 5$ cm $M = 0.5$ $D_{total} = 53$ cm	
Solution 1	Solution 2
$o_1 = 22.1$ cm	$o_1 = 4.1$ cm
$i_1 = 3.5$ cm	$i_1 = 11.1$ cm
$o_2 = 6.6$ cm	$o_2 = 31.9$ cm
$i_2 = 20.9$ cm	$i_2 = 5.9$ cm

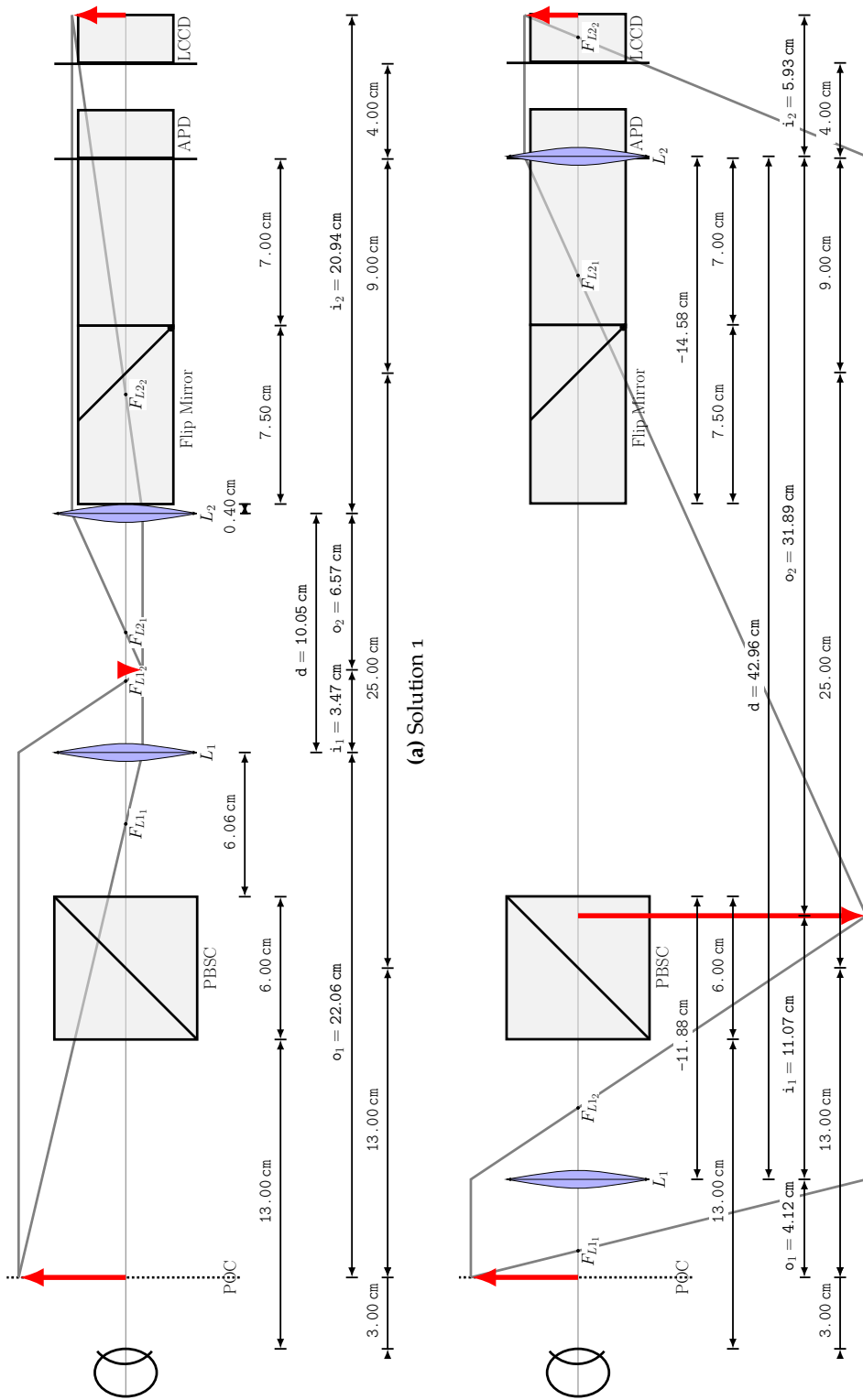


Figure 4-3: Solutions for: eye to plane: 3 cm; plane to pbsc: 13 cm (for the numerical values see Table 4.1)

4.3 Optical Setup of the New System

Figure 4.4 shows a picture of the new experimental setup, adapted to the rat eye.

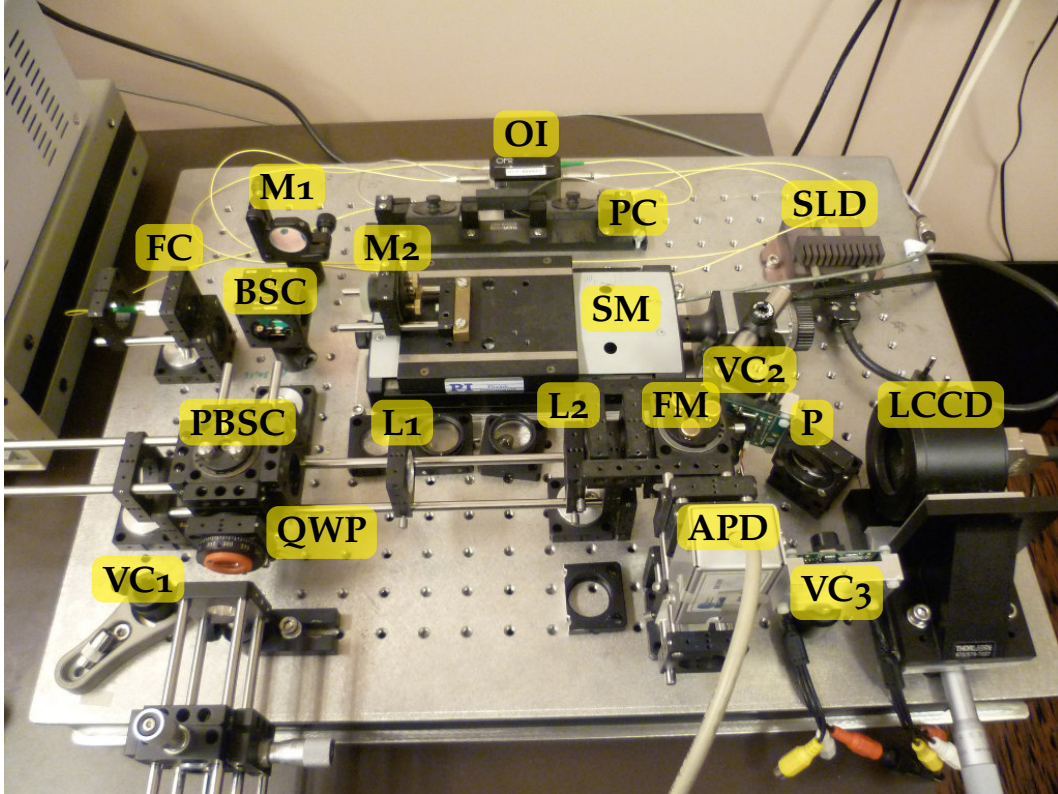


Figure 4.4: Experimental setup: the adapted system.

SLD: superluminescent diode; OI: optical isolator; PC¹: polarization controller; FC: fiber collimator; BSC: beam splitter cube; M1 and M2: mirrors; SM: stepping motor; PBSC: polarizing beam splitter cube; QWP: quarter wave plate; L1 and L2: lenses; FM: flip mirror; APD: avalanche photodiode; P: pellicle; LCCD: linear CCD array; VC1, VC2 and VC3: video cameras.

- The new, modified setup has smaller geometrical dimensions (60×45 cm), compared to the original one (approximately 100×40 cm).
- The lens L2 was changed to have focal length $f_2 = 50$ mm.
- The old big video cameras were changed to smaller ones from Conrad (the dimension with suspension: $55 \times 38 \times 45$ mm) (see Figure 4.5).
- The BSC and M1 were replaced by smaller ones from Thorlabs.



Figure 4.5: The new small CCD cameras from Conrad.

- Since fixation light is not required for the animal experiments, that is not part of the new setup; the headrest for human experiments was also replaced by an adjustable holder specially designed for OCT measurements in rats, by Thomas Blaschke (see Figure 4.6).
- Otherwise, technical components and parameters are the same as in the old setup.

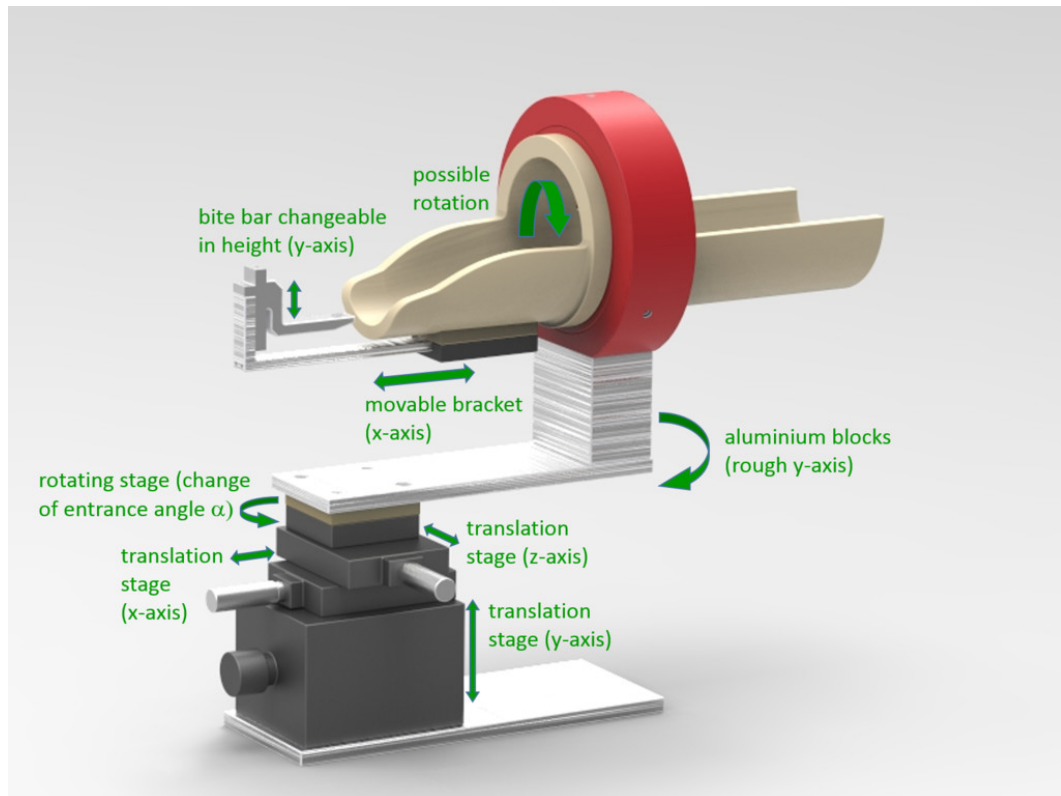


Figure 4.6: Adjustable holder for Optical Coherence Tomography eye measurements in rats. Picture taken from [46].

Chapter 5

Hardware and Software

Since Dragostinoff presented his LCTI system in 2010, a lot has changed in the field of information technology: not only the computing performance has multiplied, but also the softwares used back then are outdated today. In this chapter the arised issues connected to the information technology developments of the past years are described together with the applied solution.

5.1 Incompatibility Issues

As described in the previous chapter, most of the optical components of the setup of Dragostinoff was reused for the system built up for using with rats. It was an intended consideration to keep thrift in mind and to reuse as many parts of the old setup as possible. Aside from this, some hardware components could not be reused . This change in the hardware implied the need for changing the corresponding software, too.

The old personal computer (PC²) used for data acquisition and post processing was no more available and if it were, it has long been outdated. Therefore a new one had to be bought for this purpose.

The number of possible mainboards was limited by the requirement to have enough conventional Peripheral Component Interconnect (PCI) slots to enable the use of the already available data acquisition card (DAC), as well as the expansion card of the LCCD camera. The specifications of the new PC² are shown in Table 5.1.

The next step was to choose an appropriate operating system (OS): the old one, Microsoft Windows XP (XP) was no more an option (as of April 8, 2014 the extended support of it has ended). Before the choice of an appropriate OS, one has to keep in mind the complexity of the software developed for the LCTI system: all the software needed for data acquisition as well as for data evaluation was written in Laboratory Virtual Instrument Engineering Workbench (LabVIEW)¹. Although LabVIEW is

¹LabVIEW is a system-design platform and development environment for a visual programming language from National Instruments. (Source: <https://en.wikipedia.org/wiki/LabVIEW>, accessed on 25.06.2016)

available on a variety of platforms (including Microsoft Windows, various versions of UNIX, Linux, and OS X); the institution this masterthesis was carried out, has licence to the Windows version of LabVIEW. Additionally, the LCCD camera driver is only available for Windows. At the time the computer was bought, Windows 7 was a mature and stabil release, so the 64-bit version of this OS was choosen as the new operating system (Windows 7 Enterprise 64-bit Service Pack 1 (6.1, Build 7601)).

Not only the PC² and the OS were outdated, but also the used development environment: the LabVIEW version. To migrate an existing and functioning system to a new environment is always risky, but after carefully deliberation it was decided to do so: from LabVIEW 2009 (32-bit) to LabVIEW 2013 (Version 13.0f2, 32-bit).

Unfortunately, the LCCD camera driver and the old PCI card were not compatible with Windows 7. A new PCI card had to be ordered, but unfortunately the delivered driver, was not compatible with the old data acquisition (DAQ)-application developed in LabVIEW. It was necessary to make some fundamental changes in the LabVIEW code (see Section 5.4.3 and Appendix B).

5.2 Hardware

In this section the main and for the measurement most important not optical hardware components are presented: the PC² and for the data acquisition required expansion cards.

5.2.1 PC

Table 5.1 shows the main characteristica of the used computer.

Table 5.1: Technical specifications of the new computer.

Component	Product
Mainboard	ASRock Z97 Extreme 3
CPU	Intel S1150 Core i7-4790 @ 3.6 GHz Quad Core CPU
GPU	Sapphire Radeon HD 6570 1GB DDR3
Memory	16 GB DDR3 Corsair Vengeance low
HDD	Western Digital Caviar Green 2 TB
SSD	Crucial MX100 256 GB SSD

5.2.2 Data Acquisition and Stepping Motor Controller

NI-DAQ PCI card

The electronically filtered APD signal is read out with the data acquisition card PCI-6034E from National Instruments (see Figure 5.1). For datasheet see Appendix A.1 on page 100.



Figure 5.1: Data acquisition card PCI-6034E from National Instruments. Picture taken from National Instruments' webpage².

Strasing PCI Card

Due to incompatibility issues between the old LCCD PCI card (see Figure 5.2a) and the new operating system (see Section 5.1), a new one (see Figure 5.2b) has been ordered and is used. Table 5.2 shows the main differences between the two cards.

The manual delivered with the new PCI card and the driver states:

“The EEPROM on the PCI-board has the following mark:
Standard version (with FIFO): $Xn, n = 3$ if Windows 7 compatible
FIFO-version with interrupt: XnI .”

Since the new board has $X3$ as marking, it is the standard version, i.e. with FIFO, and is compatible with Windows 7. See Appendix A.2 on page 101 for the manual.

²<http://sine.ni.com/nips/cds/view/p/lang/en/nid/11916>, accessed on 06.08.2016

Table 5.2: Differences between the old and the new LCCD PCI cards

	Old	New
Manufacturer	Stresing Ing. Büro	Stresing Ing. Büro
Model number	2105-2	2150-2
Windows 7 compatible	no	yes ³
Driver version	V1.36	V4 ⁴
FIFO-version	no	yes
Manual version	1.5/2003	2.4/2014

5.3 Software

In this section the used softwares are described, including the operating system, the LabVIEW development environment and the necessary drivers for the PCI expansion cards.

5.3.1 Operating System and Development Environment

All the measurements and evaluation of the OFP data were performed on a PC with Windows 7 Enterprise 64-bit Service Pack 1 (6.1, Build 7601), running LabVIEW 2013 (Version 13.0f2, 32-bit).

5.3.2 NI-DAQ Driver

The Windows driver for the extension card PCI-6034E can be downloaded from the National Instruments' webpage: <http://www.ni.com/download/ni-daqmx-base-3.7/4281/en/>, accessed on 11.06.2016.

³For Windows 7 and Windows 8, 32-bit and 64-bit drivers are available, but they are not certified.

⁴Information from the README file of the delivered driver:

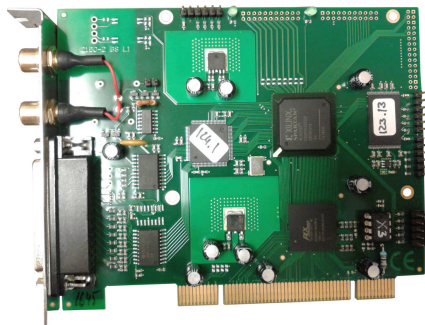
Because the 64-bit driver is not certified, it can only be installed if Windows 7 is in test mode. More about Windows test mode can be found here: <http://www.thewindowsclub.com/what-is-test-mode-and-how-to-remove-test-mode-watermark-in-windows-7>.

Before installing the driver, run the delivered batch file `Testsigning_Run_as_admin.bat`.

As a consequence of the above mentioned not certified driver, the camera can only be used in test-mode.



(a) Old extension card.



(b) New extension card.

Figure 5.2: Old and new PCI cards from Stresing Ing. Büro (Berlin, Germany).

5.3.3 Stressing PCI Driver

Because the new board comes with a FIFO memory, and the old one wasn't supplied with it, there are fundamental changes in the driver. A new dll and new subVIs are delivered with the driver, the old ones are not compatible with this board.

5.4 Data Acquisition and Signal Processing

This section describes the signal processing methods performed on the APD signal, as well as the recorded synthetic interferogram. The LabVIEW applications are shortly presented, together with the description of necessary modifications in the code. These modifications are needed due to the new hardware components and the new software versions (OS, LabVIEW). Because this would be out of the scope of this thesis, the existing LabVIEW code had not been complemented with a detailed documentation but only with short hints for superficial understanding which part is what responsible for.

5.4.1 Filtering and Image Enhancement

The signal from the APD is filtered electronically by a bandpass filter with a central frequency matching the Doppler shift f_D [30, p. 40]. For readout of the signal, the DAC PCI-6034E from National Instruments was used. After data acquisition an additional filtering step is performed digitally in LabVIEW. After performing a fast Fourier Transform (FFT) on the acquired signal, the frequency range determined by the bandwidth of the light source and the Doppler shift is selected, followed by an inverse FFT (iFFT) [30, p. 43].

Once the animal was correctly positioned – so that the interference fringes could be observed on the video monitor – the signal was recorded with the LCCD array operated at a line readout rate of 600 Hz. For online inspection of the fundus pulsations in LabVIEW, a background subtraction for elimination of internal reflections and static interference patterns from the animal's eye was performed. The advantage of this method is the effective removal of static and almost static background signals at a relatively low computational effort, leading to no significant delay in online inspection [30, p. 41, p. 66].

5.4.2 Data Acquisition Software Developed in LabVIEW Environment

All the LabVIEW files needed for the measurements and data evaluation are listed in the Appendix B. Three applications were used, one for the axial eyelength measure-

ment (*Augenlaenge.vi*), one for the ocular fundus pulsation measurement (*Kamera.vi*) and one for the evaluation of OFP (*LadenProgrammLCTI.vi*).

The user interfaces (“Front panels”) for AEL measurement (*Augenlaenge.vi*) and for OFP measurement (*Kamera.vi*), as well as that for the evaluation program (*LadenProgrammLCTI.vi*) can be seen in the Appendix B.1, B.4 and B.7, respectively.

5.4.3 Changes in the LabVIEW Code

Program for the AEL Measurement

filename.vi This is a new helper subVI to make file naming easier and consistent (see Figure B.3).

Augenlaenge.vi Additionally to the binary file outputs, also plain text files are saved to make LabVIEW and platform independent postprocessing possible (see Figure B.2). File naming was also unified by *filename.vi*.

Program for the LCCD Camera

The most important and fundamental changes in the code are caused due to the new PCI board from Stresing.

Since the old board hadn’t a FIFO memory and the new one has, reading out the LCCD camera had to be changed the LabVIEW. The old method with the noFIFO version read the camera with the function GETCCD in a loop. Since the time between 2 reads (2 calls of GETCCD) is the exposure time, a wait function was needed. This waiting had to be accomplished by software.

With the new FIFO version this is not needed anymore, because it has a built in hardware timer, which is programmed by registers of the PCI board. Here the data is written constant to the FIFO and the software must poll the FIFO before it overflows.

KameraInit.vi The initialisation process has three steps: driver initialisation, board initialisation and reset FIFO. This is done by *KameraInit.vi*, with help of the three VIs (*InitDrv.vi*, *InitBrd.vi* and *FFRS.vi*,) delivered with the new driver. Figure B.5 in the Appendix shows the modified block diagram.

Kamera.vi The old code had a software timer that was needed for the noFIFO version. This is no more required, because the built in hardware timer of the FIFO version. This hardware timer (and the camera) is started by the function StartTimer.vi (see Figure B.6a and Figure B.6b). Instead of the old method GETCCD.vi, two new functions (FFValid.vi and FFRead.vi) has to be used for the readout (see Figure B.6c). At the end, the hardware timer has to be stopped (FFStopTimer.vi) and memory has to be freed by Exit.vi (see Figure B.6d).

Program for the Evaluation of OFP Recordings

On LadenProgrammLCTI.vi no changes were made, because the output files produced by Augenlaenge.vi and Kamera.vi were also unchanged. Figure B.7 shows the LabVIEW front panel of the VI.

Chapter 6

Measurements and Results

Due to the lack of space in the animal lab and to the dense timetable of other experiments, the LCTI system was built up twice: first, in the optics lab, where some basic *in vitro* measurements were made to verify the system is working. After that, the electronical parts (e.g., power supplies, PC, etc.) were disconnected and the very sensitive components (e.g., the pellicle) has been removed and the whole system was carefully transferred to the animal lab, where it was built up and adjusted again. Following that, there was one day, and about 2 weeks later a timeframe of 4 days, when *in vivo* animal measurements could be done. After the five measurements (each day one measurement) the whole system was transferred again to the optics lab.

6.1 In Vitro Measurements

For testing purposes, *in vitro* measurements on different samples were performed: on a microscope slide and on an artificial eye, detailed below.

6.1.1 Results

Microscope Slide

First, a standard microscope slide (see Figure 6.1) was positioned in place of the animal's eye and an axial length measurement was performed. The resulting A-scan can be seen in Figure 6.2b. There occur two reflections: one at the front surface of the slide and one at the back surface. In the A-scan there is a peak at "0-position" and a peak at 1.4975 mm corresponding to the two reflections from the front and back surface of the glass plate. For an explanation of the peaks see Figure 6.2.

The refractive index of the glass is about $n = 1.5$ (depending on the exact material); the microscope slide has a thickness of about 1 mm; so the the optical path length according to Equation 3.41 is estimated about 1.5 mm, which is in good agreement with the measured value 1.4975 mm.

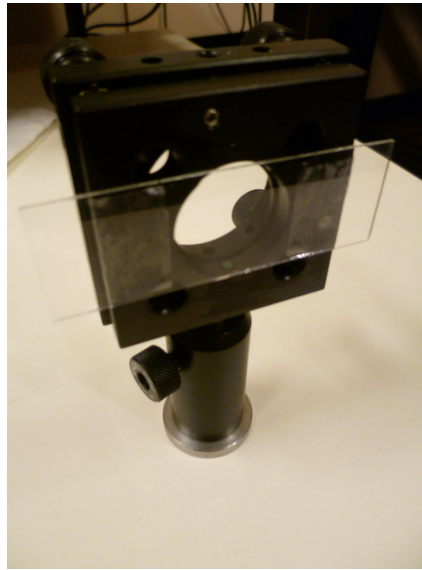


Figure 6.1: A standard microscope slide.

Artificial Eye

Secondly, an artificial eye (the front surface of the lens represents the front surface of the cornea and a piece of white paper represents the retina; see Figure 6.3) was measured. Measurements were performed placing the “retina” (i.e. the piece of paper) farther from the lens. The lens has a focal length of 6 mm, a radius of curvature of $r = 3.06$ mm and a refractive index of $n = 1.510$ at 840 nm [47]. One A-scan from these measurements is shown on Figure 6.4b: Peak 1, the zero peak, corresponds to the interferences of the reflections 1a – 2a, 1b – 2b and 1c – 2c (see Fig 6.4a). peak 2 is corresponding the interferences of the reflections 1a – 2b and 1b – 2a. These two peaks, i.e. peak 1 and peak 2 are not moving because these distances are fix, arising from the geometrical thickness of the used lens.

Two moving peaks arise from the variable distance of the mirror relating to the front and back surfaces of the lens; the third peak, peak 3 is corresponding to the interferences of the reflections 1b – 2c and 2b–1c; peak 4 corresponds to the interferences of the reflections 1a – 2c and 2a – 1c.

Other peaks may originate from multiple reflections and/or other reflections in the system itself.

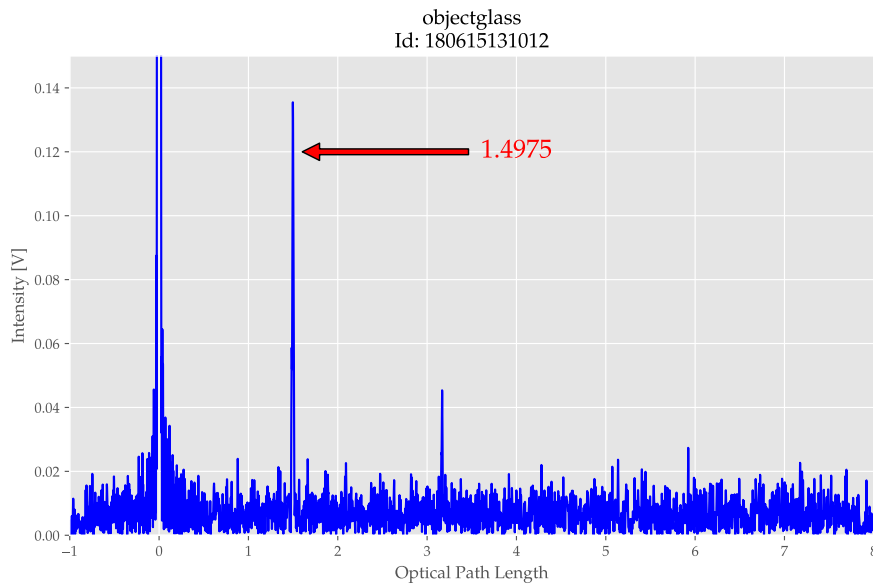
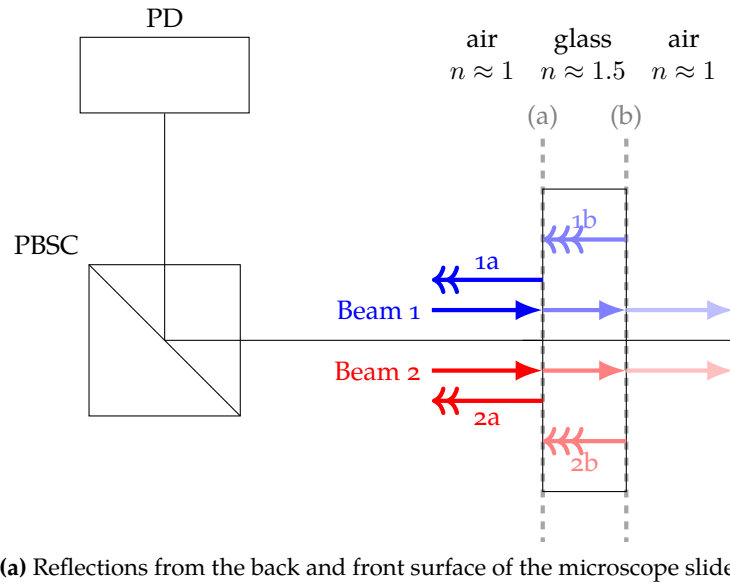


Figure 6.2: Resulting A-scan from a microscope slide: the zero peak corresponds to the interferences of the reflections $1a - 2a$ and $1b - 2b$. The peak at the position 1.4975 corresponds to the interferences of the reflections $1a - 2b$ and $1b - 2a$.

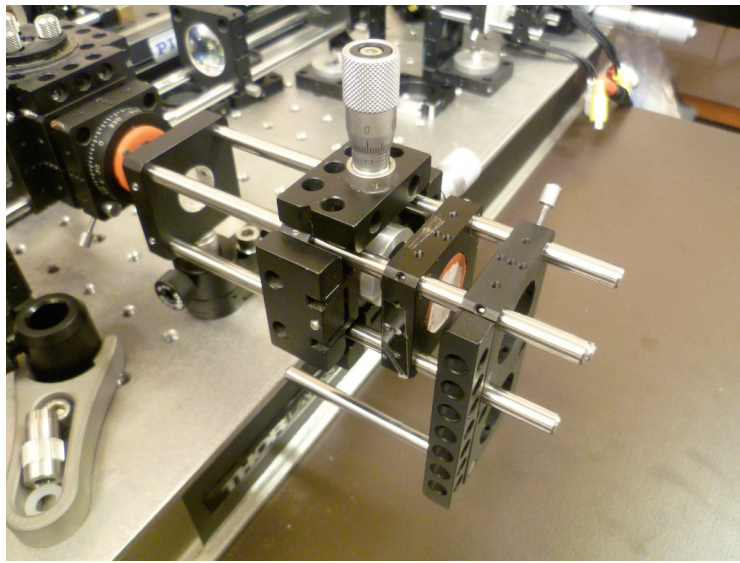
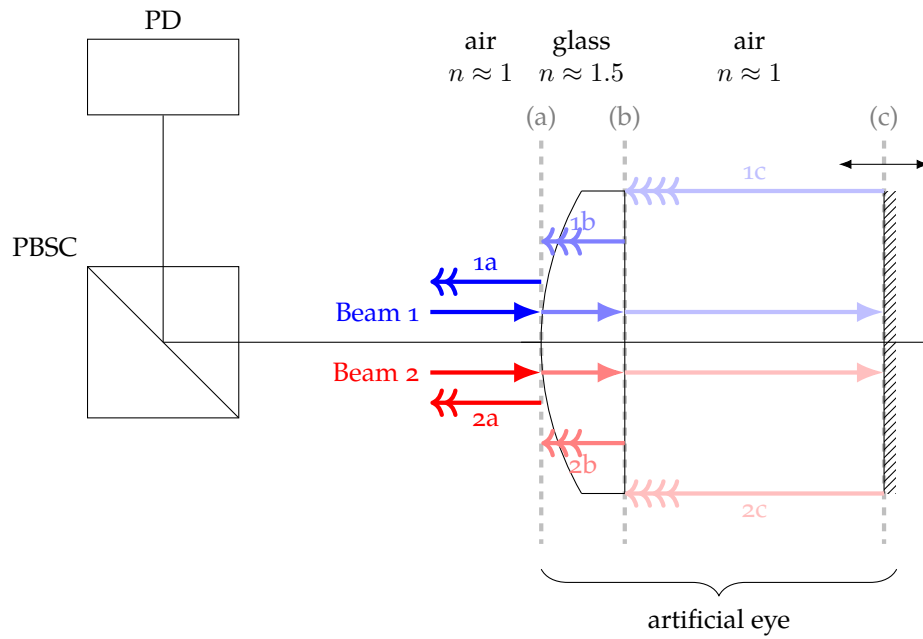
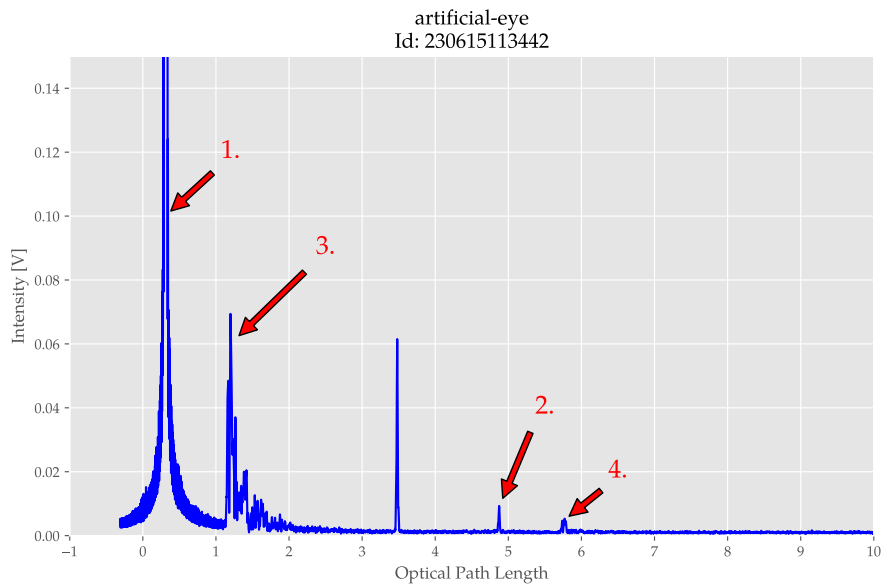


Figure 6.3: The artificial eye.



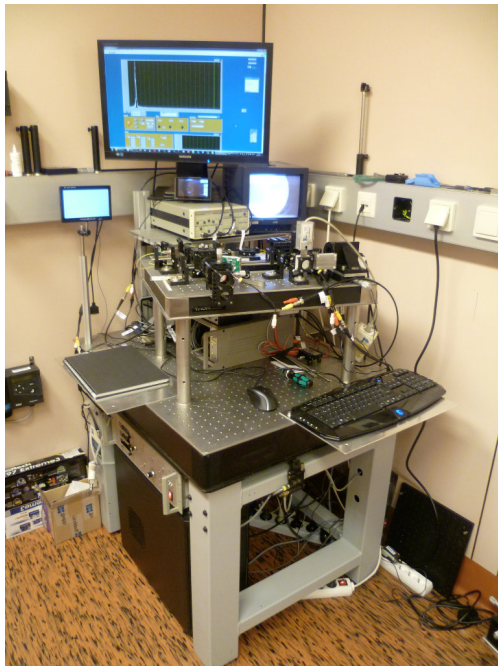
(a) Reflections from the artificial eye.



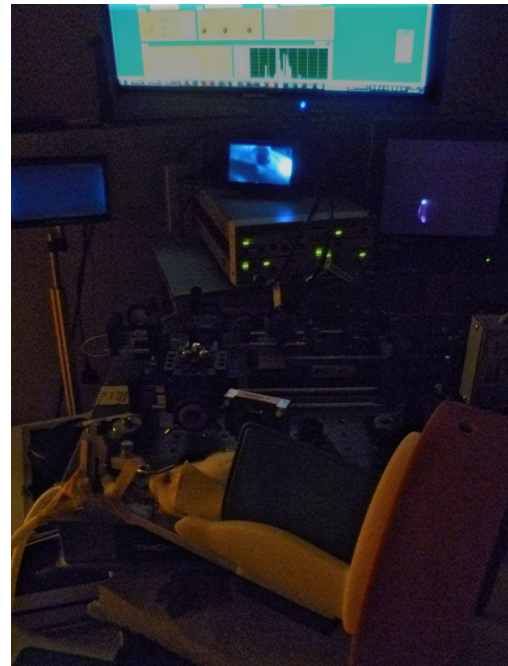
(b) A-scan of the artificial eye.

Figure 6.4: Resulting A-scan from the artificial eye. For more explanation see the text.

6.2 In Vivo Measurements



(a) Before and ...



(b) ... during measurement.

Figure 6.5: The experimental setup built up in the animal lab.

6.2.1 Laboratory Rats Used in the Study

The measurements were performed following the statement for the use of animals in ophthalmic and vision research of the association for research in vision and ophthalmology (ARVO) and was approved by the ethical committee for animal experiments of the Medical University of Vienna. 5 male Sprague-Dawley rats¹ with a body weight of 470 to 550 g were used in the study. Anesthesia was induced with an intraperitoneally injection of 100 mg/kg ketamine and 5 mg/kg xylazine. The rats were intubated and ventilated with O₂, air and 1.5 to 2 % isofluran to maintain deep anesthesia. 3 mg/kg piritramid were applied subcutaneously for analgesia. 1 ml of tempered 0.9 % NaCl was applied subcutaneously to ensure hydration of the animal during anesthesia. The right eye of each rodent was used for the measurements. To maintain good imaging qualities, the experimental eye was continuously moistened with 0.9 % NaCl. After the experiment the rats were euthanized via a lethal injection of 300 mg/kg pentobarbital.

¹The Sprague-Dawley rat is an outbred multipurpose breed of albino rat.

It is important to note, that all of the laboratory rats used in the study were experimentally investigated before the LCTI measurement, having a difficult to estimate effect on the vital status of the rats and such a way on the whole LCTI measurement.

In total, five animals were measured with the LCTI system. Below, in Section 6.2.3 on page 73 some characteristic results are shown, with evaluation and determination of the absolute position of the ocular layers with respect to the cornea front surface.

6.2.2 Remarks

Small Movements

During the measurements no stereotaxic head holder was used, with that a much more precise positioning and fixation of the animal would be possible. The animal was in anesthesia, but there were some movements present (e.g., pulmonary movement). The veterinarian continuously controlled the vitalic parameters (e.g., breathing, pulse, blood pressure, body temperature) and if necessary changed the amount of drugs applied. Unfortunately it was possible, that in some moments the animal was more "active" than in other moments, resulting in more movement artifacts. Despite the best efforts, it was possible, that a well positioned eye was moving during the measurement, or between the first and second part of the measurement.

Contact lens

To maintain a smooth ocular surface and to preserve the animal's eye during the measurement procedure, it was planned to apply a contact lens with zero optical power onto the cornea. The lens was manufactured (by Cantor & Nissel Ltd, UK) with a radius of curvature 3 mm, a diameter 6 mm and a refractive index 1.45.

Unfortunately, the radius of the lens was not appropriate for the eye's radius, therefore it could not be used for the measurements. As a consequence, the fringe contrast was a bit reduced in contrast to the calculated one (see Section 4.2.2); and the eye had to be moistened periodically with physiological saline during the whole measurement. The continuous drying of the rat's eye caused variations of image quality.

Moistening the eye need also some practice: sometimes a drop stays hanging on the eye. The excess needs to be removed, else it could be begin to move during measurement.

Heart Rate

The heart rate of the rats depends on various factors: breed, sex, age, bodyweight, bodytemperature, health, wakefulness (awake or in anesthesia), etc. Figure 6.6 shows the changes in heart rate of lightly anesthetized rats and deeply anesthetized rats hypothermia in an experiment with male, Sprague-Dawley rats, weighting between 300 and 375 grams [48]. One can see, that there are huge differences in heart rate (HR) depending on body temperature.

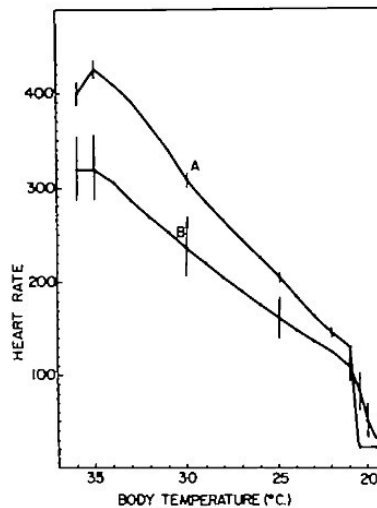


Figure 6.6: Changes in heart rate of lightly anesthetized rats, A, and deeply anesthetized rats, B, during hypothermia in an experiment with male, Sprague-Dawley rats, weighting between 300 and 375 grams. (From [48])

During the LCTI measurement, the experimental animal is placed on a thermo mat, which has two states: turned on and turned off. This enables the veterinarian to keep the rat body temperature in the “normal range”, but it does not give any information about the influence of temperature changes during measurement.

Without recorded data of HR, blood pressure and body temperature and with the fact, that there are no information about the resting HR of the animals, it is impossible to decide if the evaluated beat-to-beat intervals are correct: only extreme, non-vital values could be excluded.

Unintentional Movements Induced by the Operator

During measurement the operator needs manually switch the flip mirror, which is another source of error: an accidental touch on other parts or on the experimental

animal can cause the misalignment of the system self or the displacement of the eye.

Delay During Positioning Caused by the A/D Converter

It was quite difficult to place the animal so that the experimental eye will be in a good position: the incident light should go through the pupil and impinge onto the posterior pole of the eye and the reflections from the different ophthalmic layers should come back to the sensor. First, the reflected light was guided onto a camera, to show the interference on a (cathode ray tube (CRT)) monitor. The cause not to use a digital video converter and show the resulting image (see Figure 6.7) on the PC-monitor during the positioning, was the relative high delay between the movement and the resulting "effect" displayed. It was impossible to find the optimal position, but with the CRT monitor the delay was eliminated.



Figure 6.7: Similar image is shown on the monitor, if the experimental eye is in a good position.

The results of an LCTI measurement are OPL^2 s. To get the distances in millimeter, OPL^2 values have to be divided by the refractive index n of the medium through which light was propagating. Based on Figure 2.9b, on data in Table 2.3 and on data in Section 4.2.2 the following estimation was made for the overall refractive index of the rat eye: $n \approx 1.567$.

6.2.3 Representative Results

AEL measurement was carried out on all the animals, but unfortunately, OFP measurement could not be performed on all rats: one of the animals was no more living at the time it arrived for LCTI measurement. In this case only AEL measurement was performed.

Synthetic interferograms were recorded in several depths, but only interferograms from the most reflecting layer had the quality to be evaluated fully (i.e. determination of pulse periods, counting fringes and determination of time course and amplitude

of fundus pulsation). In other cases it was only possible to determine the pulse periods, or not even those. Nonetheless on these interferograms one can see “strange” repeating structures, but no fringes like on interferograms recorded from the most reflecting layer.

Recorded A-scans

Figure 6.8 shows a recorded A-scan of a rat (on top, the whole scan range can be seen, below the range with the retinal peaks is magnified).

During the whole measurement process, several A-scans (and also interferograms) were recorded. The A-scans differ always slightly from each other due to the fact, that motion could not be eliminated, but also drying eyes can cause differences between recordings.

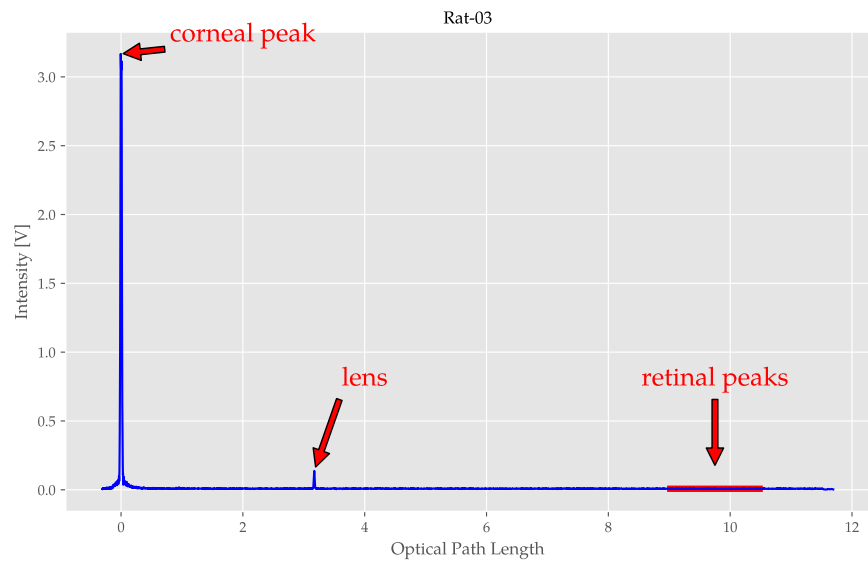
Determination of the Absolute Position of Different Ocular Layers

With help of the ultra high resolution OCT (UHR-OCT) recording (see Figure 6.9), the relative distances of different ocular layers were determined: the scale bar for 100 μm equals 140 pixels on the picture. Through measuring the distances in pixels between adjacent layers, these can be converted into micrometers (1 pixel = $5/7 \mu\text{m} \approx 0.714 \mu\text{m}$). The measurements were taken with the Measurement Tool² of GNU Image Manipulation Program (GIMP).

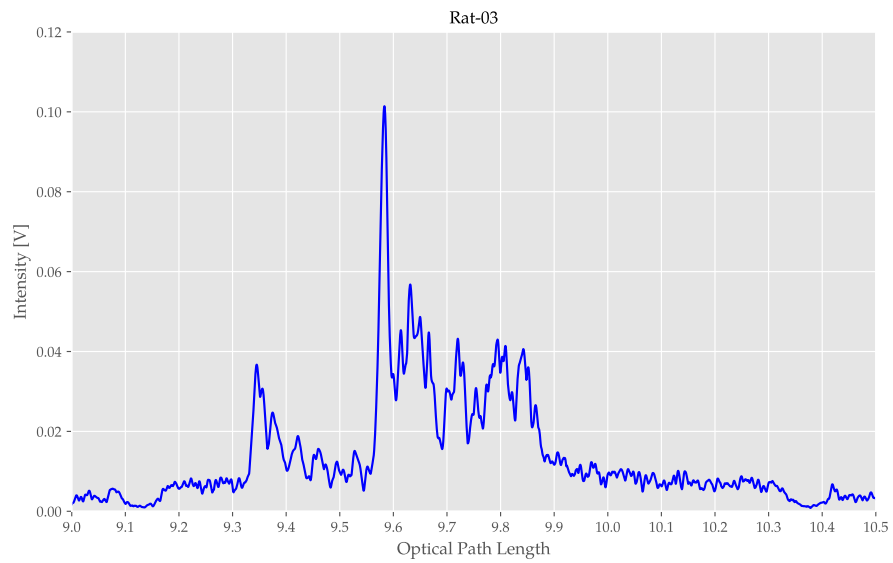
Figure 6.9 can be very helpful when different ocular layers are determined on the A-scan, because an OCT B-scan is composed of a series of adjacent A-scans recorded. The strongest reflecting layer on the A-scan (see Figure 6.8b and Figure 6.10) is most probably the RPE or Bruch’s membrane (BM). The first two peaks are most probably caused by light reflected at the ILM and NFL. Choroidal structures may be assigned with peaks 4, 5 and 6; while peaks 7, 8 and 9 could correspond to scleral structures.

From all animals similar A-scans were recorded with small variations in distance of layers, reflectivity and visibility of single layers.

²<https://docs.gimp.org/en/gimp-tool-measure.html>, accessed on 2017-02-06



(a) A-scan on the whole scan range show the relation of magnitudes of different reflecting surfaces in the eye. Retinal peaks can be seen only on the magnified figure.



(b) Magnified A-scan on the range of retinal peaks.

Figure 6.8: A-scan of a rat.

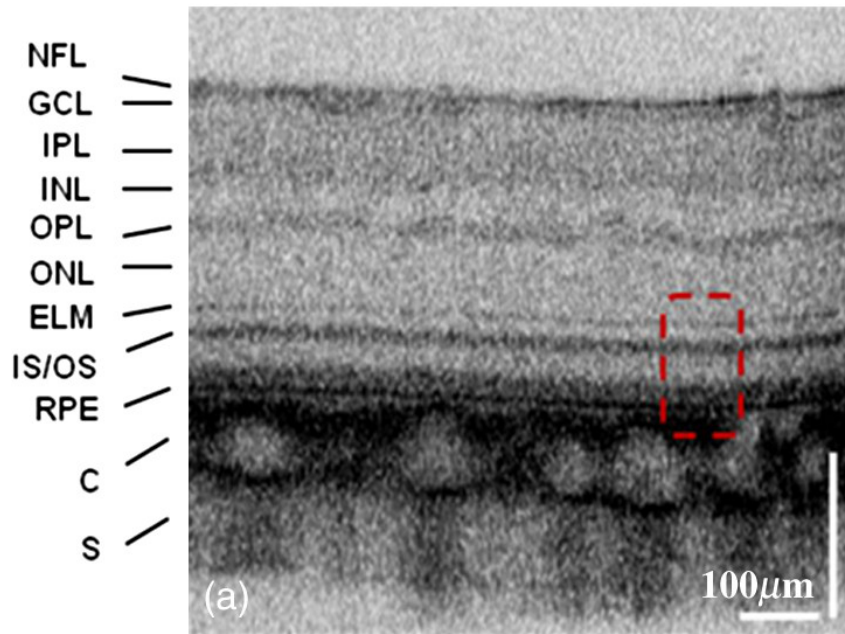


Figure 6.9: UHR-OCT tomogram acquired from a healthy rat retina. Picture taken from [49]. NFL: nerve fibre layer; GCL: ganglion cell layer; IPL: inner plexiform layer; INL: inner nuclear layer; OPL¹: outer plexiform layer; ONL: outer nuclear layer; ELM: external limiting membrane; IS/OS: interface between IS and OS (IS: photoreceptor inner segment; OS: photoreceptor outer segment); RPE: retinal pigment epithelium; C: choroid; S: sclera

Table 6.1: Distances between adjacent ocular layers in the rat eye, based on the UHR-OCT recording on Figure 6.9.

Adjacent ocular layers	pixels	μm
NFL — GCL	15	10.714
GCL — IPL	41	29.286
IPL — INL	32	22.857
INL — OPL	32	22.857
OPL — ONL	34	24.286
ONL — ELM	34	24.286
ELM — IS/OS	23	16.429
IS/OS — RPE	47	33.571
RPE — C	44	31.429
C — S	69	49.286

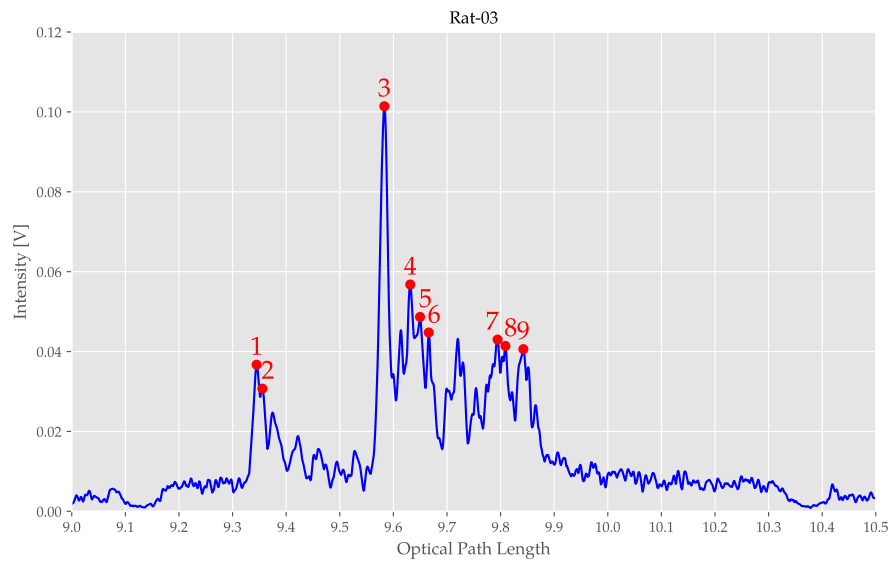
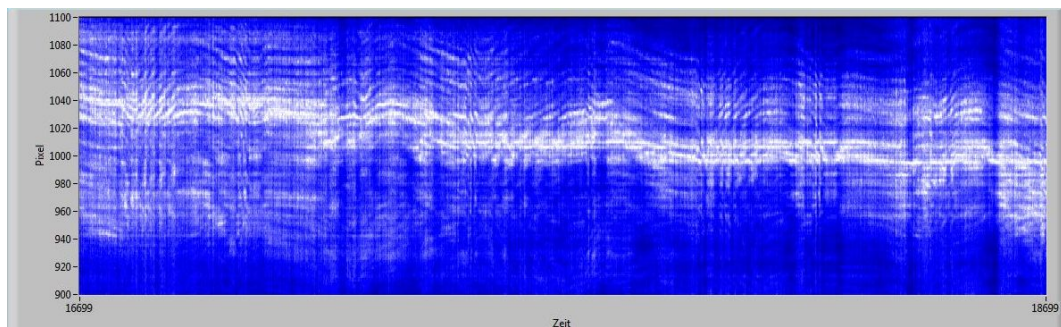


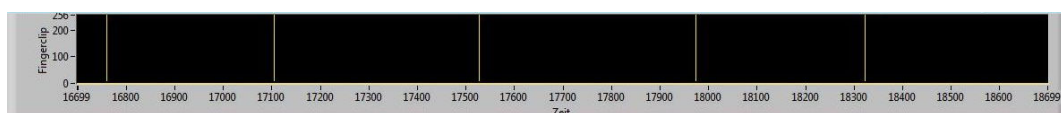
Figure 6.10: Hypothetical absolute positions of ocular layers determined on an A-scan. Peak 3 (at $6.116 \mu\text{m}$), the strongest reflecting layer may be the RPE or BM. Peak 1 (at $5.964 \mu\text{m}$) and peak 2 (at $5.970 \mu\text{m}$) could be the ILM and NFL. The peaks 4 (at $6.146 \mu\text{m}$), 5 (at $6.158 \mu\text{m}$) and 6 (at $6.168 \mu\text{m}$) may correspond to choroidal structures, while peaks 7 (at $6.250 \mu\text{m}$), 8 (at $6.260 \mu\text{m}$) and 9 (at $6.281 \mu\text{m}$) could presumably assigned to scleral structures.

Recorded Interferograms

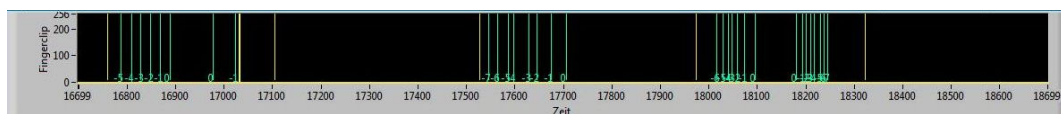
After an A-scan was recorded, the flip mirror of the system is flipped over and the fundus pulsation measurement can be started. The stepping motor is positioned according to the peak of interest in the A-scan. If the system was not misaligned or the rat was not moving, the synthetic interferogram (see Figure 6.11a) can now be seen on the monitor and it can be recorded. If it is not the case, the measurement should be started again, a new A-scan has to be recorded.



(a) Interferogram recorded on rat-5 at 9.4315 (the strongest reflecting layer).



(b) Manually determination of the pulse periods.



(c) Counting the fringes manually.

Figure 6.11: Synthetic interferogram recorded on rat-5 from the most reflecting layer (at position 9.5835). Based on the interferogram the pulse periods are manually determined and the fringes will be counted.

In the following paragraphs, the evaluation procedure is described and demonstrated with figures.

Determination of the Pulse Periods. The first step of the evaluation of interferograms is the determination of pulse periods (see Figure 6.11b). This happens manually, based on the periodically repeating fringes on the interferogram. From the beat-to-beat intervals, the instantaneous pulse rate (IPR) can be determined: IPR is the reciprocal of the beat-to-beat interval. In practice, for a recorded interferogram the pulse periods can not be determined for the whole length of recording: there are larger “gaps” between groups of “consecutive” or “standalone” intervals. Creating a

boxplot (see Figure 6.12 and Figure 6.13 for boxplots of measurements on a rat) from the beat-to-beat intervals or from the IPRs, one can have an idea about, how good the pulse periods were determined. Typical unanesthetized rat HRs value 320–480 bpm [50], but HRs in anesthesia are much below these values (exact HRs depend on several factors, as described in a section above). Outliers (see Figure 6.12) below the mean indicate “gaps” in the beat-to-beat intervals, while outliers above the mean indicates that there are beats marked too dense. The latter is likely a consequence of the poor quality of the synthetic interferogram and the subjective decision of the evaluating person. Figure 6.13 shows the same data, but without outliers: it draws attention if the evaluation process should be revised. In case of this animal, most IPR values are not extreme high or low, but IPR values at positions 9.6302 and 9.7388 are much smaller than the others. The reason for this is the poor quality of the recorded interferograms (see Figure 6.14), and thus an obviously wrong determination of the pulse periods. The length of the pulse periods in reality may be about twice so short than determined during the evaluation. It is not possible to explain these values further. Variations to other rats give also no useful information because of the individual differences between the animals. Summing up, the determination of pulse periods (beat-to-beat intervals) is assumed to be correct.

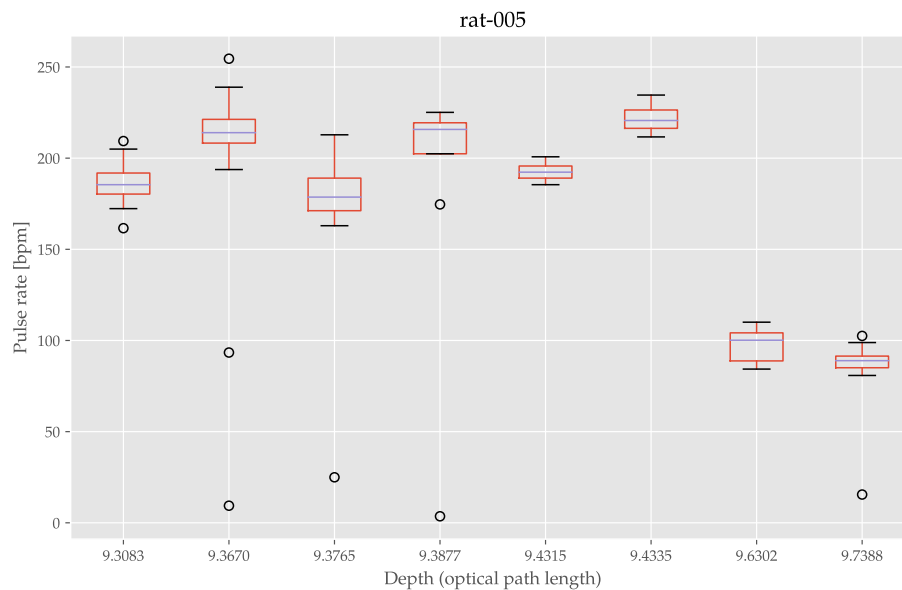


Figure 6.12: Boxplot from the IPR values of rat-5. Outliers can indicate the quality of the recorded interferogram and of the beat-to-beat interval determination.

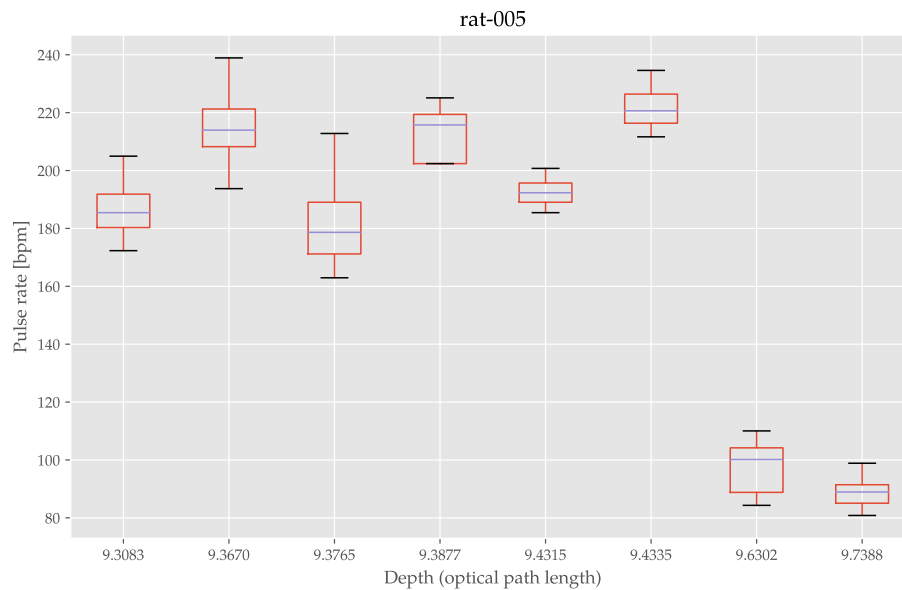
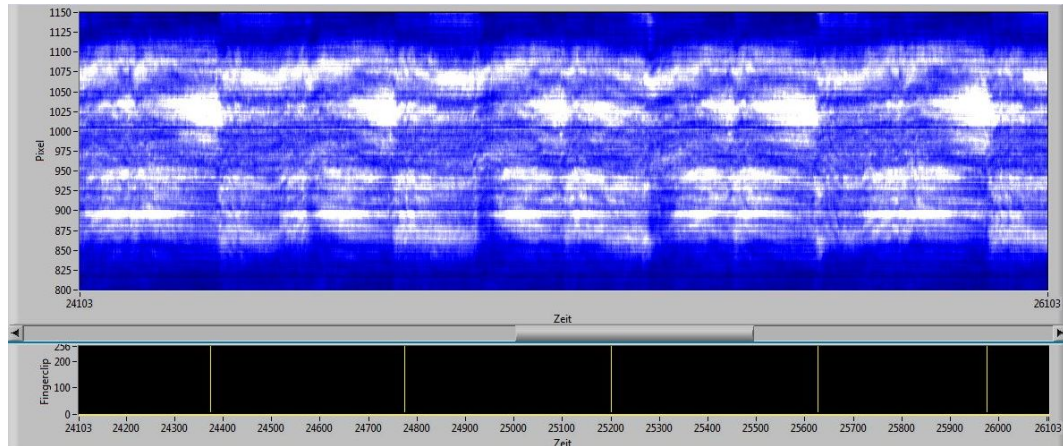


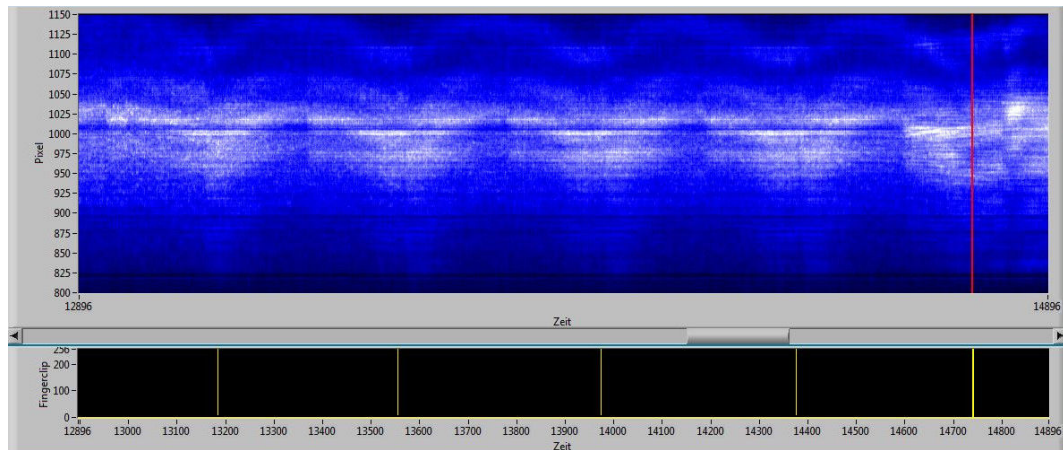
Figure 6.13: Boxplot from the IPR values (rat-5), without outliers: it shows that IPR values of the animal are not extreme (rats are in anesthesia), they can be accepted, except at positions 9.6302 and 9.7388. For more explanation see the text.

Time Course of Fundus Pulsation & FPA. By counting the fringes (see Figure 6.11c) and averaging it over several pulse periods, the time course and amplitude of the fundus pulsation (see Figure 6.15) can be determined at the layer the measurement was carried out. Errors in the measurement of FPA are introduced by blinking or eye movements, that reduce image quality and may cause individual fringes to be missed or counted twice. Differences in the biomechanical properties of the respective tissue areas can lead to different time courses of the fundus movement. The observed time course could be influenced by the pathway of the probe beam, which differs between the measurement in the macula (beam entering in the center of the cornea) and the ONH (beam entering nasal of the center, where corneal pulsations are assumed to be smaller) [30].

Figure 6.16 shows two time courses of fundus pulsation observed on an other rat at two different positions. Figure 6.16a may be observed at the RPE or BM, while Figure 6.16b could be observed at the sclera (Figure 6.17 shows the recorded synthetic interferogram, this latter time course is based on.).



(a) Synthetic interferogram and manually determined pulse periods on rat-5 at position 9.6302.



(b) Synthetic interferogram and manually determined pulse periods on rat-5 at position 9.7388.

Figure 6.14: Synthetic interferograms recorded on rat-5 at positions 9.6302 and 9.7388. The pulse periods were manually determined based on the interferograms.

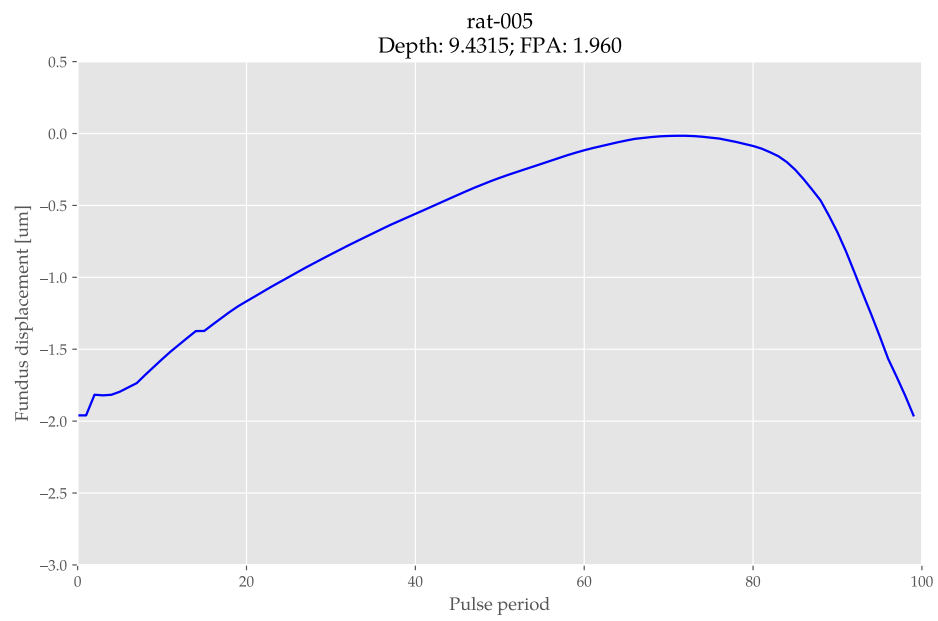
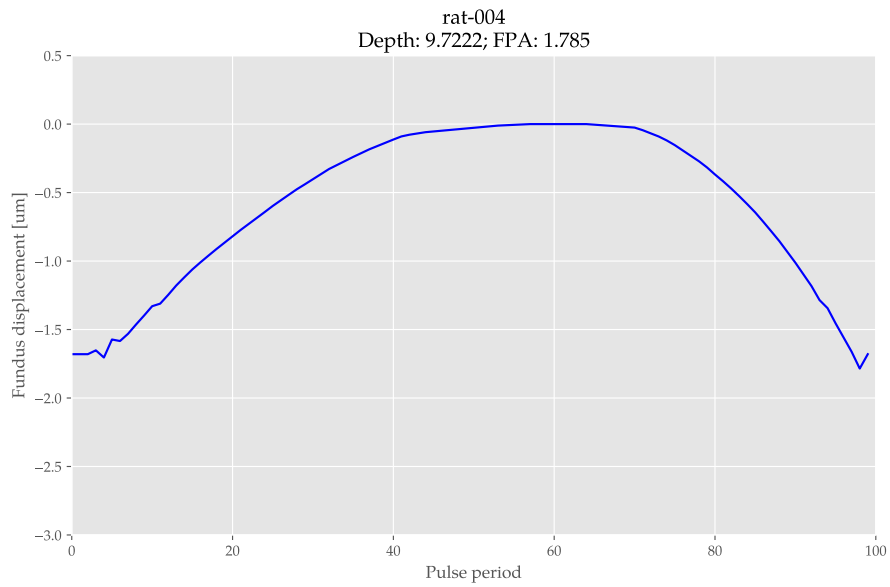
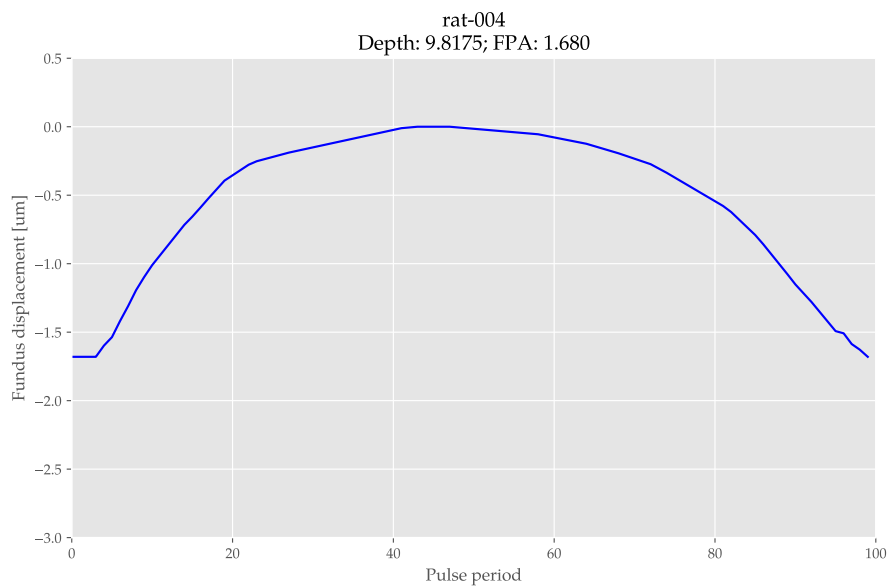


Figure 6.15: Time course of fundus pulsation.



(a) Recorded at position 9.7223 (most probably the RPE or BM).



(b) Recorded at position 9.8175 (could be a scleral structure).

Figure 6.16: Time courses of fundus pulsation on rat-4, observed at two different layers.

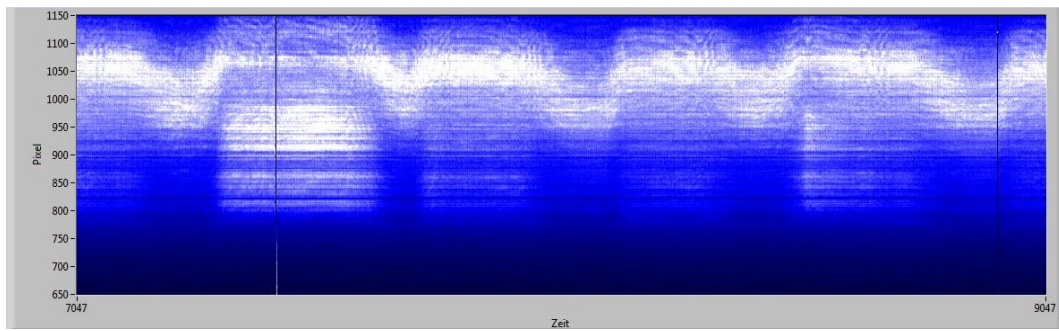


Figure 6.17: Synthetic interferogram recorded on rat-4 at 9.8175.

Chapter 7

Conclusion and Future Work

This master thesis is the first step for establishment of an LCTI system for studying both dynamic and long-term variations in axial position of ocular structures in rodent's eyes. The system allows for both estimation of pulsatile ocular blood flow and measurement of real-time growth of axial eye length in myopia models.

In the course of this master thesis, after elaboration of the special literature, an LCTI system has been built up and adapted to the characteristics of the rat eye.

There were some incompatibility issues between new hardware and software, the existing LabView code was updated accordingly.

In vitro measurements on phantom structures were performed before *in vivo* rat experiments to test and verify the system is functioning correctly and gives usable results.

In vivo results show that it is possible to identify all intraocular layers (including sclera); however, performing further measurements (preferably after some modifications on the system described in the next section below) would be necessary to reliably observe and record fundus pulsations at any arbitrary layer. The author's inexperience with *in vivo* experiments caused a higher failure rate concerning the number of evaluable recordings, as well as with increasing experience, the length of measurement in one position showed a decreasing tendency, which results in a higher number of recordings in the available time.

Currently available recorded interferograms from the strongest reflecting layer have in general better image qualities, and thus could be evaluated easier, than interferograms from other layers, e.g., sclera. Interferograms recorded from layers more behind the strongest reflecting layer show *visible differences* (these could be further investigated in future) as opposed to interferograms attributed to e.g. the RPE. Former, show some periodicity, which in some cases enables the determination of pulse periods but unfortunately in most cases there are no fringes visible, i.e. determination of time courses and FPAs are not possible.

Unfortunately, only in one case, in one position could be the time course of fundus pulsation from a probably scleral layer determined; to validate this, more evaluable recordings would be needed.

Nevertheless, AEL measurements show promising results in identification of all intraocular layers, and the system built up in the course of this master thesis can be improved further, to allow OFP measurements with a higher success rate.

Possible Modifications on the LCTI System

Instead of the current used adjustable holder a stereotaxic rat holder could be used for more precise positioning of the experimental animal. This would allow eliminate more movements, thus resulting in better quality interferograms.

The integration of a fundus camera into the system could help to register the measurement position and would allow to perform measurements on the exact same position.

Possible misadjustments of the system can be prevented by motorizing the flip mirror.

Although the used optical isolator is polarization independent, there are some losses. Placing a polarization controller also right before the optical isolator may improve the effective power on the sample.

The currently used SLD could be replaced by an other one with central frequency at 1060 nm to reach deeper penetration of the probing beam.

Additional Measurements on the Animals

Monitoring and recording vital parameters (e.g., heart rate, respiratory rate, body temperature, body weight, etc.) of the rat before and during the LCTI measurement could help individual biological characteristics to take into account.

In vivo OCT and/or *ex vivo* histology of the animal's eye ball would be very helpful to determine the anatomical structures and thus it would validate the results.

References

- [1] Nikolaus Dragostinoff, René M. Werkmeister, Martin Gröschl, and Leopold Schmetterer. "Depth-resolved measurement of ocular fundus pulsations by low-coherence tissue interferometry". In: *Journal of Biomedical Optics* 14.5 (2009). DOI: <http://dx.doi.org/10.1117/1.3251049>.
- [2] World Health Organisation. *Visual impairment and blindness. Fact Sheet N°282*. 2014. URL: <http://www.who.int/mediacentre/factsheets/fs282/en/> (accessed on 2016-02-23).
- [3] World Health Organisation. *Visual Impairment and Blindness 2010*. URL: http://www.who.int/blindness/data_maps/VIFACTSHEETGLOBALDAT2010_1.pdf (accessed on 2016-03-10).
- [4] Donatella Pascolini and Silvio Paolo Mariotti. "Global estimates of visual impairment: 2010". In: *British Journal of Ophthalmology* (2011-12-01), [bjophthalmol-2011-300539](https://doi.org/10.1136/bjophthalmol-2011-300539). DOI: 10.1136/bjophthalmol-2011-300539. URL: <http://bjo.bmj.com/content/early/2011/11/30/bjophthalmol-2011-300539> (accessed on 2016-03-11).
- [5] Josef Flammer, Selim Orgül, Vital P. Costa, Nicola Orzalesi, Günter K. Krieglstein, Luis Metzner Serra, Jean-Paul Renard, and Einar Stefánsson. "The impact of ocular blood flow in glaucoma". In: *Progress in Retinal and Eye Research* 21.4 (2002-07), pp. 359–393.
- [6] A. Harris, H. S. Chung, T. A. Ciulla, and L. Kagemann. "Progress in measurement of ocular blood flow and relevance to our understanding of glaucoma and age-related macular degeneration". In: *Progress in Retinal and Eye Research* 18.5 (1999-09), pp. 669–687.
- [7] A Mendívil, V Cuartero, and M P Mendívil. "Ocular blood flow velocities in patients with proliferative diabetic retinopathy and healthy volunteers: a prospective study." In: *The British Journal of Ophthalmology* 79.5 (1995-05), pp. 413–416. URL: <http://www.ncbi.nlm.nih.gov/pmc/articles/PMC505126/> (accessed on 2016-03-11).

References

- [8] Gerard J Tortora and Bryan H Derrickson. *Principles of anatomy and physiology*. 13th. Hoboken, N J: Wiley, 2011.
- [9] M. J. A. Girard, N. G. Strouthidis, A. Desjardins, J. M. Mari, and C. R. Ethier. "In vivo optic nerve head biomechanics: performance testing of a three-dimensional tracking algorithm". In: *Journal of The Royal Society Interface* 10.87 (2013-07-24), pp. 20130459–20130459. DOI: 10.1098/rsif.2013.0459. URL: <http://rsif.royalsocietypublishing.org/cgi/doi/10.1098/rsif.2013.0459> (accessed on 2016-02-09).
- [10] Henry Gray. *Gray's Anatomy: the anatomical basis of clinical practice*. Ed. by Susan Standring. 39th. Edinburgh [u.a.]: Elsevier, Churchill Livingstone, 2005.
- [11] János Szentágothai. *Functional anatomy*. Budapest: Medicina Könyvkiadó, 1971.
- [12] Henry Gray. *Gray's Anatomy: the anatomical basis of clinical practice*. Ed. by Susan Standring. 40th. Elsevier Limited, 2008.
- [13] The Retina Reference. *Normal Retinal Anatomy*. URL: <http://www.retinareference.com/anatomy/> (accessed on 2016-04-21).
- [14] Health Partners Optical. *Optical Coherence Tomography. Determining the health of your eye*. URL: <http://www.healthpartners.com.au/optical/products/eye-examinations/optical-coherence-tomography> (accessed on 2016-04-21).
- [15] World Health Organisation. "Glaucoma is second leading cause of blindness globally". In: *Bulletin of the World Health Organization* 82.11 (2004), pp. 811–890. (Accessed on 2016-02-15).
- [16] H. A. Quigley and A. T. Broman. "The number of people with glaucoma worldwide in 2010 and 2020". In: *British Journal of Ophthalmology* 90.3 (2006-03-01), pp. 262–267. DOI: 10.1136/bjo.2005.081224. URL: <http://bjo.bmj.com/content/90/3/262> (accessed on 2016-03-04).
- [17] Glaucoma Research Foundation. *Childhood Glaucoma*. 2015. URL: <http://www.glaucoma.org/glaucoma/childhood-glaucoma-1.php> (accessed on 2016-02-24).
- [18] Glaucoma Research Foundation. *Types of Glaucoma*. 2015. URL: <http://www.glaucoma.org/glaucoma/types-of-glaucoma.php> (accessed on 2016-02-10).

References

- [19] National Eye Institute, National Institute of Health. *Facts About Age-Related Macular Degeneration*. 2015. URL: https://nei.nih.gov/health/maculardegen/armd_facts (accessed on 2016-01-27).
- [20] National Eye Institute, National Institute of Health. *A scene as it might be viewed by a person with age-related macular degeneration*. 2012. URL: <https://www.flickr.com/photos/nationaleyeinstitute/7544733860/> (accessed on 2016-03-16).
- [21] Jennifer I. Lim, ed. *Age-Related Macular Degeneration, Third Edition*. 3 edition. CRC Press, 2012-11-15. 406 pp.
- [22] National Eye Institute, National Institute of Health. *Facts About Diabetic Eye Disease*. 2015. URL: <https://nei.nih.gov/health/diabetic/retinopathy> (accessed on 2016-02-12).
- [23] Anne Hanson. "The Rat's Eyes". In: *Rat behavior and biology*. (2009-06-11). URL: <http://ratbehavior.org/Eyes.htm> (accessed on 2016-01-11).
- [24] Theo G. M. F. Gorgels and Dirk van Norren. "Spectral Transmittance of the Rat Lens". In: *Vision* 32.8 (1992), pp. 1509–1512.
- [25] Philip M. Meier and Pamela Reinagel. "Rats and humans differ in processing collinear visual features". In: *Frontiers in Neural Circuits* (2013).
- [26] Gesine Huber, Severin Heynen, Coni Imsand, Franziska vom Hagen, Regine Muehlfriedel, Naoyuki Tanimoto, Yuxi Feng, Hans-Peter Hammes, Christian Grimm, Leo Peichl, Mathias W. Seeliger, and Susanne C. Beck. "Novel Rodent Models for Macular Research". In: *PLoS ONE* 5.10 (2010), e13403.
- [27] *Mouse Schematic Eye; Rat Schematic Eye; Human Schematic Eye*. URL: <http://prometheus.med.utah.edu/~marclab/protocols.html> (accessed on 2011-11-16).
- [28] Jaime L. Masferrer, Kathleen M. Leahy, Alane T. Koki, Ben S. Zweifel, Steven L. Settle, B. Mark Woerner, Dorothy A. Edwards, Amy G. Flickinger, Rosalyn J. Moore, and Karen Seibert. "Antiangiogenic and Antitumor Activities of Cyclooxygenase-2 Inhibitors". In: *Cancer Research* 60 (2000-03), pp. 1360–1311.
- [29] Dietmar Link, Clemens Strohmaier, Bernd U. Seifert, Thomas Riemer, Herbert A. Reitsamer, Jens Haueisen, and Walthard Vilser. "Novel non-contact retina camera for the rat and its application to dynamic retinal vessel analysis". In: *Biomedical Optics Express* 2.11 (2011), pp. 3094–3108. DOI: <http://dx.doi.org/10.1364/BOE.2.003094>.

References

- [30] Nikolaus Dragostinoff. "Low Coherence Tissue Interferometry for the Depth-Resolved Measurement of Ocular Fundus Pulsations". PhD thesis. Vienna University of Technology, 2010-09.
- [31] Anne Hanson. "What Do Rats See?" In: *Rat behavior and biology*. (2007-03-14). URL: <http://ratbehavior.org/RatVision.htm> (accessed on 2016-01-11).
- [32] Bahaa E. A. Saleh and Malvin Carl Teich. *Fundamentals of Photonics*. 2nd ed. 2007.
- [33] Robert D. Guenther. *Modern optics*. Wiley, 1990.
- [34] F. Graham Smith, Terry A. King, and Dan Wilkins. *Optics and Photonics: An Introduction*. 2nd ed. John Wiley & Sons, 2007.
- [35] A. F. Fercher, C. K. Hitzenberger, W. Drexler, L. Schmetterer, O. Findl, and H. Sattmann. *Optical coherence biometry in ophthalmology*. Vol. 2. Research Signpost, 2002.
- [36] Christoph K. Hitzenberger. "Optical Measurement of the Axial Eye Length by Laser Doppler Interferometry". In: *Investigate Ophthalmology & Visual Science* 32.3 (1991-03).
- [37] Adolf Friedrich Fercher. "Optical Coherence Tomography". In: *Journal of Biomedical Optics* 1.2 (1996-04), pp. 157–173.
- [38] Wolfgang Drexler and James G. Fujimoto, eds. *Optical Coherence Tomography. Technology and Applications*. Springer, 2008.
- [39] Wolfgang Drexler and James G. Fujimoto. "State-of-the-art retinal optical coherence tomography". In: *Progress in Retinal and Eye Research* 27 (2008), pp. 45–48.
- [40] *First in vivo ultrahigh resolution OCT*. URL: <http://www.zmpbmt.meduniwien.ac.at/index.php?id=320> (accessed on 2016-01-27).
- [41] Afif Elghraoui and Yuan Huan Lo. "Laser Doppler Velocimetry". 2010. URL: http://tff2009.ucsd.edu/neurophysics/courses/physics_173_273/Phys_173_LDV_2010.pdf.
- [42] Adolf Friedrich Fercher. "In Vivo Measurement of Fundus Pulsations By Laser Interferometry". In: *IEEE Journal of Quantum Electronics* QE-20.12 (1984-12), pp. 1469–1471.

References

- [43] L. Schmetterer, F. Lexer, C. J. Unfried, H. Sattmann, and A. F. Fercher. "Topical Measurement of fundus pulsations". In: *Optical Engineering* 34 (1995), pp. 711–716.
- [44] A Gullstrand. "The dioptrics of the eye". In: *Helmholtz's Treatise on Physiological Optics*. Ed. by J. P. C. Southall. Vol. 1. Optical Society of America, 1924, pp. 351–352.
- [45] E. Chen. "Refractive indices of the rat retinal layers." In: *Ophthalmic Research* 25.1 (1993), pp. 65–68.
- [46] Thomas Blaschke. "Adjustable holder for Optical Coherence Tomography eye measurements in rats. Projektarbeit, TU Wien". 2015.
- [47] Mikhail N. Polyanskiy. *Refractive index database*. URL: <https://refractiveindex.info> (accessed on 2016-05-03).
- [48] John P. Hannon. "Effect of Temperature on the Heart Rate, Electrocardiogram and Certain Myocardial Oxidations of the Rat". In: *Circulation Research* 6 (6 1958).
- [49] Sepideh Hariri, Man Chun Tam, Donghyun Lee, Denise Hileeto, Alireza Akhlagh Moayed, and Kostadinka Bizheva. "Noninvasive imaging of the early effect of sodium iodate toxicity in a rat model of outer retina degeneration with spectral domain optical coherence tomography". In: *Journal of Biomedical Optics* 18.2 (2013), pp. 026017–026017. DOI: 10.1117/1.JBO.18.2.026017. URL: <http://dx.doi.org/10.1117/1.JBO.18.2.026017>.
- [50] Anne Hanson. "Biological Statistics of the Norway Rat". In: *Rat behavior and biology*. (2005-08-11). URL: <http://www.ratbehavior.org/Stats.htm> (accessed on 2017-02-07).

List of Figures

1.1	The ratio of VI and blindness to the world population	2
1.2	Most common global causes of VI	2
1.3	Most common global causes of blindness	3
2.1	Superior view of transverse section of right eyeball	5
2.2	Schematic of a human eye; OCT of human ONH	5
2.3	Drawing of a histological section through the choroid	7
2.4	Retinal cell layers	10
2.5	HD-OCT scan of a healthy retina	10
2.6	The two most common types of glaucoma	14
2.7	Comparing normal vision and vision affected by age-related macular degeneration	15
2.8	Comparing normal vision and vision affected by diabetic retinopathy and diabetic macular edema, respectively	17
2.9	Schematical cross sections of the human and rat eye	17
2.10	Schematic ZEMAX illustrations of the dimensions of the rat eye in relation to the human eye	19
3.1	Dynamic length measurement interferometry.	35
3.2	Partial Coherence Interferometry (PCI)	36
3.3	Schematic diagram of a dual beam PCI	37
3.4	IOL master (Zeiss, Jena, Germany)	38
3.5	In vivo sub-cellular resolution OCT	38
3.6	Synthetic interferogram with corresponding contraction-dilatation graph	39
3.7	Schematic diagram of an LCTI system	40
3.8	Losses on the non-polarizing BSC of the Michelson interferometer	41
3.9	Operational principle of the PBSC	42
3.10	Effect of the QWP to the polarization state of the beam	43
3.11	A-scan of a human volunteer	44
3.12	Interference pattern is recorded with the time	45
4.1	LCTI system built by Dragostinoff for human measurements	46
4.2	Contrast of the fringe system vs distance from the cornea	50
4.3	Calculation for lens positioning	53
4.4	The new, adapted system	54
4.5	New CCD cameras from Conrad	55

List of Figures

4.6	Adjustable holder for Optical Coherence Tomography eye measurements in rats	56
5.1	NI-DAQ PCI-6034E	59
5.2	Old and new PCI cards from Stresing Ing. Büro (Berlin, Germany) . .	61
6.1	A standard microscope slide	66
6.2	Resulting A-scan from a microscope slide	67
6.3	The artificial eye	68
6.4	Resulting A-scan from the artificial eye	69
6.5	The experimental setup built up in the animal lab	70
6.6	Changes in heart rate of anesthetized rats during hypothermia	72
6.7	Similar image is shown on the monitor, if the experimental eye is in a good position.	73
6.8	A-scan of a rat	75
6.9	UHR-OCT tomogram acquired from a healthy rat retina	76
6.10	Hypothetical positions of ocular layers determined on an A-scan . . .	77
6.11	Synthetic interferogram recorded on rat-5 from the most reflecting layer	78
6.12	Boxplot from the IPR values.	79
6.13	Boxplot from the IPR values, without outliers	80
6.14	Strange synthetic interferograms recorded on rat-5	81
6.15	Time course of fundus pulsation	82
6.16	Time courses of fundus pulsations on rat-4, observed at two different layers	83
6.17	Synthetic interferogram on rat-4	84
A.1	Wavelength dependent transmission of the non-polarising BSC	106
B.1	Augenlaenge.vi: front panel	111
B.2	Augenlaenge.vi: modifications	112
B.3	filename.vi: new subVI to help consequent filenaming	113
B.4	Kamera.vi: front panel	114
B.5	KameraInit.vi: block diagram	115
B.6	Kamera.vi: modifications on the block diagram	116
B.6	Kamera.vi (cont.): modifications on the block diagram	117
B.7	LadenProgrammLCTI.vi: front panel	118

List of Tables

2.1	Curvature and thickness of the cornea and sclera	6
2.2	Dimensions of the rat and human eyes	18
2.3	Parameters for Gullstrand's schematic eye and for the rSRE	18
4.1	Calculations for lens positioning	52
5.1	Technical specifications of the new computer	58
5.2	Differences between the old and the new LCCD PCI cards	60
6.1	Distances between adjacent ocular layers in the rat eye	76

Acronyms and Abbreviations

- ACG** angle-closure glaucoma 13, 14
- AEL** axial eye length 3, 65, 75, 88
- AMD** age-related macular degeneration 2, 3, 14, 15
- APD** avalanche photodiode 35, 48, 64
-
- BM** Bruch's membrane 76, 82
- BSC** beam splitter cube 29, 48, 56
-
- CCD** charge-coupled device 32
- CRA** central retinal artery 9
- CRT** cathode ray tube 75
- CRV** central retinal vein 9
-
- DAC** data acquisition card 59, 64
- DAQ** data acquisition 60
- DG** developmental glaucoma 14
- DME** diabetic macular edema 16
- DOF** depth of focus 18
- DR** diabetic retinopathy 2, 3, 16
-
- ELM** external limiting membrane 9, 11
-
- FD-OCT** Fourier domain optical coherence tomography 32
- FFT** fast Fourier Transform 64
- FM** flip mirror 53
- FPA** fundus pulsation amplitude 34, 82, 87
- FWHM** full width at half maximum 28, 48

Acronyms and Abbreviations

- GCL** ganglion cell layer 9, 12
- GIMP** GNU Image Manipulation Program 76
- HR** heart rate 74, 81
- iFFT** inverse FFT 64
- ILM** inner limiting membrane 1, 9, 76, 79
- INL** inner nuclear layer 9, 11, 12
- IO** intraocular 34
- IOP** intraocular pressure 12, 14
- IPL** inner plexiform layer 9, 12
- IPR** instantaneous pulse rate 80, 81
- LabVIEW** Laboratory Virtual Instrument Engineering Workbench 59, 60, 62, 64–66, 102
- LCCD** linear CCD array 34, 35, 45, 48, 49, 53, 59–62, 64, 65
- LCI** low coherence interferometry 31, 32
- LCTI** low-coherence tissue interferometry iii, 1, 3, 18, 21, 34, 45, 47, 59, 73–75, 87, 88
- LDV** laser dopler velocimetry 33
- LS** light source 29
- NDR** nonproliferative diabetic retinopathy 16
- NFL** nerve fibre layer 9, 12, 76, 79
- NTG** normal-tension glaucoma 14
- OAG** open-angle glaucoma 13, 14
- OBF** ocular blood flow 4, 33
- OCT** optical coherence tomography 31, 32, 57, 76, 88
- OFDI** optical frequency domain imaging 32
- OFFP** ocular fundus pulsation 1, 18, 33, 65, 75, 88
- ON** optic nerve 9
- ONH** optic nerve head 9, 12, 82

Acronyms and Abbreviations

- ONL** outer nuclear layer 9, 11
- OPD** optical path difference 28–30
- OPL¹** outer plexiform layer 9, 11
- OPL²** optical path length 23, 29, 75
- OS** operating system 59, 60, 64
-
- PACG** primary angle-closure glaucoma 14
- PBSC** polarizing beam splitter cube 35, 48, 53
- PC²** personal computer 59, 60
- PCI** partial coherence interferometry 29–32, 34, 45, 59–63, 65
- PD** photodetector 29, 30, 35
- PDR** proliferative diabetic retinopathy 16
- POAG** primary open-angle glaucoma 14
- POBF** pulsatile ocular blood flow 3
-
- QWP** quarter wave plate 35, 48
-
- RPE** retinal pigment epithelium 1, 9, 15, 16, 34, 76, 82, 87
- rSRE** reduced schematic rat eye 19, 20, 50
-
- SG** secondary glaucoma 14
- SLD** superluminescent diode 30, 35, 48, 88
- SM** stepping motor 48
-
- TD-OCT** time domain optical coherence tomography 32
- TOPL** total optical path length 29
-
- UHR-OCT** ultra high resolution OCT 76
-
- VI** visual impairment 1, 2
-
- XP** Microsoft Windows XP 59

Appendices

A Technical Specifications

Due to the extent of this thesis, only the first page of technical datasheets and manuals are included; these documents are available for download at the manufacturers homepage, or a printed copy can be found at the Center for Medical Physics and Biomedical Engineering, Medical University Vienna.

A.1 Datasheet NI-DAQ

http://www.ni.com/pdf/products/us/4daqsc202-204_ETC_212-213.pdf, accessed on 2017-02-10.

Low-Cost E Series Multifunction DAQ – 12 or 16-Bit, 200 kS/s, 16 Analog Inputs

NI E Series – Low-Cost

- 16 analog inputs at up to 200 kS/s, 12 or 16-bit resolution
- Up to 2 analog outputs at 10 kS/s, 12 or 16-bit resolution
- 8 digital I/O lines (TTL/CMOS); two 24-bit counter/timers
- Digital triggering
- 4 analog input signal ranges
- NI-DAQ driver that simplifies configuration and measurements

Families

- NI 6030E
- NI 6034E
- NI 6035E
- NI 6024E
- NI 6023E

Operating Systems

- Windows 2000/NT/XP
- Real-time performance with LabVIEW
- Others such as Linux® and Mac OS X

Recommended Software

- LabVIEW
- LabWindows/CVI
- Measurement Studio
- VI Logger

Other Compatible Software

- Visual Basic, C/C++, and C#

Driver Software (included)

- NI-DAQ 7



Family	Bus	Analog Inputs	Input Resolution	Max Sampling Rate	Input Range	Analog Outputs	Output Resolution	Output Rate	Output Range	Digital I/O	Counter/Timers	Triggers
NI 6030E	PCI, PCMCIA	16 SE/8 DI	16 bits	200 kS/s	±0.05 to ±10 V	2	16 bits	10 kS/s ¹	±10 V	8	2, 24-bit	Digital
NI 6034E	PCI	16 SE/8 DI	16 bits	200 kS/s	±0.05 to ±10 V	0	–	–	–	8	2, 24-bit	Digital
NI 6025E	PCI, PXI	16 SE/8 DI	12 bits	200 kS/s	±0.05 to ±10 V	2	12 bits	10 kS/s ¹	±10 V	8	2, 24-bit	Digital
NI 6024E	PCI, PCMCIA	16 SE/8 DI	12 bits	200 kS/s	±0.05 to ±10 V	2	12 bits	10 kS/s ¹	±10 V	8	2, 24-bit	Digital
NI 6023E	PCI	16 SE/8 DI	12 bits	200 kS/s	±0.05 to ±10 V	0	–	–	–	8	2, 24-bit	Digital

¹10 kS/s typical when using the single DMA channel for analog output. 1 kS/s maximum when using the single DMA channel for either analog input or counter/timer operations. 1 kS/s maximum for PCMCIA DAQCard devices in all cases.

Table 1. Low-Cost E Series Model Guide

Overview and Applications

National Instruments low-cost E Series multifunction data acquisition devices provide full functionality at a price to meet the needs of the budget-conscious user. They are ideal for applications ranging from continuous high-speed data logging to control applications to high-voltage signal or sensor measurements when used with NI signal conditioning. Synchronize the operations of multiple devices using the RTSI bus or PXI trigger bus to easily integrate other hardware such as motion control and machine vision to create an entire measurement and control system.

Highly Accurate Hardware Design

NI low-cost E Series DAQ devices include the following features and technologies.

Temperature Drift Protection Circuitry – Designed with components that minimize the effect of temperature changes on measurements to less than 0.0010% of reading/°C.

Resolution-Improvement Technologies – Carefully designed noise floor maximizes the resolution.

Onboard Self-Calibration – Precise voltage reference included for calibration and measurement accuracy. Self-calibration is completely software controlled, with no potentiometers to adjust.

NI DAQ-STC – Timing and control ASIC designed to provide more flexibility, lower power consumption, and a higher immunity to noise and jitter than off-the-shelf counter/timer chips.

NI MITE – ASIC designed to optimize data transfer for multiple simultaneous operations using bus mastering with one DMA channel, interrupts, or programmed I/O.

NI PGIA – Measurement and instrument class amplifier that guarantees settling times at all gains. Typical commercial off-the-shelf amplifier components do not meet the settling time requirements for high-gain measurement applications.

PFI Lines – Eight programmable function input (PFI) lines that you can use for software-controlled routing of interboard and intraboard digital and timing signals.

RTSI or PXI Trigger Bus – Bus used to share timing and control signals between two or more PCI or PXI devices to synchronize operations.

RSE Mode – In addition to differential and nonreferenced single-ended modes, NI low-cost E Series devices offer the referenced single-ended (RSE) mode for use with floating-signal sources in applications with channel counts higher than eight.

Onboard Temperature Sensor – Included for monitoring the operating temperature of the device to ensure that it is operating within the specified range.



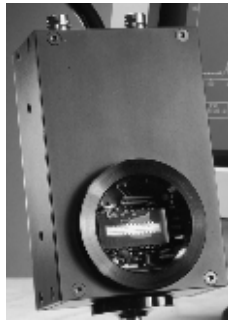
A.2 Manual for Stresing LCCD Camera System

Manual

for CCD - line scan camera system CCD1000



and for CCD - line scan camera system CCD 2000



Version: 2.4/ 2014

© Entwicklungsbüro G. Stresing

i

A.3 Fiber Collimator: HPUCO-23-850-S-6.2AS, OZ Optics


OZ Optics
www.ozoptics.com

14 Westbrook Rd., Orange, ON, Canada, M9A 1L6 Toll Free: 1-800-361-0411 Tel: (416) 831-0991 Fax: (416) 836-5093 E-mail: sales@ozoptics.com

COLLIMATORS AND FOCUSERS – RECEPTACLE STYLE

FEATURES:

- High power handling
- Rugged and compact design
- Low insertion loss
- Wide wavelength range
- Wide range of beam diameters
- GRIN, aspheric, achromatic, plano-convex, and biconvex lenses available
- Singlemode, multimode, and polarization maintaining fiber versions
- Diffraction limited optics
- **LOW COST!**

APPLICATIONS:

- Fiber optic device packaging, including WDM's
- Splitters, and integrated optics
- Source to fiber coupling
- Fiber to detector coupling

SPECIFICATIONS:

- **Available Wavelengths:** 180nm - 2000nm
- **Polarization:**
- **Extinction ratios:** 20, 25, or 30dB
- **Beam Diameters:** 0.2 to 22mm
- **Spot size:** As small as <5 microns
- **Wavefront distortion:** $\lambda/4$ to $\lambda/10$
- **Insertion Loss:** ≤ 0.6 dB for 60mm separation
 ≤ 0.3 dB for 10mm separation

PRODUCT DESCRIPTION:

OZ Optics offers a complete line of fiber collimators and focusers with low backreflection, designed to collimate or focus light exiting a fiber to a desired beam diameter or spot size. By utilizing diffraction limited lenses, spot sizes of a few microns can be achieved. These devices can be used with laser diodes, photodiodes, acousto-optic modulators and other fiber optic devices. Collimators and focusers can be used as matched pairs to couple light in and out of optical devices. This makes them ideal for fiber packaging of devices.

For collimators, the collimated beam diameter (**BD**) and full divergence angle (**DA**) depends upon the focal length of the lens (**f**), the core diameter (**a**), and the fiber numerical aperture (**NA**). The collimated beam characteristics are given by:

$$BD(mm) = 2 \times f(mm) \times NA \quad DA(rad) = a(\mu m) / f(mm)$$

When using the above formulae, please exercise caution. Different definitions for the numerical aperture are used by fiber manufacturers. For instance, definitions based on 50 percent, 13.5 percent ($1/e^2$), 5 percent, and 1 percent intensity levels are all used.

OZ Optics standard tables list the definitions used for each fiber type, as well as conversion factors to convert values to $1/e^2$ values. OZ Optics uses $1/e^2$ definitions for its calculations of the beam diameter wherever possible.

PRELIMINARY



Collimators/Focusers With 20mm and 33mm Flanges



12mm OD Collimator/Focuser




11mm OD Collimator/Focuser


DTS0094
OZ Optics reserves the right to change any specifications without prior notice.
12-Jun-08 1

A.4 Optical Fiber: SM800-5.6-125, Thorlabs

<https://www.thorlabs.com/thorproduct.cfm?partnumber=SM800-5.6-125>, accessed on 2017-02-10.



Single Mode Fiber:
830 nm




Description

Thorlabs' specialty single mode fibers are engineered for a variety of applications including biotechnology, laser delivery, and telecommunications. These fibers offer enhanced bend-insensitivity as well as reduced splice loss while providing excellent resistance to bend induced loss similar to that of conventional type fibers.

SM800-5.6-125

Specifications

Geometrical & Mechanical	
Cladding Diameter	125 ± 1.0 μm
Coating Diameter	245 ± 15 μm
Core-Cladding Concentricity	≤ 1.0 μm
Coating Material	Dual Acrylate
Proof Test Level	1%, 2%, or 3% (100, 200, or 300 kpsi)
Operating Temperature	-55 to 85 °C



Optical	
Numerical Aperture (Nominal)	0.10 - 0.14
Attenuation ¹	<5 dB/km
Operating Wavelength ²	830 - 980 nm
Cut-Off Wavelength	660 - 800 nm
Mode Field Diameter ³	4.7 - 6.9 μm @ 830 nm

¹Attenuation is a worst-case value, quoted for the shortest design wavelength.
²The wavelength range is the spectral region between the cutoff wavelength and the bend edge, in which the fiber transmits the TEM₀₀ mode with low attenuation. For this fiber, the bend edge wavelength is typically 200 nm longer than the cut-off wavelength. At the design wavelengths of 830 nm, the launched power must be considered carefully as these fibers have germanosilicate cores, and as such are susceptible to color center generation.
³The Mode Field Diameter is a nominal, calculated value, estimated at the operating wavelength(s) using typical value of numerical aperture and cut-off wavelength.

US, Canada, & South America: +1-973-300-3000 | France: +33 (0) 970 444 844 | Europe: +49 (0) 8131-5956-0 | UK & Ireland: +44 (0)1353-654440
 Brazil: +55-16-3413 7062 | Scandinavia: +46-31-733-30-00 | Japan & Asia: +81-3-5979-8889 | China: +86 (0)21-60561122

January 13, 2015
12345-S01, Rev E

www.thorlabs.com

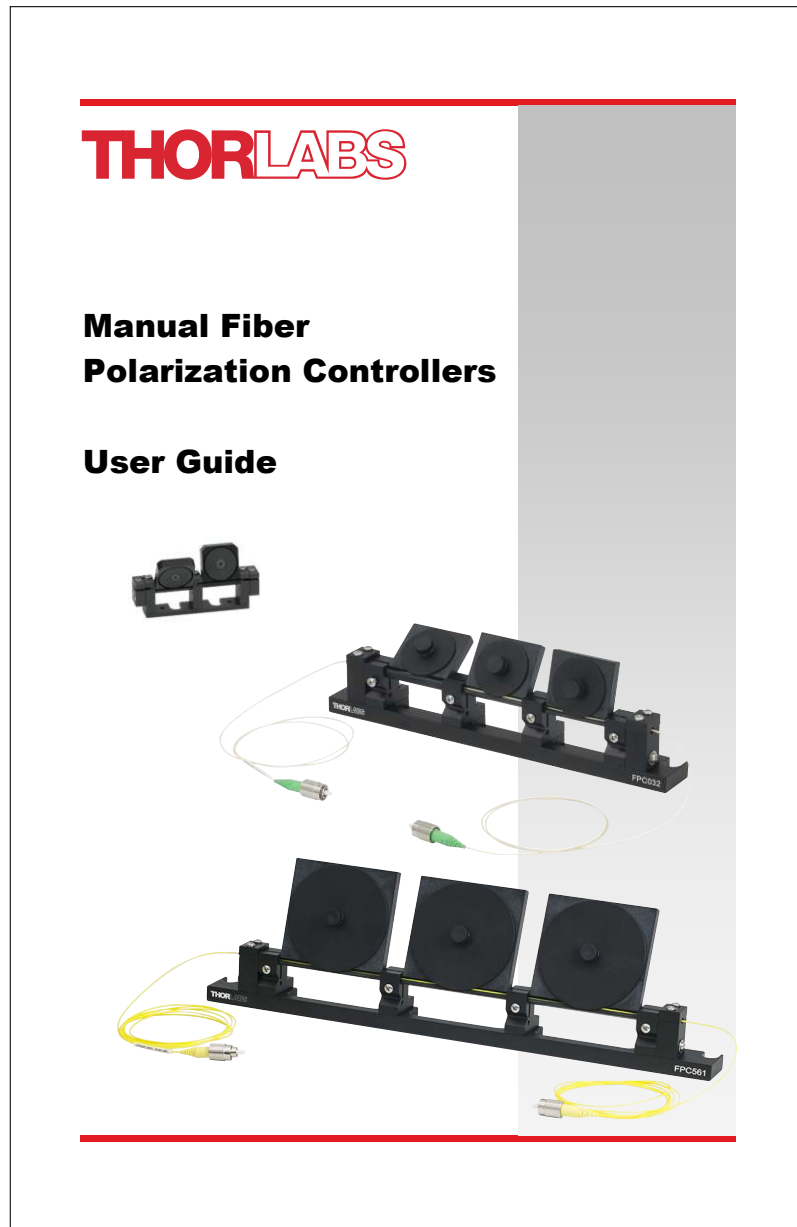
A.5 Optical Isolator: IO-F-850-APC, Thorlabs

<https://www.thorlabs.com/thorProduct.cfm?partNumber=IO-F-850APC>, accessed on 2017-02-10.



A.6 Polarisation Controller: FPC030, Thorlabs

<https://www.thorlabs.com/thorProduct.cfm?partNumber=FPC030>, accessed on 2017-02-10.



A.7 Beam Splitter Cube: , Thorlabs

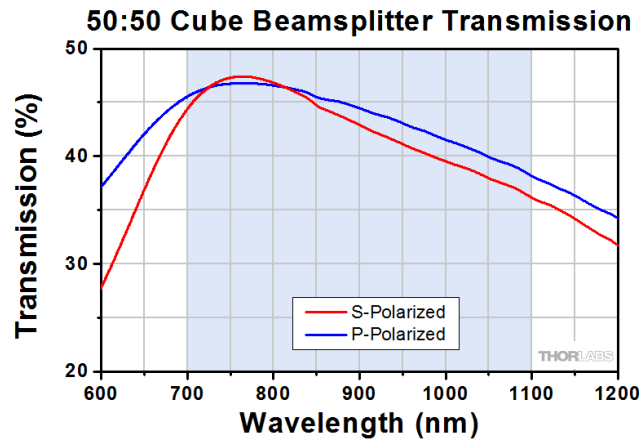


Figure A.1: Wavelength dependent transmission of the non-polarising beam splitter cube. Graph is taken from http://www.thorlabs.com/images/TabImages/BS014_Transmission_780.gif, accessed on 2017-02-10.

B LabVIEW

Listing B.1 shows all LabVIEW files, needed for the measurement as well as for the evaluation of the recorded data. There are 3 programs, each in a separate sub-folder; one for eye length measurement (Augenlaenge/Augenlaenge.vi), one for fundus pulsation measurement (Kamera/Kamera.vi) and one for data evaluation (LadenProgrammLCTI/LadenProgrammLCTI.vi).

Listing B.1: All LabVIEW files, needed for measurement and data evaluation.

```
/
|
|
+--- Augenlaenge
|   |   Augenlaenge.vi
|   |
|   +--- klajo
|   |   filename.vi
|   |
|   \--- subVIs
|       apd_run.vi
|       close2_gpib-32.vi
|       close_gpib-32.vi
|       close_gpib-32_ask.vi
|       DigitalFilter.vi
|       FindMaxima.vi
|       hvang-global_.vi
|       mm_to_samples.vi
|       ReadSettingD.vi
|       ReadSettingR.vi
|       samples_to_mm.vi
|       send_recv_gpib-32.vi
|       sm_counter.vi
|       sm_counter_init.vi
|       sm_init2_gpib-32.vi
|       sm_motorpos_0.vi
|       sm_move_abs.vi
|       sm_pos_gpib-32.vi
|       sm_status_gpib-32.vi
|       sm_wait.vi
```

```
|         TheCloser.vi
|         WriteSettingR.vi
|         write_digital_channel.vi
|         write_multiple_channels.vi
|
+---Kamera
|   |   changelog.txt
|   |   Kamera.vi
|   |
|   \---subVIs
|       |   Checksum.vi
|       |   HighPerformanceCounter1st.vi
|       |   HighPerformanceCounterInit.vi
|       |   HighPerformanceCounterWait.vi
|       |   hvang-global_.vi
|       |   InitSerialChipOX.vi
|       |   KameraInit.vi
|       |   motor_vars_global.vi
|       |   PulsoxiInterpolate.vi
|       |   ReadSettingR.vi
|       |   RecordStart.vi
|       |   RecordStartP.vi
|       |   SerialReadString.vi
|       |   SerialString.vi
|       |
|       +---board.vis
|           |   about.vi
|           |   BothSlopes.vi
|           |   Cal16Bit.vi
|           |   clearRead.vi
|           |   closeshutter.vi
|           |   Coolon.vi
|           |   ErrMsgOff.vi
|           |   ErrMsgOn.vi
|           |   ESLSCDLL.dll
|           |   ESLSCDLL_2cam.dll
|           |   Exit.vi
|           |   FFDis.vi
|           |   FFEn.vi
|           |   FFGETone.vi
|           |   FFOvl.vi
|           |   FFRead.vi
|           |   FFReadCnt.vi
|           |   FFRS.VI
```

B LabVIEW

		FFStopTimer.vi
		FFSWTrig.vi
		FFValid.vi
		FFXCKI.VI
		GETCCD.vi
		HiSlope.vi
		InitBrd.vi
		InitDrv.vi
		InitSysTimer.vi
		IsFFT.vi
		IsPDA.vi
		LowSlope.vi
		Mouse_off.vi
		Mouse_on.vi
		OpenShutter.vi
		OTrig_h.vi
		OTrig_l.vi
		OutTrigP.vi
		ReadB.vi
		ReadFFLoop.vi
		ReadL.vi
		ReadLoop.vi
		ReadRingBlock.vi
		RS_TOREG.vi
		SetAd16Default.vi
		SetADcds.vi
		SetAdGain.vi
		SetAdOff.vi
		SetDA.vi
		SetExtTrig.vi
		SetIntTrig.vi
		SetOvsmp.vi
		SetTemp.vi
		SetTOREG.vi
		SetVCLKReg.vi
		SRingBlockTrig.vi
		SRingLastRead.vi
		SRingReadCnt.vi
		SRingStartFetch.vi
		SRingStartThread.vi
		SRingStopThread.vi
		SRingThreadIsOFF.vi
		SRingValid.vi
		StartTimer.vi

```
|      |      TGood.vi
|      |      vi_description.txt
|      |      V_off.vi
|      |      V_on.vi
|      |      WaitforTelapsed.vi
|      |      waitTrig.vi
|      |      WriteB.vi
|      |      WriteL.vi
|      |
|      | \---old_board.vis
|      |     __ExitInv.vi
|      |     __GetCCD.vi
|      |     __InitbrdInv.vi
|      |     __InitdrvInv.vi
|
| \---LadenProgrammLCTI
|   changelog.txt.txt
|   LadenProgrammLCTI.vi
|
| \---subVIs
|     Filter.vi
|     Josef.vi
|     LoadPart.vi
|     Mean.vi
|     SubDigAlgo.vi
|     SubDigAlgo_Save_Steps_As_Bmp.vi
|     SubDoPeri.vi
|     SubFindStartEndPx.vi
|     SubFlatten.vi
|     SubFlatten011209.vi
|     SubFlattenIntensity.vi
|     SubFrgClLoadB.vi
|     SubLoadPulseMaxima.vi
|     SubMaxReduce011209.vi
|     SubMaxReduce240608.vi
|     SubSaveFrg.vi
|     SubSaveFrgB.vi
|     SubSavePulseMaxima.vi
|     SubThreshold.vi
|     Sub_SaveAsBMP.vi
```

B.1 Axial Eye Length Measurement

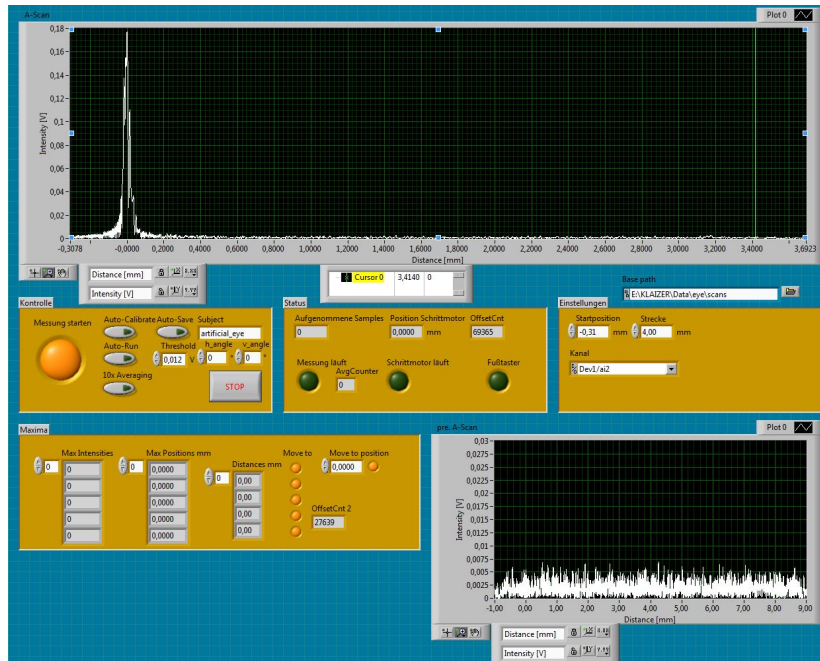
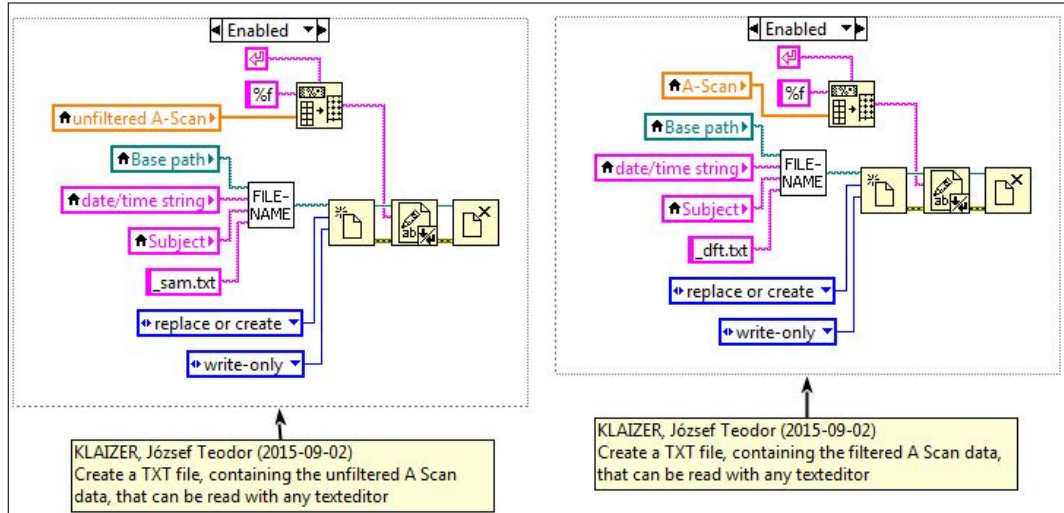
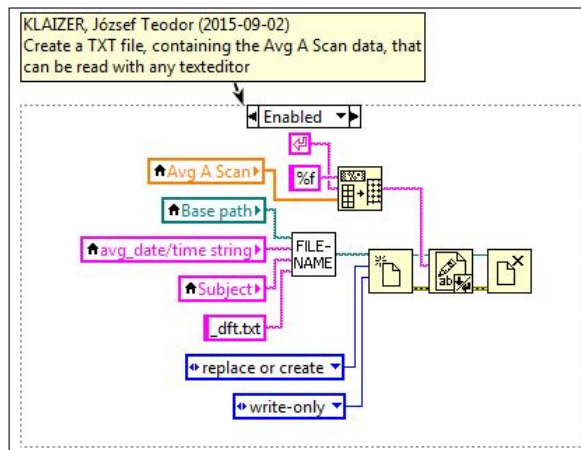


Figure B.1: LabVIEW front panel for axial eye length measurement (Augenlaenge.vi).

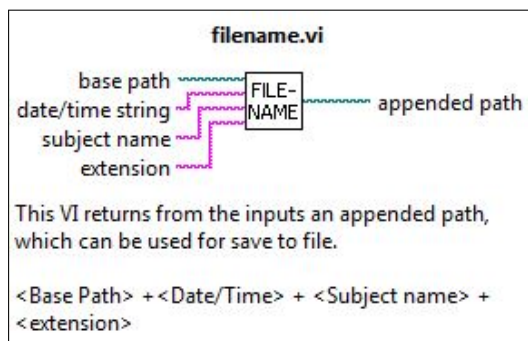


(a) Write unfiltered and digitally filtered A-scan data also to text file: *_sam.txt and *_dft.txt, respectively.

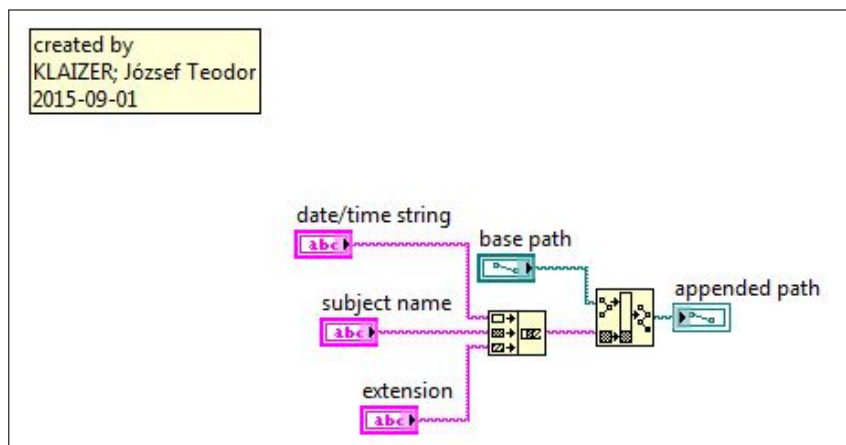


(b) Write digitally filtered A-scan data also to text file: *_dft.txt.

Figure B.2: Modifications on Augenlaenge.vi.



(a) Function signature.



(b) Block diagram of the VI.

Figure B.3: A new subVI (filename.vi) was created making easier and consequent (unified filenames) the saving of different output files.

B.2 Ocular Fundus Pulsation Measurement

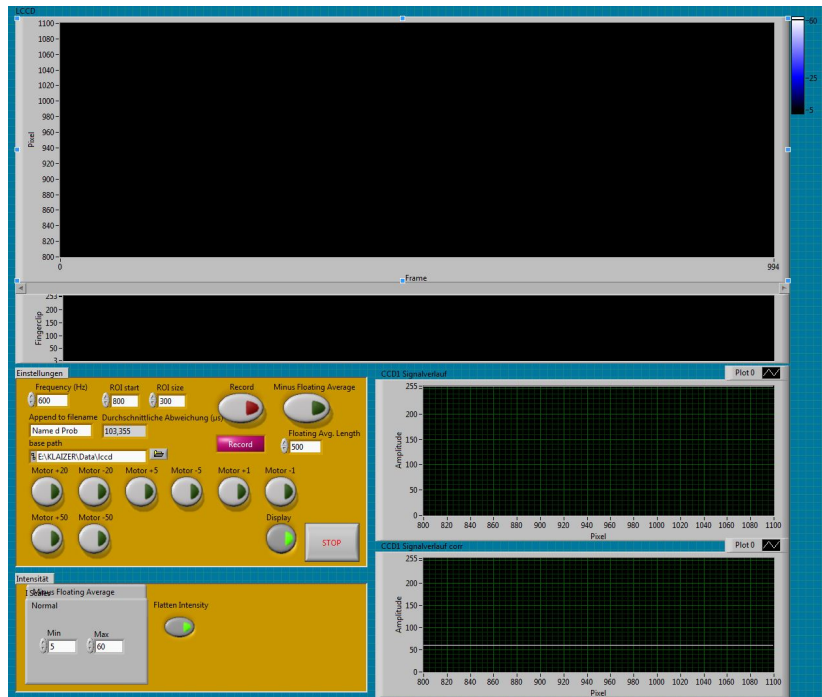


Figure B.4: LabVIEW front panel for ocular fundus pulsation measurement (Kamera.vi).

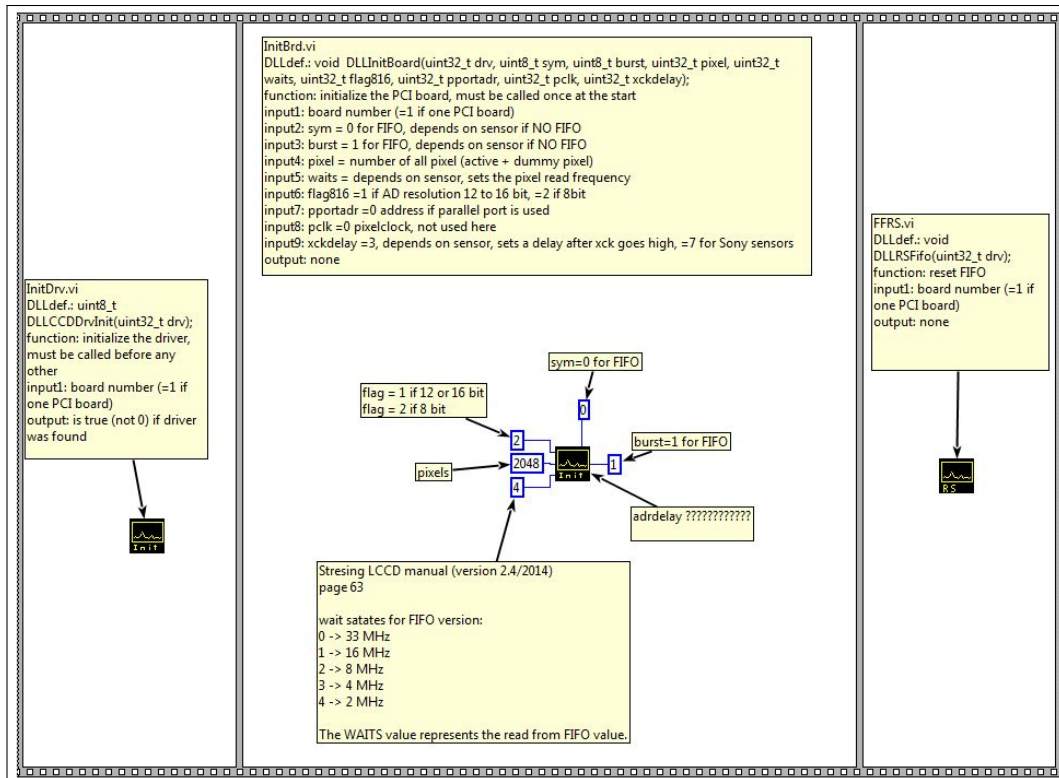
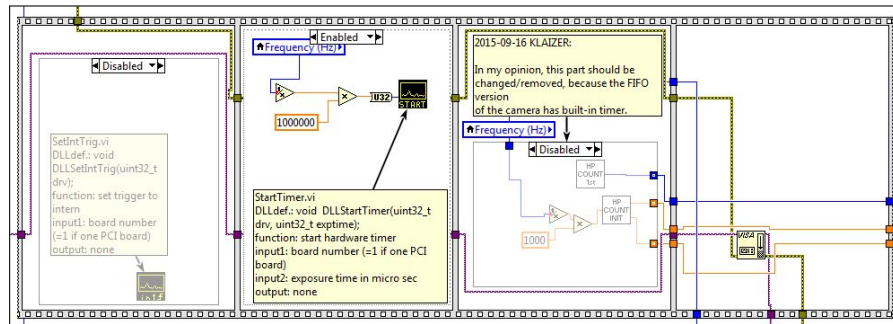
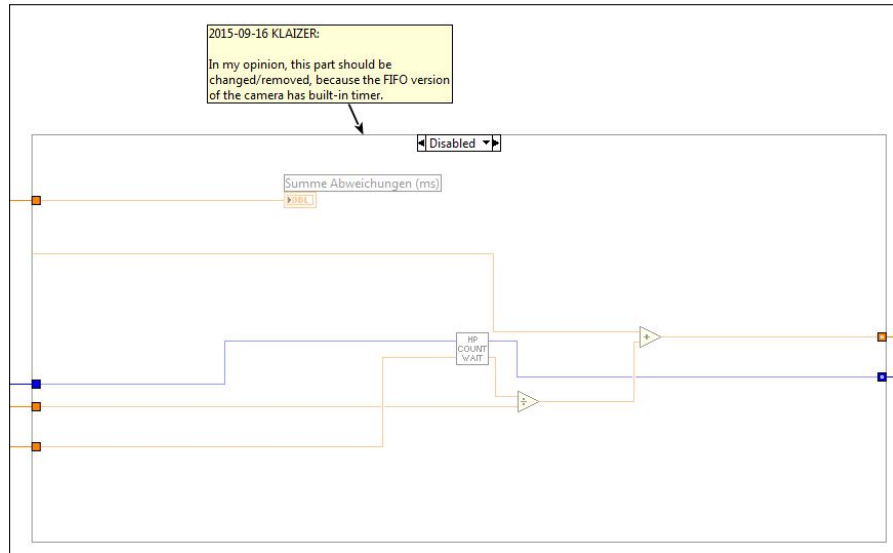


Figure B.5: LabVIEW block diagram of KameraInit.vi.



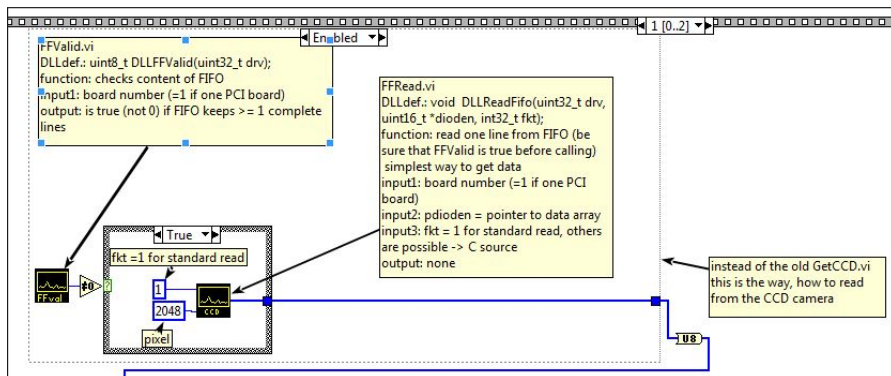
(a) The old method with software timer is for the noFIFO version, the FIFO hardware timer can be started by StartTimer.vi.



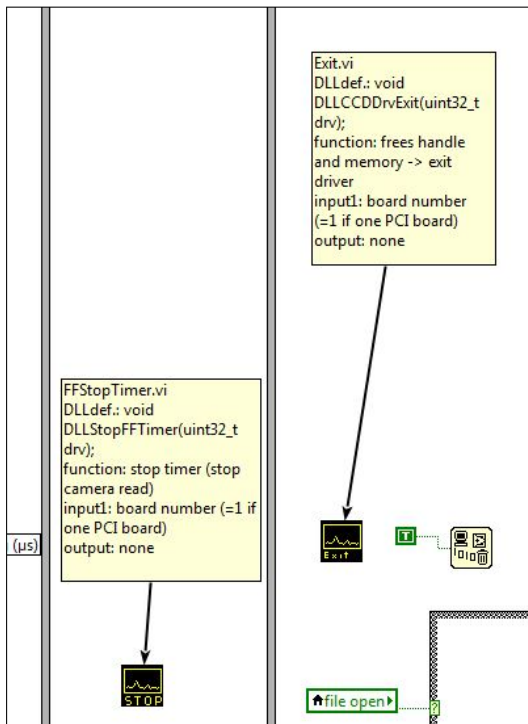
(b) For the noFIFO version a waiting function implemented by software was required. This is no more needed.

Figure B.6: The changed LabVIEW block diagram of Kamera.vi.

B LabVIEW



(c) Instead of the old method GETCCD.vi two new functions (FFValid.vi and FFRead.vi) has to be used for the readout.



(d) At the end, the hardware timer has to be stopped (FFStopTimer.vi) and memory has to be freed by Exit.vi.

Figure B.6: (cont.) The changed LabVIEW block diagram of Kamera.vi.

B.3 Data Evaluation

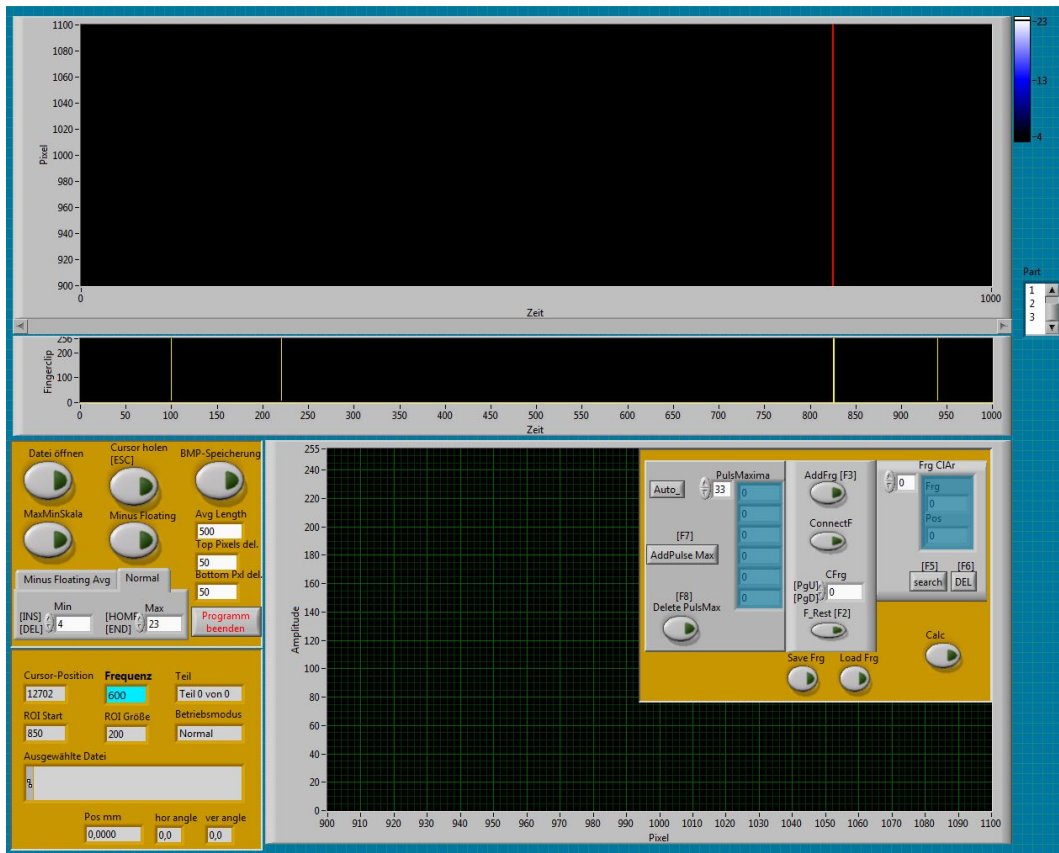


Figure B.7: LabVIEW front panel for ocular fundus pulsation evaluation (LadenProgrammLCTI.vi).

József Teodor KLAIZER

Curriculum Vitæ

Persönliche Daten

Adresse: Udvarnoki utca 8
H-9400 Sopron, Ungarn

E-Mail: jozsef.teodor@klaizer.at

Telefon: +43 660/634 05 77

Geburtsdatum: 27. Jänner 1989

Geburtsort: Sopron, Ungarn

Staatsangehörigkeit: Ungarn

Ausbildung

03/2012 – **TU Wien, Wien**
Masterstudium Biomedical Engineering
Masterthesis zum Thema „Depth-Resolved Measurement of Ocular Fundus Pulsations in Rats using Low-Coherence Tissue Interferometry“

09/2008 – 01/2012 **PPKE ITK, Budapest, Ungarn**
Bachelorstudium Molekulare Bionik
Bachelorarbeit zum Thema „Modification of a Low Coherence Tissue Interferometry (LCTI) system for use in the rodent eye“

09/2011 – 01/2012 **PPKE JÁK, Budapest, Ungarn**
Parallelstudium: Internationale Verwaltung BA

06/2008 **GYMJVÖ JÁGIKK, Győr, Ungarn**
Berufsprüfung mit Auszeichnung: Softwarebetreiber (EDV)

05/2008 **BDEG, Sopron, Ungarn**
Zweisprachige Matura mit Auszeichnung
Deutscher Nationalitätenzweig (Deutsch-Ungarisch)

Publikation

- (1) Nikolaus Dragostinoff, René M. Werkmeister, József Klaizer, Martin Gröschl und Leopold Schmetterer. „Time course and topographic distribution of ocular fundus pulsation measured by low-coherence tissue interferometry“. In: *Journal of Biomedical Optics* 18.12 (2013), S. 121502–121502.

Berufserfahrung

05/2014 – 03/2015	Bilfinger Baugesellschaft m.b.H., Wien Web and Database Engineer
05/2014 – 07/2014	TU Wien, Wien Projektassistent am Institut für Sensor- und Aktuatorssysteme • „Manipulation of Magnetically Labeled Jurkat Cells“
01/2012 – 06/2012	Telemark Marketing Gebhard Zuber GmbH, Wien Call Center Agent
10/2011 – 12/2011	ZMPBMT MedUni Wien – TU Wien Erasmus Praktikum im Zentrum für Medizinische Physik und Biomedizinische Technik

IT-Kenntnisse

IT-Softwarebetreiber	Berufsprüfung, 06/2008
ECDL-Zertifikat	02/2007
Linux, Windows	Arch Linux (desktop), Debian (home server), Linux Mint, MS Windows
Office & Textsatz	LaTeX2e, MS/Libre Office, Emacs, Scribus (python scripting)
Programmierung	Python 3, LabVIEW 2013, Sagemath, Matlab, R, C++, VBA

Ehrenamtliches Engagement

seit 2007	ehrenamtlicher Mitarbeiter – KIE (ungarischer CVJM/YMCA)
03/2013	„Hand in Hand – Take a Stand“, Hafnarfjörður, Island • 1 Woche Trainingskurs (European Fellowship) • Der Inhalt konzentrierte sich auf Jugendorganisationsentwicklung, soziale Rechte, die Bekämpfung von Rassismus und interkulturelle Verständigung
08/2008	YMCA Europe Festival 2008, Prag, Tschechische Republik

Interessen & Hobbies

Sport und Tanzen	<ul style="list-style-type: none">• Gesellschaftstanz (4 Jahre), Salsa (Grundlagen)• Kyokushin Karate (3 Jahre im Verein), Calisthenics
-------------------------	--

Psychologie

Einzelplatinen-Computer Banana PI, Raspberry PI

IT Security

Februar 2017